When plants paint their leaves purple: Spliceosomal complex components regulate acclimation responses during high light in Arabidopsis

Dissertation

to obtain the academic degree of

Doktor der Naturwissenschaften (Dr. rer. nat.)

submitted to the Faculty of Mathematics and Natural Sciences

at the University of Rostock

by

Gali Estopare Araguirang

Rostock, April 2025

https://doi.org/10.18453/rosdok_id00005424

Reviewers:

Prof. Dr. Andreas Richter, Universität Rostock, Institut für Biowissenschaften
Prof. Dr. Ekkehard Neuhaus, RPTU Kaiserslautern-Landau, Fachbereich Biologie

Date of Submission: April 11, 2025
Date of Defense: July 4, 2025

“I'm gonna live a life
Where I am proud to say
That I followed my joy
I followed my heart
I lived this one wild life,
I ripped it apart
I pushed through the corners
with no apologies
And finally I can say
I know the way
I'll say that I love
the way that I spent
My days”

-Joy Woods, “My Days”

(The Notebook The Musical)

This work was carried out from November 2020 to April 2021 at Humboldt Universität zu Berlin and from May 2021 to June 2024 at the University of Rostock under the supervision of Jun.-Prof. Andreas Richter, within the framework of the Collaborative Research Center/Transregio "TRR175: The green hub – Central Coordinator of Acclimation in Plants", supported by the German Research Foundation (INST 86/2042-1/ project C06).

Erklärung der Eigenständigkeit

Hiermit versichere ich, dass ich diese Arbeit selbstständig verfasst und keine anderen als die angegebenen Quellen und Hilfsmittel verwendet habe. Alle wörtlich oder sinngemäß aus anderen Werken übernommenen Inhalte wurden ordnungsgemäß gekennzeichnet. Zudem wurde diese Arbeit weder vollständig noch in Teilen in gleicher oder ähnlicher Form als Prüfungs- oder Studienleistung eingereicht.

Rostock, April 2025

_____

Gali Estopare Araguirang

Publications

8. **Araguirang GE**, Venn B, Kelber NM, Feil R, Lunn J, Kleine T, Leister D, Mühlhaus T, and Richter AS. (2023) "Spliceosomal complex components are critical for adjusting the C:N balance during high-light acclimation" The Plant Journal 119, 153-175. https://doi.org/10.1111/tpj.16751

7. **Araguirang GE**, Venn B, Kelber NM, Feil R, Lunn J, Kleine T, Leister D, Mühlhaus T, and Richter AS. (2023) "Spliceosomal complex components are critical for adjusting the C:N balance during high-light acclimation" BioRxiv https://doi.org/10.1101/2023.07.19.549727 [now in The Plant Journal, see Publication #8]

6. **Araguirang GE** and Richter AS. (2022) "Activation of anthocyanin biosynthesis in high light – what is the initial signal?" New Phytologist 236: 2037-2043. https://doi.org/10.1111/nph.18488

5. Zirngibl ME, **Araguirang GE**, Kitashova A, Jahnke K, Rolka T, Kühn C, Nägele T, and Richter AS. (2022) "Triosephosphate export from chloroplasts and cellular sugar content regulate anthocyanin biosynthesis during high light acclimation" Plant Communications https://doi.org/10.1016/j.xplc.2022.100423

4. Zirngibl ME, **Araguirang GE**, Kitashova A, Jahnke K, Rolka T, Kühn C, Nägele T, and Richter AS. (2022) "Triosephosphate export from chloroplasts regulates flavonoid biosynthesis and permits high light acclimation through the inactivation of SnRK1" BioRxiv https://doi.org/10.1101/2022.03.09.483619 [now in Plant Communications; see Publication #5]

3. Lin YC*, **Araguirang GE***, Ngo AH*, Lin KT, Angkawijaya AE, and Nakamura Y. (2020) "The Four Arabidopsis Choline/Ethanolamine Kinase Isozymes Play Distinct Roles in Metabolism and Development" Plant Physiology 183: 152-166. https://doi.org/10.1104/pp.19.01399 (*equal contribution)

2. **Araguirang GE**, Niemann N, Kiontke S, Eckel M, Dionisio-Sese ML, and Batschauer A. (2020) "The Arabidopsis cryptochrome 2 I404F mutant is hypersensitive and shows flavin reduction even in the absence of light" Planta 251:33. https://doi.org/10.1007/s00425-019-03323-y

1. **Araguirang GE**, Arizala AJR, Asilo EBB, Batalon JLS, Bello EB, Madigal JPT, Monge JR, Sanchez NAL, and Elegado FB. (2020) "Pre-Treatment and Enzymatic Hydrolysis of Banana (Musa acuminata x balbisiana) Pseudostem for Ethanol Production" Agro Bali: Agricultural Journal 3 (2): 98-107 https://doi.org/10.37637/ab.v3i2.608

The following awards and grants were received in association with this dissertation:

Awards

2023 **Reinhold-von-Sengbusch Best Poster Award** (out of ~100 posters), Molecular Biology of Plants Conference (Plant Physiology and Molecular Biology Section of the DBG), February 6-9, 2023, Hennef, Germany

2022 **European Molecular Biology Laboratory (EMBL) Best Poster Award** (out of ~150 Participants), 24th EMBL PhD Symposium (The Spectra of Life: Dimensional Breadth in Biological Research), December 07-09, 2022, EMBL, Heidelberg, Germany

2022 **Botanik Tagung Best Poster Award** (Rank 1 from the Top 10 Best Posters, out of 309 posters), Botanik Tagung 2022, Aug. 28 - Sept. 1, 2022, University of Bonn, Germany

2022 **New Phytologist Best Poster Award** (1st Prize, out of ~100 posters), New Phytologist's Next Generation Scientist 2022, July 19-22, 2022, University of Tartu, Estonia

Grants

2023 **Full Scholarship Travel Grant (10% Success Rate),** Early Career Researcher Plant Networking Meeting and IPB Symposium, Leopoldina/Leibniz Institute of Plant Biochemistry, Halle (Saale), Germany, 08-11 May 2023

2023 **Deutsche Botanische Gesellschaft e.V. (DBG) Travel Scholarship** (250 €), Molecular Biology of Plants 2023, Sportschule Hennef, North Rhine-Westphalia, Germany, 06-09 February 2023

2022 **Deutsche Botanische Gesellschaft e.V. (DBG) Travel Scholarship** (400 €), Botanik-Tagung: International Conference of the German Society for Plant Sciences, University of Bonn, 28 August – 01 September 2022

2022 **Full Scholarship Travel Grant (highly competitive),** New Phytologist Next Generation Scientist 2022, Delta Centre, University of Tartu, Estonia, 19-22 July 2022

Acknowledgements

This PhD thesis is the culmination of years of academic endeavor, intellectual pursuit, and personal growth. My journey as a scientist has been deeply shaped by extraordinary individuals whom I have had the privilege of learning from and working alongside since I started navigating this world of research in 2013. Their unwavering guidance, endless support, and invaluable wisdom have been instrumental in shaping my passion and dedication to scientific discovery. So this dissertation stands as a testament to the collective encouragement, mentorship, and kindness of many people, to whom I owe my deepest and heartfelt gratitude, that have accompanied me throughout this journey.

First and foremost, I am grateful to my PhD supervisor, Prof. Dr. Andreas S. Richter, for his mentorship. When I was academically lost in 2020, he saw potential in me, offering not just a research project but also a chance to rebuild my confidence and renew my sense of purpose in science. His belief in my abilities allowed me to navigate this project, and his patience in teaching me new techniques encouraged me to grow as a scientist. The scientific discussions, no matter how intense, pushed me beyond my limits, strengthening my ability to think more critically and independently. His support of my academic endeavors also opened doors I never thought possible, allowing me to gain international and prestigious accolades that once felt out of reach.

I would also like to express my appreciation to Prof. Bernhard Grimm (Humboldt-Universität zu Berlin) and Prof. Martin Hagemann (University of Rostock) for their constructive feedback and discussions during my progress report presentations. Their insights and expertise helped improve my research and challenged me to refine my scientific reasoning.

To my former colleagues in Berlin and Rostock, thank you for the many scientific discussions, the shared frustrations over failed experiments, and the moments of celebration when things finally worked. You all made the struggles of this PhD a little more bearable, and for that, I am truly grateful.

A special thank you to PD Dr. Stefan Timm and Klaudia Radloff-Michl, whose patience and expertise helped me process hundreds of samples for LC/MS and guided me through the complexities of using the LICOR machine. Their generosity with time and knowledge made a world of difference in my research.

I am also immensely grateful to many scientific collaborators who contributed to this project. I would like to thank PD Dr. Tatjana Kleine and Prof. Dr. Dario Leister (LMU Munich) for their support in whole genome sequencing to identify the SNPs in the *raa* mutants, and Dr. John Lunn and Regina Feil (MPIMP Golm) for their invaluable contributions to the quantification of phosphorylated sugars during HL. Their expertise and contributions were invaluable to this work.

To my former students, Lucas Erdmann and Nadja Kelber-Discher, thank you for the dedication in helping with the reconfirmation of the genotypes and characterization of my transgenic plants. Your time and hard work were instrumental in refining this research.

I would also like to extend my sincere gratitude to the Collaborative Research Center/Transregio "TRR175: The Green Hub – Central Coordinator of Acclimation in Plants", funded by the German Research Foundation (INST 86/2042-1, Project C06), for the generous financial support of my PhD. They made this research possible, and I am truly honored to have been part of this collaborative effort in advancing plant acclimation studies.

To my incredibly supportive former professors, Prof. Maribel L. Dionisio-Sese (University of the Philippines), Prof. Dr. Alfred Batschauer (Philipps Universität Marburg), and Dr. Yuki Nakamura (RIKEN CSRS, Japan), thank you for always being just one email away whenever I needed reference letters to apply for programs during my PhD. Your unwavering belief in me have provided invaluable opportunities that shaped this chapter of my career.

Beyond the laboratory, I also found a second home, my Asian communities in Berlin and Rostock. Being surrounded by these people who just get it and who understand the little things, the cultural nuances, and the emotions tied to leaving home and living overseas, makes this group feels like a family. To Pao, Marc, Ruth, Karla, Pat, Weng, Oliver, JM, Simeon, Pi, Miao, Che, Rhods, Amabelle, and Erwin, thank you for being my support system, for the laughter, for the meals that felt like home, and

for simply being there during my PhD. Your presence made this journey a little lighter and a lot more meaningful, and reminded me that no matter where I am, I am never alone.

To Pierre, my sunshine, words will never be enough to express how deeply grateful I am for you. Thank you for being by my side through countless sleepless nights of writing and rewriting, always reminding me to rest whenever I can, offering a quiet reassurance, and holding space for me when I needed it most. You have been my pillar of strength throughout my writing journey, constantly supporting me as I balanced the demands of finishing my dissertation while navigating my new work as a bridging postdoc. Your enduring patience, pure kindness, and gentle strength became my refuge in the most overwhelming moments. You believed in me, even in times when I struggled to believe in myself. Your presence was my greatest source of comfort and courage. Just knowing you were there was enough to carry me through. *Je t'aime tellement*!

And finally, to my family, my mom and my siblings, who have always believed in me, thank you for your unconditional love and faith. You have always been my foundation, my strength, and my greatest motivation. Thank you for allowing me to chase my elusive dreams, even when they took me thousands of miles away from home. This accomplishment is not mine alone. This belongs to you as well.

To everyone who has been part of this journey, from the bottom of my heart, *maraming salamat*! ♡

Summary

Acclimation is essential for plant survival and productivity, enabling them to respond effectively to environmental stressors such as high light intensity, extreme temperatures, drought, or nutrient fluctuations. To adapt to these changing environments, plants develop specialized mechanisms, including the accumulation of anthocyanins, which help mitigate damage and maintain metabolic balance.

Through a forward genetic screen aimed at identifying new factors involved in anthocyanin biosynthesis, Increased Level of Polyploidy1 (ILP1), a previously elusive protein that functions upstream of this pathway, was isolated. Despite its potential significance, only a handful of studies had characterized ILP1, leaving its role in acclimation and metabolism largely unknown.

To bridge this knowledge gap, a multidisciplinary approach incorporating extensive genetics, transcriptomics, metabolomics, cell biology, and physiological assays was employed. A time-resolved transcriptomic analysis during high light exposure revealed that starch and sugar metabolism are disrupted in the *ilp1-1* mutant. Biochemical quantification of starch, cytosolic sugars (sucrose, fructose, and glucose), and phosphorylated sugars (such as trehalose-6-phosphate and sucrose-6-phosphate) in *ilp1-1* showed significant accumulation during high light conditions.

Moreover, a time-resolved metabolic map of *ilp1-1* under high light exposure demonstrated that most amino acids exhibited reduced levels during acclimation. This suggests a striking imbalance in carbon-to-nitrogen pools, given the concurrent increase in sugar levels and decrease in amino acid content.

To further investigate ILP1's function, overexpression and genetic complementation lines of *ILP1* were generated. Interestingly, *ILP1* overexpression suppressed soluble sugar production under high light, indicating a regulatory role in sugar metabolism. Stable truncation mutants of ILP1 were also established and characterized to dissect the functional roles of its different domains. The results revealed that ILP1, particularly its GC-rich DNA-binding domain, represses sugar accumulation, highlighting a key molecular mechanism in metabolic regulation.

Given ILP1's additional implications in spliceosomal function and microRNA biogenesis, a systematic screen was conducted on other mutants within this complex and from different stages of the splicing cycle, including *NTC-RELATED PROTEIN1* (*NTR1*), *PLEIOTROPIC REGULATORY LOCUS1* (*PRL1*), and *PRE-mRNA PROCESSING8* (*PRP8*), and *SERRATE1* (*SE1*) from miRNA processing. Notably, *NTR1*, *PRL1*, and *PRP8* mutants, but not *SE1*, exhibited similar acclimation phenotypes to *ilp1-1*, characterized by anthocyanin overaccumulation, increased cytosolic sugars, and reduced amino acid levels under high light conditions. This indicates that these spliceosomal mutants are indispensable in the metabolic regulation of acclimation response.

Taken together, this dissertation further expands the current knowledge on ILP1's role beyond transcriptional repression, providing unprecedented insights on its broader function in metabolic homeostasis during acclimation response. Additionally, this study clearly provides an initial framework and a fundamental understanding of how spliceosomal components, or to a larger extent, the whole spliceosome, act as acclimation markers and regulate adaptive responses in plants during high light.

Zussamenfassung

Die Akklimatisierung ist entscheidend für das Überleben und die Produktivität von Pflanzen, da sie ihnen ermöglicht, effektiv auf Umweltstressoren wie hohe Lichtintensität, extreme Temperaturen, Trockenheit und Nährstoffschwankungen zu reagieren. Um sich anzupassen, entwickeln Pflanzen spezielle Mechanismen, darunter die Akkumulation von Anthocyanen, die helfen, Schäden zu minimieren und das metabolische Gleichgewicht aufrechtzuerhalten.

Durch einen forward-genetischen Screen zur Identifizierung neuer Faktoren in der Anthocyan-Biosynthese konnte Increased Level of Polyploidy1 (ILP1) isoliert werden – ein bisher wenig charakterisiertes Protein, das stromaufwärts dieses Signalwegs agiert. Trotz seines potenziellen Einflusses wurden nur wenige Studien zu ILP1 durchgeführt, wodurch seine Rolle in der Akklimatisierung und im Stoffwechsel weitgehend unbekannt blieb.

Um diese Wissenslücke zu schließen, wurde ein multidisziplinärer Ansatz angewandt, der umfassende genetische, transkriptomische, metabolische, zellbiologische und physiologische Analysen kombinierte. Eine zeitaufgelöste Transkriptomanalyse unter hoher Lichtintensität zeigte, dass der Stärke- und Zuckermetabolismus in der *ilp1-1*-Mutante gestört ist. Die biochemische Quantifizierung von Stärke, zytosolischen Zuckern (Saccharose, Fruktose und Glukose) sowie phosphorylierten Zuckern (wie Trehalose-6-phosphat und Saccharose-6-phosphat) in *ilp1-1* zeigte eine signifikante Akkumulation unter hoher Lichtintensität.

Darüber hinaus zeigte eine zeitaufgelöste metabolische Kartierung von *ilp1-1* unter hoher Lichtintensität, dass die meisten Aminosäuren während der Akklimatisierung in verringerten Mengen vorlagen. Dies deutet auf ein erhebliches Ungleichgewicht zwischen Kohlenstoff- und Stickstoffpools hin, da gleichzeitig die Zuckerkonzentration anstieg und der Aminosäuregehalt sank.

Um die Funktion von ILP1 weiter zu untersuchen, erzeugte ich Überexpressions- und komplementäre Zur weiteren Untersuchung der *ILP1*-Funktion wurden Überexpressions- und genetische Komplementationslinien von *ILP1* generiert. Interessanterweise unterdrückte die Überexpression von *ILP1* die Produktion

löslicher Zucker unter hoher Lichtintensität, was auf eine regulatorische Rolle im Zuckerstoffwechsel hinweist. Zusätzlich wurden stabile ILP1 Trunkierungsmutanten erzeugt und charakterisiert, um die funktionellen Rollen der einzelnen Domänen zu untersuchen. Die Ergebnisse zeigten, dass ILP1, insbesondere seine GC-reiche DNA-Bindedomäne, die Zuckerakkumulation unterdrückt und somit einen zentralen molekularen Mechanismus in der metabolischen Regulation darstellt.

Angesichts der zusätzlichen Rolle von ILP1 in der Funktion des Spleißosoms und der MikroRNA-Biogenese wurde eine systematische Untersuchung anderer Mutanten innerhalb dieses Komplexes sowie aus verschiedenen Phasen des Spleißzyklus durchgeführt. Dazu gehörten *NTC-RELATED PROTEIN1* (*NTR1*), *PLEIOTROPIC REGULATORY LOCUS1* (*PRL1*) und *PRE-mRNA PROCESSING8* (*PRP8*) sowie *SERRATE1* (*SE1*), das in der miRNA-Prozessierung eine Rolle spielt. Auffällig war, dass die Mutanten von *NTR1*, *PRL1* und *PRP8*, jedoch nicht *SE1*, ähnliche Akklimatisierungsphänotypen wie *ilp1-1* zeigten. Diese waren gekennzeichnet durch eine übermäßige Anthocyanin-Akkumulation, erhöhte zytosolische Zuckerwerte und verringerte Aminosäuregehalte unter Hochlichtbedingungen. Dies deutet darauf hin, dass diese Spleißosomen-Mutanten eine unverzichtbare Rolle in der metabolischen Regulation der Akklimatisierungsreaktion spielen.

Zusammenfassend erweitert diese Dissertation das aktuelle Wissen über die Rolle von ILP1 über die transkriptionelle Repression hinaus und liefert neuartige Einblicke in seine umfassendere Funktion bei der metabolischen Homöostase während der Akklimatisierungsreaktion. Darüber hinaus stellt diese Studie ein grundlegendes Konzept bereit und schafft eine fundamentale Grundlage für das Verständnis, wie Spleißosomen-Komponenten, oder in größerem Umfang das gesamte Spleißosom, als Akklimatisierungsmarker fungieren und adaptive Reaktionen in Pflanzen unter Hochlichtbedingungen regulieren.

This dissertation is dedicated to my beloved grandmother, ***Maria****, who passed away in 2012, and my mom,* ***Madeline****, both of whom have been my greatest heroes. This is a tribute to their sacrifices, their dreams, and the boundless love they poured into me.*

Table of Contents

1 Introduction

1.1 Plant acclimation

Plants are one of the most vulnerable organisms when faced with harsh environmental challenges like light and temperature stresses. To survive and thrive under these fluctuating conditions, they have developed a remarkable ability to acclimate. This plant acclimation response involves intricate physiological, morphological, and molecular adjustments that enable plants to maintain homeostasis and optimize their growth and reproduction even under stress (Garcia-Molina et al., 2020; Kleine et al., 2021).

1.1.1 Morphological changes

To cope with immediate and short-term environmental changes, plants undergo morphological changes as part of their acclimation strategy (Alpert and Simms, 2002; Freschet et al., 2018; Rozendaal et al., 2006). Leaf structure is highly adaptable such that when plants are in high light environments, they often develop smaller, thicker leaves to reduce water loss and prevent damage from excessive sunlight (Leigh et al., 2017). Conversely, shade-tolerant plants might have larger, thinner leaves to capture more light (Zhang et al., 2007; Wang et al., 2024b). These morphological adaptations are not only crucial for individual survival but also affect plant competition and community dynamics. Plants with more efficient acclimation strategies often outcompete others, influencing the composition and structure of plant communities (Craine and Dybzinski, 2013).

1.1.2 Physiological and biochemical changes

One of the primary ways plants acclimate is through physiological and biochemical adjustments. Photosynthesis, the process by which plants convert light energy into chemical energy, is highly sensitive to environmental changes. In low light conditions, plants may increase chlorophyll concentration to maximize light absorption (Chen et al., 2021), while in high light conditions, they can increase the efficiency of their photosynthetic machinery to avoid photoinhibition and dissipate excessive excitation energy (Goss and Lepetit, 2015; Mittler et al., 2022). Similarly, plants adjust their respiration rates to balance energy production and consumption, ensuring that cellular functions are maintained even under stress conditions (Zhang et al., 2020).

1.2 Anthocyanin Biosynthesis

One of the key responses to light acclimation is the biosynthesis of anthocyanins (Figure 1), a group of flavonoid pigments responsible for red, purple, and blue colors in plants. Anthocyanins are not merely for aesthetic purposes. They play several roles in plants, including attracting pollinators, deterring herbivores, and providing protection as antioxidants against various environmental stresses (Agati et al., 2020, 2021; Gould et al., 2018). Its biosynthesis involves a complex pathway regulated by genetic and environmental factors but serves multiple functional roles, particularly in plant stress responses.

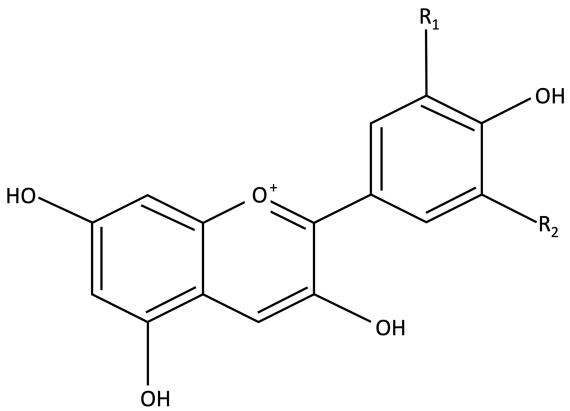

Figure 1. Basic chemical structure of anthocyanins.

1.2.1 Early Biosynthetic Genes (EBGs)

The first steps of the anthocyanin biosynthetic pathway start with the phenylpropanoid Early Biosynthetic Genes (EBGs). It is comprised of the phenylpropanoid pathway, leading to the production of flavonoid precursors, and the first parts of the flavonoid pathway (Figure 2). Chloroplast-derived phenylalanine is converted to cinnamic acid by phenylalanine ammonium lyase (PAL). Subsequently, cinnamic acid is synthesized to *p*-coumaric acid by cinnamate-4-hydroxylase (C4H) which is then converted to *p*-coumaroyl-CoA by 4-coumarate CoA ligase (4CL). The latter step is an important step of the phenylpropanoid pathway because it provides the flavan backbone needed for flavonoid biosynthesis.

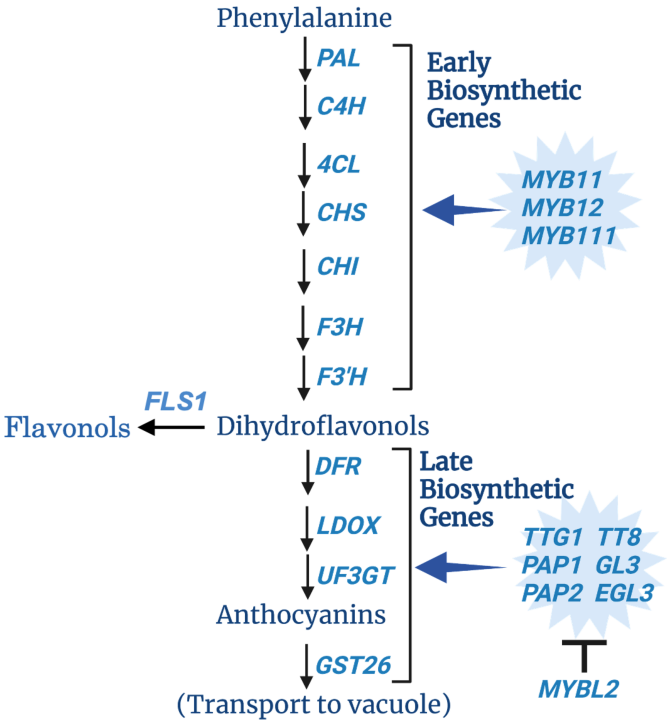

Figure 2. The anthocyanin biosynthetic pathway.

The *p*-coumaroyl-CoA is directed to the flavonoid biosynthetic pathway and is converted to naringenin chalcone by chalcone synthase (CHS), the first member of the EBGs. Then chalcone isomerase (CHI) synthesizes naringenin from naringenin chalcone. Subsequently, naringenin is converted to dihydroflavonols by flavanone

3-hydroxylase (F3H). Dihydroflavonols. are an essential pool of metabolites that serve as precursor for the biosynthesis of flavonols or leucoanthocyanidins that is catalyzed by flavonol synthase (FLS) or dihydroflavonol reductase (DFR), respectively. These EBGs are tightly regulated by transcription factors namely, MYB11, MYB12, and MYB111 (Stracke et al., 2007).

1.2.2 Late Biosynthetic Genes (LBGs)

The synthesis of leucoanthocyanidins by DFR, the first member of the LBGs, is the key and limiting step in the production of anthocyanins. This step is succeeded by converting leucoanthocyanidins into anthocyanidins by the action of leucocyanidin dioxygenase (LDOX). But because anthocyanidins are naturally unstable, they immediately undergo modifications such as glycosylation, methylation, and acylation by different transferases before they get transported to the vacuole for storage (Yonekura-Sakakibara et al., 2009).

Unlike the EBGs, the LBGs are controlled by a complex called MBW [Myeloblastosis (MYB), basic helix-loop-helix (bHLH), WD40]. The WD40 variant, TRANSPARENT TESTA GLABRA 1 (TTG1), together with bHLH TFs, TRANSPARENT TESTA 8 (TT8), GLABRA 3 (GL3), and ENHANCER OF GL3 (EGL3), act in concert with MYB TFs such as MYB75, also known as PRODUCTION OF ANTHOCYANIN PIGMENT 1 (PAP1), MYB90 (PAP2), MYB113, and MYB114 (Borevitz et al., 2000; Gonzalez et al., 2008; Lloyd et al., 2017). MBW complex activity is repressed by MYBL2 functioning as repressor of anthocyanin biosynthesis (Dubos et al., 2008; Matsui et al., 2008).

1.2.3 Other factors involved

Aside from the aforementioned genes and proteins, previous studies have shown the direct and indirect involvement of other factors in the production of anthocyanins (as reviewed by Araguirang and Richter, 2022). For example, reactive oxygen species and phytohormones were previously found to influence anthocyanin levels. Expression levels of the LBGs and components of the MBW complex were upregulated upon ROS application (Xu et al., 2017; Shi et al., 2018). Plant

hormones like cytokinin (Das et al., 2012; Wang et al., 2019), auxin (Liu et al., 2014; Wang et al., 2019), abscisic acid (Loreti et al., 2008; Shen et al., 2014; An et al., 2018; An et al., 2021b), and jasmonic acid (Loreti et al., 2008; Qi et al., 2011; Xie et al., 2016; Li et al., 2020; An et al., 2021a) also impact anthocyanin accumulation.

The SNF1-related kinase1 (SnRK1) that is highly evolutionary conserved in controlling more than a thousand genes for metabolism, growth and development (Baena-Gonzalez et al., 2007) also works upstream of the anthocyanin biosynthetic pathway (Broucke et al., 2023; Zirngibl et al., 2022). When sugar accumulates, particularly trioses exported out of the chloroplast by triose phosphate/phosphate translocator (TPT) under high light conditions, SnRK1 is inactivated to trigger HL-induced anthocyanin accumulation (Zirngibl et al., 2022). Under normal conditions, SnRK1 inhibits the production of anthocyanins both at the transcriptional and post-translational level, specifically by repressing the MBW activity through its dissociation, initiating PAP1 degradation, directly phosphorylating many MBW components, and directly/indirectly promoting the expression of *MYBL2* (Broucke et al., 2023).

1.3 Carbon : nitrogen balance

It is well-recognized that when the internal carbon pool increases because of a high photosynthetic activity, anthocyanin accumulates (Zirngibl et al., 2022). This is because the increase in carbon assimilation also provides more substrates to produce anthocyanins. Moreover, many sugar molecules such as trehalose-6-phosphate (T6P) can act as signaling molecules, to inactivate SnRK1 or activate transcription factors that upregulate anthocyanin biosynthetic genes.

In the same vein, the lack of nitrogen availability, a critical element for amino acid and protein synthesis, also affects anthocyanin levels (Lea et al., 2007; Liang and He, 2018; Liao et al., 2022). When nitrogen is abundant, resources are diverted towards primary metabolism, reducing the flux towards secondary metabolism, including anthocyanin biosynthesis (Nunes-Nesi et al., 2010). These previous studies support the notions that (1) carbon:nitrogen (C:N) balance should be tightly coordinated to maintain proper metabolism and (2) C:N interplay is mediated

through complex signaling pathways and gene regulatory mechanisms for optimal growth and development in response to environmental and nutritional cues.

1.4 The spliceosomal complex

The intricate process of anthocyanin biosynthesis is stringently regulated at the level of gene expression to allow plants to respond dynamically to internal and external stimuli. One important master regulator of gene expression is the spliceosome. The spliceosome is a highly conserved multi-megadalton complex and dynamic molecular machinery essential for gene expression in eukaryotic cells. It is responsible for the removal of non-coding sequences (introns) from precursor messenger RNA (pre-mRNA) and the precise joining of coding sequences (exons) to produce mature messenger RNA (mRNA) (Black, 2003; Wahl et al., 2009). This process, known as RNA splicing, is a crucial step in the post-transcriptional modification of RNA, ensuring that the resulting mRNA can be correctly translated into functional proteins (Lee and Rio, 2015).

The spliceosome undergoes at least seven sequential states throughout the splicing process, including the pre-catalytic, activated, step I catalytically activated, catalytic step I, step II catalytically activated, post-catalytic, and intron lariat spliceosome (ILS) stages (Wan et al., 2017). During the final phase of the canonical splicing cycle, the ILS is dismantled, allowing splicing factors to be recycled and intron lariats to be degraded (Arenas & Abelson, 1997). Disruptions in two key components of the ILS disassembly complex, *INCREASED LEVEL OF POLYPLOIDY 1* (*ILP1*) and *NTC-RELATED PROTEIN 1/SPLICEOSOMAL TIMEKEEPER LOCUS 1* (*NTR1/STIPL1*), have been linked to disturbances in important cellular processes like the circadian clock, cell cycle regulation, and heat stress tolerance, primarily due to alternative splicing (Cecchini et al., 2022; Dolata et al., 2015; He et al., 2023; Jones et al., 2012; Wang et al., 2019; Yoshizumi et al., 2006).

One of the most significant aspects of the spliceosome's function is its role in alternative splicing. Alternative splicing allows a single gene to produce multiple mRNA variants, leading to the generation of different protein isoforms (Brett et al.,

2002; Kan et al., 2001). This increases the diversity of the proteome and enables cells to adapt to various functional needs and environmental conditions (Syed et al., 2012). Hence, how mature mRNAs are accurately spliced is important for cellular process and also depends on different external cues such as light and temperature (Calixto et al., 2018; Fu et al., 2009; John et al., 2021; Martín et al., 2021). This is also why some mutants of the spliceosomal complex show pleiotropic phenotypes primarily because of differential splicing of many mRNA variants and secondly, a decrease in microRNA (miRNA) levels (Dolata et al., 2015; Wang et al., 2019).

1.5 microRNAs (miRNAs)

microRNAs (miRNAs) are small, non-coding RNAs that regulate gene expression post-transcriptionally. They bind to complementary sequences in target mRNAs, leading to translational repression or mRNA degradation (Lee & Ambros, 2001; Ruvkun, 2001). The biogenesis of miRNAs involves the transcription of primary miRNAs (pri-miRNAs), their processing into precursor miRNAs (pre-miRNAs), and finally the generation of mature miRNAs that are incorporated into the RNA-induced silencing complex (RISC).

miRNAs can fine-tune the expression levels of these genes, thereby modulating the production of anthocyanins in response to developmental cues and environmental stimuli (Chen et al., 2020; Li et al., 2019; Wang et al., 2020). In plants, the miR156 family is known to target SPL (SQUAMOSA Promoter Binding Protein-Like) transcription factors, which are key regulators of developmental timing and floral transition (Wang et al., 2020). SPL proteins have been shown to influence the expression of anthocyanin biosynthesis genes indirectly. By modulating SPL levels, miR156 can affect anthocyanin accumulation during different stages of plant development (Wang et al., 2020). Moreover, miR828 and miR858 target certain MYB transcription factors that act as repressors of anthocyanin biosynthesis (Tirumalai et al., 2019). The cleavage of these MYB mRNAs by miR828 can lead to the derepression of anthocyanin biosynthetic genes and therefore promoting pigment production.

1.6 *gun5* and suppressor screening

As it turned out that anthocyanin production is a result of chloroplast-to-nucleus-communication, mutants of this signaling process is also noteworthy to study. It was recently found that a mutant of the *Genomes Uncoupled5* (*GUN5*), an essential protein of the magnesium chelatase necessary for chlorophyll production, accumulated lower anthocyanin levels than WT during seedling development after norflurazon treatment (Richter et al., 2020). This observation suggested that *gun5* mutant either accumulates a repressor of the anthocyanin biosynthetic pathway or lacks an inducer of anthocyanin production after norflurazon application. To better understand this mechanism and discover novel factors that might be involved in anthocyanin biosynthesis, a forward genetic screening in *gun5* to induce single nucleotide polymorphisms (SNPs) using ethyl methanesulfonate (EMS) was employed. Second site mutations were identified in the *gun5* mutant which showed overaccumulation of anthocyanins (Araguirang et al., 2024). These mutants were later called as *restored anthocyanin accumulation* (*raa*) mutants.

After screening thousands of seedlings, six *raa* mutants, namely *raa7*, *raa8*, *raa10*, *raa13*, *raa14*, and *raa20* were isolated. After whole genome sequencing analysis, the exact SNPs from 3 out of the 6 *raa* mutants were identified, specifically the SNPs in *raa7*, *raa14*, and *raa20*. *Raa7* and *raa14* are allelic mutants of *Pleiotropic Regulatory Locus1* (*PRL1*) while *raa20* is a SNP mutant of *Increased Level of Polyploidy1* (*ILP1*). The mutants were backcrossed to Col-0 to get rid of the *gun5* background.

1.7 Background, aims, and scope of this work

High light acclimation response allows plants to adapt to unfavorable conditions in an appropriate and timely manner. This process involves complex regulatory networks that control gene expression and protein activity. From a forward genetic screen for new factors important in HL acclimation response, ILP1 was identified as an essential element upstream of the anthocyanin biosynthetic pathway.

Currently, there are only a handful of studies that have explored the diverse roles of ILP1, including its function as (1) a transcriptional repressor in vitro and in vivo

(Yoshizumi et al., 2006), (2) a protein factor needed for an efficient alternative splicing (Dolata et al., 2015), (3) a component of the spliceosomal complex involved in miRNA biogenesis (Wang et al., 2019), and (4) a destabilizer of the U6 nuclear small RNA (snRNA) level (Wu et al., 2024). However, how ILP1 functions during acclimation response remains largely unknown. To address this research gap, this dissertation aimed to integrate the known functions of ILP1 within the framework of HL acclimation. Specifically, a multifaceted approach was employed with the following objectives:

1. To unravel the molecular mechanism of how ILP1 regulates the transcriptional landscape of anthocyanin accumulation during HL;

2. To disentangle how ILP1 drives metabolic reprogramming under HL exposure;

3. To resolve the functionality of the different ILP1 domains in the context of acclimation response; and

4. To understand how ILP1, as part of the spliceosomal complex, maintains transcriptional and metabolic equilibrium during HL acclimation.

Experiments involving extensive genetics, transcriptomics, metabolomics, cell biology, and physiological assays were designed and conducted to explore ILP1 functions during acclimation response. Results from this research uncover a crucial link between carbon and nitrogen metabolism and further highlight the key roles of spliceosomal complex components in maintaining a timely transcriptional activation of necessary genes and proper metabolic homeostasis during HL exposure.

2 Materials & Methods

This chapter contains all buffers, reaction mixtures, mutant plants, techniques, and other materials used in the presented work. Additionally, it also outlines protocols for all the work presented in this dissertation.

Some parts of this section were published in:

Araguirang, G.E., Venn, B., Kelber, N.M., Feil, R., Lunn, J., Kleine, T., Leister, D., Mühlhaus, T., and Richter, A.S. (2024). Spliceosomal complex components are critical for adjusting the C:N balance during high-light acclimation. Plant J 119, 153-175 https://doi.org/10.1111/tpj.16751

2.1 Cloning and related techniques

2.1.1 Polymerase Chain Reaction (PCR)

Polymerase chain reactions were carried out either with Q5® High-Fidelity DNA Polymerase (New England Biolabs) in 25 µL reactions for cloning or DreamTaq Green DNA-Polymerase (Fisher Scientific) in 20 µL reactions for colony PCR and genotyping. Primer annealing temperatures were calculated with Thermofischer Tm Calculator and designed to have an annealing temperature of 60°C. The following reaction scheme was used:

Table 1. Q5 cloning reaction mixture.

Component	Volume (µL)
5X Q5 Reaction Buffer	5
10mM dNTPs	0.5
10 µM Forward Primer	1.25
10 µM Reverse Primer	1.25
Q5 Polymerase	0.25

H_2O	to 25
DNA	< 1000 ng

These two PCR reactions were run using the following programs:

Table 2. Q5 cloning PCR condition.

Temp in	Time	Loop
98°C	30 sec	
98°C	5-10 sec	
50-72°C	10-30 sec	
72°C	20-30 sec/kb	Back to step 2, Loop 34×
72°C	2 min	
4°C	∞	

2.1.2 Electrophoretic separation of DNA using agarose gels

Agarose gel electrophoresis was performed to separate DNA products. The gel contained 1% (w/v) agarose, 1X TAE buffer and ethidium bromide (EtBr). Based on the sample number, appropriate combs were chosen. DNA samples were loaded on the gel with a size marker (1 kb DNA ladder, NEB). The gel was subsequently run in 1X TAE buffer at 100V until satisfactory separation of the DNA was achieved. Gel visualization was achieved using a gel imaging system.

2.1.3 Restriction digests

Restriction digests were performed to (1) clone a particular construct into another plasmid vector, (2) open a target vector via its multiple cloning site (MCS), or (3) initially check for correct cloning prior to sequencing. The following reaction scheme was used and was incubated in an appropriate temperature:

Table 3. Restriction digest reaction mixture.

Component	Volume (µL)
10X Cutsmart Buffer	2
Restriction Enzyme	0.1
DNA	2
H2O	Vol. up to 20

2.1.4 Transformation of chemically competent cells

To transform cloned plasmid constructs into chemically competent cells (DH5α, GV3101), 5 µL of plasmid DNA was transferred into 75 µL of competent cells. The mixture was placed on ice for 20 minutes prior to heat shock at 42°C for 90 seconds or 5 minutes for DH5α or GV3101, respectively. The samples were placed on ice immediately for 2 minutes before incubation with 300 µL LB or YEB medium for 1 hr at 37°C.

2.1.5 Colony PCR

Grown colonies were picked for colony PCR using the following reaction mixture and program:

Table 4. Colony PCR reaction mixture.

Component	Volume (µL)
5X DreamTaq Reaaction Buffer	2
10mM dNTPs	0.8
10 µM Forward Primer	0.4
10 µM Reverse Primer	0.4
Q5 Polymerase	0.1
H2O	16.3
DNA	-

Table 5. Colony PCR DreamTaq program.

Temp in	Time	Loop
95°C	1-3 min	
95°C	30 sec	
50-72°C	30 sec	
72°C	1 min	Back to step 2, Loop 34×
72°C	5-15 min	
4°C	∞	

2.1.6 Isolation of plasmid DNA

First, to isolate plasmid DNA, 3 mL of liquid cultures with the appropriate antibiotics were incubated overnight. From these cultures, 2 mL was transferred to 2 mL Eppendorf tubes. The samples were centrifuged at a maximum speed for 30 seconds at room temperature (RT). The supernatant was discarded, and the pellet was dissolved with 300 µL of P1. Then 300 µL of P2 was added into the mixture and was incubated for 5 minutes at RT. Consequently, 300 µL of P3 was added into the solution and was kept on ice for 10 minutes. The samples were centrifuged at 4°C for 10 minutes at maximum speed. The supernatant was transferred into 1.5 mL eppi tubes and added with 700 µL isopropanol. The samples were centrifuged 4°C for 15 minutes at maximum speed. Then the supernatant was discarded and 800 µL of 70% ethanol (EtOH) was added to wash the pellet. The tubes were centrifuged at 4°C for 5 minutes at maximum speed then the supernatant was discarded. The pellets were air dried for 10 minutes at RT. Lastly, 25 µL ddH_2O was added to the tubes to dissolve the dried pellet. The aforementioned buffers were prepared using the following components:

Table 6. Buffer compositions used in plasmid isolation.

Buffers	Composition
P1 (Resuspension Buffer)	50 mM Tris-HCl pH 8.0, 10 mM EDTA, 100 µg/mL RNase A
P2 (Lysis Buffer)	200 mM NaOH, 1% SDS (w/v)
P3 (Neutralization Buffer)	3 M Potassium Acetate pH 5.5

2.2 Plant Materials

The following mutants were obtained from NASC seed stock centre: *ilp1-1* (SALK_030650C), *ilp1-2* (SALK_135563C), *ntr1-1* (SALK_073187), *prl1-2* (SALK_008466C), *pap1-D* (Borevitz et al., 2000) and *serrate1* (Ori et al., 2000; Prigge and Wagner, 2001). Homozygous plants were isolated by PCR-based genotyping with gene-specific primers and T-DNA-specific primers. For *se-1* mutants, DNAs were sent for sequencing to check for the 7bp deletion in the *SERRATE* genomic sequence (Figure S21C).

2.2.1 Plant growth conditions

Arabidopsis thaliana plants (Columbia-0 ecotype) were always grown under short-day conditions (10h light/14h dark regime) at 22°C, unless otherwise stated. For plant culture, Murashige and Skoog medium (Duchefa, M0222.0050) was used at 1/2 concentration (Murashige and Skoog, 1962). For both root and hypocotyl length experiments, seeds were sterilized with 70% ethanol and subsequently stratified at 4°C in the dark for 2–4 d before plating. For root length experiments, all plates were kept vertically until the desired day. On the other hand, for hypocotyl experiments, plates were also kept vertically after 6 hours of light induction but were kept in a dark place for 4 days. Roots and hypocotyls were photographed and measured manually with ImageJ. For plant media with and without nitrogen, the following modified concentrations were used:

Table 7. Modified MS media without nitrogen.

Concentration (mg/L)	Reagent
6.2	Boric Acid
332.2	Calcium Chloride, Anhydrous
0.025	Cobalt Chloride•6H_2O
0.025	Cupric Sulfate•5H2O
37.26	Na_2EDTA•2H2O
27.8	Ferrous Sulfate•7H2O
180.7	Magnesium Sulfate, Anhydrous
16.9	Manganese Sulfate•H2O

0.25	Molybdic Acid (Sodium Salt)•2H2O
0.83	Potassium Iodide
170	Potassium Phosphate, Monobasic
8.6	Zinc Sulfate•7H2O

Table 8. Modified MS media with nitrogen.

Concentration (mg/L)	**Reagent**
6.2	Boric Acid
332.2	Calcium Chloride, Anhydrous
0.025	Cobalt Chloride•6H_2O
0.025	Cupric Sulfate•5H2O
37.26	Na_2EDTA•2H2O
27.8	Ferrous Sulfate•7H2O
180.7	Magnesium Sulfate, Anhydrous
16.9	Manganese Sulfate•H2O
0.25	Molybdic Acid (Sodium Salt)•2H2O
0.83	Potassium Iodide
170	Potassium Phosphate, Monobasic
8.6	Zinc Sulfate•7H2O
101.1	Potassium Nitrate
80.04	Ammonium Nitrate

2.2.2 High light treatment

Two hours after light initiation, plants were exposed to continuous light at an intensity of 500 µmol photons m^{-2} s^{-1} for 24 hours under a constant temperature of 22°C in a Conviron GEN1000 (Canada) growth chamber equipped with a white LED light source. To inhibit photosynthesis, a 200 µM solution of DCMU (3-(3,4-dichlorophenyl)-1,1-dimethylurea) in water was applied to the leaves using a paintbrush. For the cold treatment, 4-week-old plants were maintained at 4°C for one week, with treatment beginning five hours after light onset. Sampling was conducted at midday on the seventh day of cold exposure.

2.2.3 Harvesting of samples

Experiments were conducted with up to four replicates, each containing material from three individual 4- to 5-week-old plants grown in separate pots. Samples were promptly frozen in liquid nitrogen and subsequently lyophilized for further processing. Unless specified otherwise, dried, finely ground leaf material was used for downstream analyses.

2.2.4 Plasmid construction and transgenic plant production

For *ProILP1:ILP1 ilp1*, a 6641 bp fragment of the *ILP1* genomic region was amplified by PCR using primers GA16 and GA17. This fragment included 1499 bp upstream of the start codon (containing the endogenous promoter) and 840 bp downstream of the stop codon. The amplified sequence was cloned into the pCambia3301 vector at *Sma*I restriction sites.

For *Pro35S:ILP1-HA*, a 2724 bp coding sequence (CDS) of *ILP1* was amplified using primers GA18 and GA90, then cloned into the *Sma*I site of the pCambiaStrep plasmid vector. The resulting vectors were introduced into *ilp1-1* and Col-0 plants via *Agrobacterium tumefaciens*-mediated transformation (floral dipping). T1 transformants were selected by Basta resistance, and resistant plants were genotyped for the *ilp1-1* background (LP = GA13, RP = GA14, LB = GA01) and endogenous *ILP1* (GA38 and GA344). The presence of the transgene was verified using primers GA44 and GA26. Selection and genotyping were repeated for the T2 generation. Expression levels of *ILP1* in knockout mutant alleles, genomic complementation, and overexpression lines were assessed using primers GA47 and GA48. Overexpression lines were designated as *OE #1* and *OE #12* while genetic complementation lines were designated as *ILP #2*, *ILP1 #3*, *ILP #5*, and *ILP #6*. The following floral dip solution was used:

Table 9. Composition of the flora dip solution.

Concentration	Reagent
0.5X	Murashige & Skoog Medium
5%	Sucrose
0.05%	Silwet L-77

All oligonucleotides used in this study can be found in Table S1.

2.2.5 Virus-Induced Gene Silencing

Double mutant of *ntr1-1* and a suppressed *ILP1* was generated by Virus-Induced Gene Silencing (VIGS) (Burch-Smith et al., 2006; Liu et al., 2002). To silence the expression of *ILP1,* the whole GC-rich DNA binding domain of *ILP1* was amplified using primers GA166 and GA90. The amplicon was digested with *Nru*I and cloned into the TRV2-vector (Burch-Smith et al., 2006). Both TRV1 and TRV2 vectors were transformed into *Agrobacterium tumefaciens* (GV3310). Then liquid cultures of the transformed agrobacteria were grown overnight and centrifuged at 3000 rpm for 15 min. Pellets were dissolved in 2 ml infiltration buffer (10 mM MgCl2, 10 mM MES) and OD600 was adjusted to 1.5. After 4 h incubation (dark, RT), cells were mixed 1:1 with *TRV1* and *TRV2-ILP1* and used to infiltrate 14-day-old *ntr1-1* plants. Small syringes without a needle were used with the opening pressed against the underside of the first true leaves. *TRV2-GFP* was used as a control. Primers GAA39 and GA40 were used to verify the suppression of *ILP1*. The following VIGS infiltration medium was used:

Table 10. The VIGS infiltration medium.

Concentration	Reagent
10 mM	$MgCl_2$
10 mM	MES pH 5.5

2.2.6 Anthocyanin quantification

Anthocyanins were extracted from leaf material using 1 ml of anthocyanin extraction buffer, consisting of 18% 1-propanol and 1% hydrochloric acid in water. The mixture was thoroughly mixed and incubated in darkness at room temperature for 2 hours. Following incubation, the samples were centrifuged at maximum speed for 15 minutes at 4°C. The supernatants were then transferred to cuvettes, and absorbance was measured at 537, 650, and 720 nm. Anthocyanin absorption was calculated using the formula: (A537–A720) – 0.25×(A650–A720). Finally, the results were normalized based on the fresh weight (fw) or dry weight (dw) of the samples.

2.3 RNA Extraction and quantitative PCR

RNA was extracted from ground leaf material by adding 300 µl of cell lysis buffer containing 2% SDS, 68 mM sodium citrate, 132 mM citric acid, and 1 mM EDTA. Next, 100 µl of a DNA/protein precipitation solution (4 M NaCl, 16 mM sodium citrate, and 32 mM citric acid) was added. The samples were vortexed, kept on ice for 10 minutes, and then centrifuged at 4°C for 10 minutes at maximum speed. To precipitate the RNA, 300 µl of the supernatant was mixed with an equal volume (300 µl) of 2-propanol. The mixture was centrifuged at room temperature for 5 minutes at maximum speed, and the resulting RNA pellets were washed with 800 µl of 75% ethanol, centrifuged again, and air-dried. Finally, the RNA was dissolved in 25 µl of RNase-free water and stored at -80°C for future use.

2.3.1 cDNA Synthesis

To synthesize cDNA from RNA, the following reaction mixture was prepared:

Table 11. cDNA synthesis reaction mixture.

Volume	Reagent
0.5 µL	100 µM Oligo dT
2 µL	5X Reaction Buffer

0.75 µL	water
1 µL	dNTPs
0.25 µL	Ribolock Inhibitor
0.5 µL	Reverse Transcriptase

A master mix containing 0.5 µL DNase and 0.5 µL DNase Buffer was added to 1.5 µg of RNA in 4 µL and incubated at 37°C for 30 minutes. To inactivate DNase, 1 µL of 25 mM EDTA was added, and the mixture was incubated at 65°C for 10 minutes. Subsequently, 5 µL of the reaction mixture was added to each tube and reverse transcribed at 42°C for 1 hour. The reverse transcriptase was then degraded at 70°C. The resulting cDNA was diluted with 40 µL of ddH_2O (1:5) and stored at -20°C for later use.

For quantitative polymerase chain reaction (qPCR) analysis, reactions were conducted using a CFX96-C1000 96-well plate thermocycler (Bio-Rad) with ChamQ Universal SYBR qPCR Master Mix (Absource Diagnostics, Germany). Relative gene expression was calculated using the $2^{-\Delta\Delta C(t)}$ method, with *SAND* (AT2G28390) serving as the reference gene.

For RNA sequencing (RNA-seq), the isolated RNA was treated with 2 µL (2 units) of DNase I and 3 µL of 10X DNase buffer, followed by incubation at 37°C for 30 minutes. To precipitate RNA, 70 µL of ddH_2O, 50 µL of 7.5 M ammonium acetate, and 400 µL of 100% ethanol were added. The mixture was centrifuged at 4°C for 20 minutes, and the pellet was washed with 800 µL of 70% ethanol. The RNA was then resuspended in 20 µL of ddH_2O and either stored at -80°C for future use or shipped on dry ice.

2.3.2 RNA Sequencing

Messenger RNA was isolated from total RNA using poly-T oligo-attached magnetic beads for PolyA-enrichment. Following fragmentation, first-strand cDNA was synthesized using random hexamer primers, followed by the synthesis of the second strand. The library was evaluated using Qubit and real-time PCR for quantification,

while a bioanalyzer was used to assess size distribution. The quantified libraries were sequenced on Illumina platforms (NovaSeq, paired-end, 150 bp), based on the effective library concentration and required data output (4GB raw reads). Raw sequencing data in FASTQ format underwent quality control using in-house Perl scripts, ensuring clean data (clean reads) by filtering out sequences containing adapters, poly-N regions, and low-quality reads. Additionally, Q20, Q30, and GC content were calculated for the clean data. The paired-end clean reads were then mapped to the reference genome using Hisat2 v2.0.5. Reference genome and gene model annotation files of the TAIR10 release were used (ensemblplants_arabidopsis_thaliana_tair10_gca_000001735_1). FeatureCounts v1.5.0-p3 was used to quantify the number of reads mapped to each gene. The FPKM (Fragments Per Kilobase of transcript per Million mapped reads) value for each gene was determined based on its length and the number of mapped reads. RNA-seq analysis was performed using two biological replicates of Col-0 and *ilp1-1*, with a total of six plants per time point.

2.4 Starch and sugar analysis

2.4.1 Starch extraction and quantification

Starch was extracted from dried, finely ground leaf material using 80% (v/v) ethanol supplemented with 1 µL of 20 mg/mL Ribitol and incubated at 80°C for 30 minutes. The samples were then centrifuged at room temperature (RT) for 10 minutes at maximum speed, and the supernatant was collected for soluble sugar quantification. The remaining pellet was resuspended in 750 µL of 0.5 M NaOH and incubated at 95°C for 30 minutes. Following this, 750 µL of 1 M CH_3COOH was added.

Starch digestion was performed by mixing 100 µL of the starch suspension with 100 µL of amyloglucosidase solution (1 mg/mL in 200 mM CH_3COOH and 100 mM NaOH) and incubating for 2 hours at 55°C with shaking at 1000 rpm. Next, 100 µL of the starch digest was combined with 200 µL of glucose oxidase reagent (containing 1 mg glucose oxidase, 1.5 mg horseradish peroxidase [HRP], 5 mg dianisidine/HCl in 50 mL of 0.5 M Tris/HCl [pH 7.0], and 40% [v/v] glycerol).

To create the glucose standard curve, glucose standards of 0, 100, 250, 500, and 750 µM were mixed with 200 µL of glucose oxidase reagent. Both the standards and samples were incubated at 30°C for 30 minutes, and the reaction was stopped by adding 400 µL of 5 M HCl. After brief centrifugation, absorbance was measured at 540 and 720 nm using a 96-well plate reader (SpectraMax M2, Molecular Devices, USA). The starch content was expressed as glucose equivalents, and the glucose concentration was determined using the standard curve.

To visualize starch content in situ, chlorophyll pigments were first removed by incubating leaves in 80% (v/v) ethanol at 80°C for at least 20 minutes until they became transparent or chlorophyll-free. The rosette leaves were then treated with Lugol's iodine solution for 1 hour, followed by destaining with H_2O.

2.4.2 Cytosolic sugar quantification

To the dried supernatant from starch extraction, 65 µL of a pyridine/methoxylamine solution (containing 20 mg methoxylamine per 1 mL pyridine; Sigma) was added. The samples were incubated at 30°C with shaking for 90 minutes, followed by brief centrifugation. Next, 35 µL of N-Methyl-N-trimethylsilyl-trifluoroacetamide (MSTFA) was introduced, and the mixture was incubated at 65°C for 90 minutes before another brief centrifugation. Quantification of glucose, fructose, and sucrose was performed using Gas Chromatography/Mass Spectrometry (GC/MS) (Agilent Technologies, USA). Ribitol served as the internal standard, and the sugar peak areas were normalized to the dry weight of the samples. Data analysis was conducted using the Agilent GC ChemStation software package (USA).

2.4.3 Sugar-phosphate extraction and analysis

Trehalose-6-Phosphate and other phosphorylated intermediates were extracted using a chloroform-methanol solution and quantified through high-performance anion-exchange chromatography combined with tandem mass spectrometry, following the method described by Lunn et al. (2006) with modifications from Figueroa et al. (2016).

2.5 In vivo transcriptional activity and sub-cellular localization

Transient transformation of leaves from *Nicotiana benthamiana* with Agrobacterium suspension was performed. The Agrobacterium cultures with an OD600 ~0.1 were harvested and resuspended in infiltration buffer (10 mM magnesium chloride, 10 mM MES pH 5.7, 100 µM acetosyringone). After 2 h incubation, the suspension was injected into the lower side of the leaves. The leaves were analyzed at the 3rd and 4th days after infiltration using a Zeiss LSM800 with Airyscan (Zeiss, Jena, Germany). The detection settings were chosen according to the fluorophores. Excitation of GFP was at 488 nm, and for chlorophyll, was at 640 nm.

For the in vivo quantitative luciferase assays, 4 days post-infiltration, the leaves were infiltrated with 1 mM luciferin (diluted in infiltration media) and waited for 20 minutes before analysis. The signals were detected using Clarity Western ECL substrate (Bio-Rad, Germany) and an ECL Chemostar CCD camera (Intas, Germany) and were quantified using imageJ.

2.6 ROS staining

The presence of superoxide radicals was detected using nitro blue tetrazolium chloride (NBT, Sigma-Aldrich [USA], 93862). Single leaves or entire rosettes from 4-week-old plants were immersed in an NBT staining solution (25 mM HEPES/KOH, 1 mg/mL NBT, pH 7.5). The leaves underwent vacuum infiltration for 15–30 minutes, followed by incubation in darkness at room temperature (RT) for 2 hours. Chlorophyll was then removed by treating the leaves with 80% (v/v) ethanol at 80°C in a water bath for 20 minutes.

Hydrogen peroxide accumulation was visualized using 3,3′-diaminobenzidine (DAB, Merck-Millipore [USA], D8001). The DAB staining solution (20 mM Tris/acetate, 1 mg/mL DAB [Sigma-Aldrich], pH 5.0) was prepared one hour before staining. Leaves were vacuum infiltrated with this solution for 30 minutes, then incubated in darkness at RT for 24 hours. Chlorophyll was subsequently

removed by treating the leaves with 80% (v/v) ethanol at 80°C in a water bath for 20 minutes.

2.7 Metabolite quantification

Metabolite quantification was performed using liquid chromatography coupled with tandem mass spectrometry (LC-MS/MS) on the LCMS-8050 system (Shimadzu, Japan). Approximately 2–3 mg of dried and ground leaf material was mixed with 100 µL of LC-MS buffer (150 µL chloroform, 350 µL methanol, and 1 µL of 1 mg/mL morpholinoethanesulfonic acid (MES) as an internal standard), followed by the addition of 400 µL of ice-cold LC-MS grade H_2O. After thorough mixing, the samples were incubated at -20°C for 2 hours. They were then centrifuged at maximum speed for 10 minutes at room temperature (RT), and the aqueous phase was transferred to fresh tubes. The remaining pellet was re-extracted with 400 µL of ice-cold LC-MS grade H_2O, vortexed, and centrifuged for 5 minutes at maximum speed. The aqueous phase was combined with the initial supernatant and dried overnight in a Speed-Vac (Eppendorf Concentrator plus™).

Metabolites were quantified using multiple reaction monitoring (MRM) based on the parameters defined in the LC-MS/MS method and the LabSolutions software package (Shimadzu, Japan). Calibration was conducted using authentic amino acid standards (Merck, Germany), and peak areas were normalized to the internal standard (MES). Data analysis was carried out using the LabSolutions software package (Shimadzu, Japan).

2.8 PAM measurement

Four-week-old plants (four plants per pot) were dark-adapted for 20 minutes prior to PAM measurement (Imaging PAM, Walz, Effeltrich, Germany). Plants were exposed to a pulsed, blue measuring beam (1 Hz, intensity 4, gain 1, damping 1) to obtain the basal chlorophyll (Chl) fluorescence (F) in darkness and a saturating light flash (intensity 10) was applied to determine the maximum Chl (F) in the dark-

adapted state (Fm) used for calculation of Fv/Fm. The PSII quantum yield [Y(II)=(Fm′–F)/Fm′], NPQ [NPQ=(Fm–Fm′)/Fm′], non-regulated energy dissipation Y(NO), and photochemical quenching (qP) were measured at 286 µmol photons m^{-2} s^{-1} of a blue LED light source.

2.9 Light response curves

Fluorescence light response curves (0, 25, 50, 100, 250, 500, 750, 1000, 1500 µmol m^{-2} s^{-1}) to measure photosynthetic rates before (T0) and after HL (T24) were measured using a Li-Cor-6400 gas exchange system (LI-COR, Lincoln, NE, USA) using fully expanded leaved from 7-week-old plants. The following conditions were set: block temperature = 25°C; CO_2 concentration = 400 ppm; flow rate = 300 µmol s^{-1}; and relative humidity = 60 to 70%.

2.10 Western blot and total protein quantification

Total leaf proteins were extracted from finely ground leaf material using a protein extraction buffer (PEB). Following resuspension in PEB, samples were incubated at 70°C for 20 minutes, then centrifuged at maximum speed for 10 minutes at room temperature (RT). The resulting protein extracts were transferred to fresh tubes and separated using 8% or 12% polyacrylamide-SDS gels before being blotted onto a nitrocellulose membrane.

Membranes were blocked for 1 hour with a 4% milk solution in TBS-T (50 mM Tris/HCl, 150 mM NaCl, pH 7.5, 0.1% (v/v) Tween 20), followed by overnight incubation at 4°C with primary antibodies in a 1% milk solution in TBS. The next day, membranes were washed and incubated with a secondary antibody (goat anti-rabbit immunoglobulin G [IgG] conjugated with HRP, 1:10,000 in 1% milk solution, TBS) for 1.5 hours at RT. Protein signals were visualized using Clarity Western ECL substrate (Bio-Rad, Germany) and an ECL Chemostar CCD camera (Intas, Germany). Antibodies were sourced from Agrisera (Sweden) and Bio-Rad (Germany). The following protein extraction buffer was prepared:

Table 12. Protein extraction buffer composition.

Concentration	Reagent
56 mM	Na_2CO_3
56 mM	DTT
2% (w/v)	SDS
12% (w/v)	Sucrose
2 mM	EDTA

Table 13. SDS-PAGE and western blot buffer compositions.

Buffers and Reagents	Composition
10X TBS Buffer	500 mM Tris, 150 mM NaCl, pH 7.5
10X Stock SDS/WB Solution (1 L)	30 g Tris, 144 g Glycin
Ponceau Staining Solution (500 mL)	50 mL Acetic Acid, 10 g Ponceau S
Coomassie Blue Staining Solution (1 L)	450 mL Methanol, 450 mL H2O, 100 mL Acetic Acid, 1 g Coomassie Brilliant Blue R-250
Destaining Solution for Coomasie Blue (1 L)	450 mL Methanol, 450 mL H2O, 100 mL Acetic Acid

2.11 Chlorophyll extraction

For chlorophyll extraction and quantification analysis, 1 ml of 80% acetone with 10 µM KOH in water was added to 1-5 mg of dry weight of samples. Samples were vortexed and incubated for 1 hr at -20°C, then centrifuged for 15 min (maximum speed) at 4°C. The supernatants were transferred to a new tube and absorbance was analyzed at 646, 663 and 720nm. Chlorophyll *a* and *b* were calculated using the formula:

Chl *a* (µg ml^{-1}) = 12.25 (A_{663nm}-A_{720nm}) – 2.79 (A_{645nm}-A_{720nm})

Chl *b* (µg ml^{-1}) = 21.50 (A_{645nm}-A_{720nm}) – 5.10 (A_{663nm}-A_{720nm}).

3 Results

Some parts of this section were published in:

Araguirang, G.E., Venn, B., Kelber, N.M., Feil, R., Lunn, J., Kleine, T., Leister, D., Mühlhaus, T., and Richter, A.S. (2024). Spliceosomal complex components are critical for adjusting the C:N balance during high-light acclimation. Plant J 119, 153-175 https://doi.org/10.1111/tpj.16751

3.1 *INCREASED LEVEL OF POLYPLOIDY1* (*ILP1*) mutants

3.1.1 *ilp1* characterization

From a forward genetic screen in a *gun5* mutant, a single nucleotide polymorphism (SNP) in *raa20* was identified by whole genome sequencing in position 2767004 of chromosome 5, which is the first nucleotide of intron 4 (C>T), causing a retention of intron 4 in the *ILP1* mRNA (AT5G08550) (Figure S1A). Here the *ilp1* mutants, namely the knockout mutants, *ilp1-1* and *ilp1-2* (Figure S1D, S1E), and a new mutant allele, *ilp1 SNP*, with an intron 4 retention (Figure 3A, S1B-S1C) were further characterized. Results from the high light shift experiments showed that all *ilp1* mutants accumulated more anthocyanins compared to Col-0 and *gun5-1* mutant, indicating that this phenotype is independent of *gun5* (Figure 3B).

Previous studies on *ILP1* knockout mutants reported short root and hypocotyl, and late flowering phenotype (Yoshizumi et al., 2006; Wang et al., 2019). To reconfirm these observations, further phenotypic characterization of *ilp1 SNP* along with the *ilp1* knockout mutants was performed. The results revealed similarities in root and hypocotyl length, flowering time, rosette phenotype, and anthocyanin

accumulation, suggesting that intron retention caused *ILP1* to resemble a knockout mutant at the post-translational level (Figure 3B-3F). Hence, using one T-DNA knockout mutant allele of *ilp1* in further downstream experiments would be representative already of the three mutants.

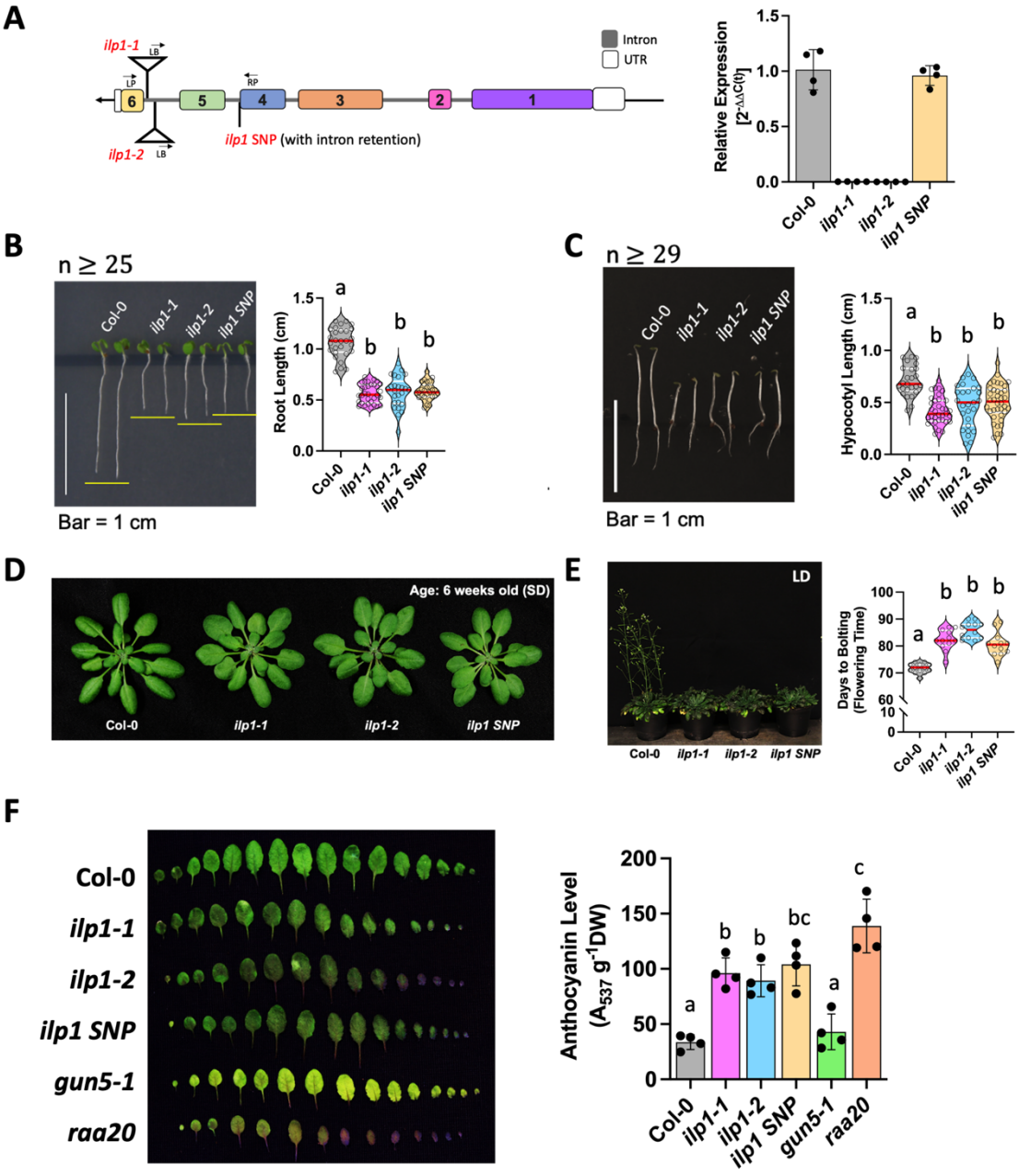

Figure 3. Phenotypic characterizations of the isolated *ilp1* mutants. (A) Locations of the T-DNA insertions and their corresponding *ILP1* relative expressions, (B) root lengths of 6DAG seedlings, (C) hypocotyl lengths of 4DAG dark-grown seedlings, (D) rosette, (E) flowering, and (F) anthocyanin content phenotypes of the *ilp1* mutants. For A and F, data are mean ± SD (n = 4). The red lines inside the violins show the median of values and the white lines the quartiles. Different letters indicate significance groups at $P < 0.05$ by Šidák's and Tukey's multiple comparison tests, respectively, as determined by two-way ANOVA.

3.1.2 Anthocyanin production in *ilp1-1*

To better understand the timing and factors influencing anthocyanin accumulation in *ilp1-1* mutant during HL shift, a kinetic analysis of anthocyanin production was conducted. The rate of anthocyanin biosynthesis in *ilp1-1* remained similar to Col-0 before HL (T0) and up to 12 hrs of continuous HL (Figure 4C). However, after 12 hrs, anthocyanins exponentially accumulated in *ilp1-1* mutant and continued to increase until 24 hrs of HL (Figure 4C). Anthocyanin production plateaued upon returning to normal light conditions for recovery. Kinetic analysis of mRNA transcripts involved in anthocyanin biosynthesis showed upregulation a few hours after the onset of HL. *PAP1* mRNA transcripts in *ilp1-1* exponentially increased and were significantly higher than WT after 4 hrs of HL while its target gene, *DFR*, was significantly upregulated at 12 hrs of HL (Figure 4A, 4B). This clearly displayed a proof of concept of a cascade of signaling process involving ILP1 in anthocyanin production during HL acclimation.

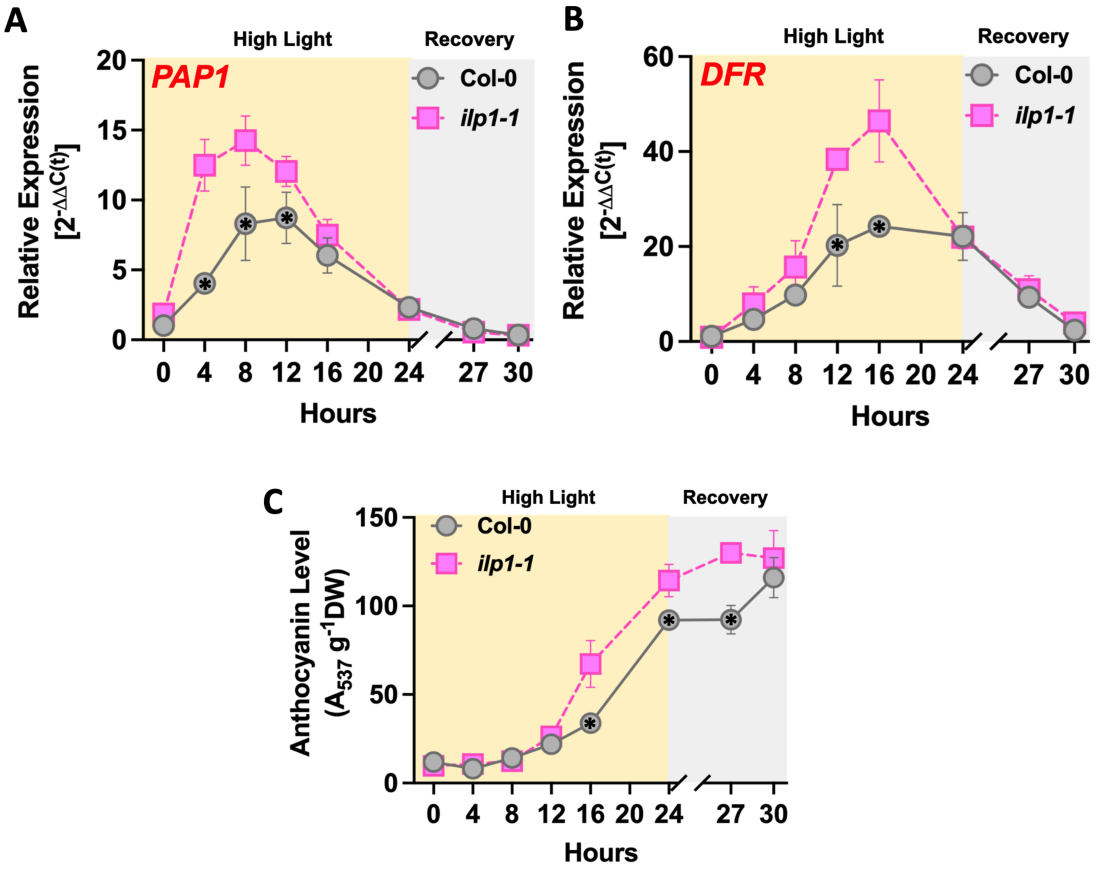

Figure 4. Kinetic analysis of mRNA transcripts and anthocyanin production in *ilp1-1*. Relative expressions of (A) *PAP1* and (B) *DFR*, and (C) anthocyanin accumulation during a 24-hr high light exposure and 6 hrs of recovery time. Asterisks indicate significance (P<0.05).

3.1.3 *ilp1-1* transcriptome

To examine global gene expression dynamics during HL exposure, a time-resolved RNA sequencing analysis was employed. Firstly, in the absence of *ILP1,* many genes were already upregulated and downregulated even before HL (T0) (Figure S2A). The highest peak of differentially upregulated genes occurred at 8 hrs of HL, while the highest number of differentially downregulated genes was observed during the recovery phase (T30) (Figure S2A). Targeted RNA-seq analysis of genes involved in anthocyanin biosynthesis revealed differential expression of multiple genes in *ilp1-1* across various time points. In particular, *4CL3*, *PAP2*, and *MYBL2* were already differentially expressed in *ilp1-1* even before HL, suggesting that their expressions are not dependent on HL, but on the absence or presence of a functional ILP1 (Figure 5A, 5B). Secondly, the average of log2 fold changes (FC) of different segments of the anthocyanin biosynthetic pathway showed that the most significant change happened at 4 hrs after HL (T4) within the flavonoid pathway (Figure 5D), indicating that this pathway plays a key role in driving the rapid anthocyanin production in *ilp1-1* during HL exposure (Figure 5C-5E).

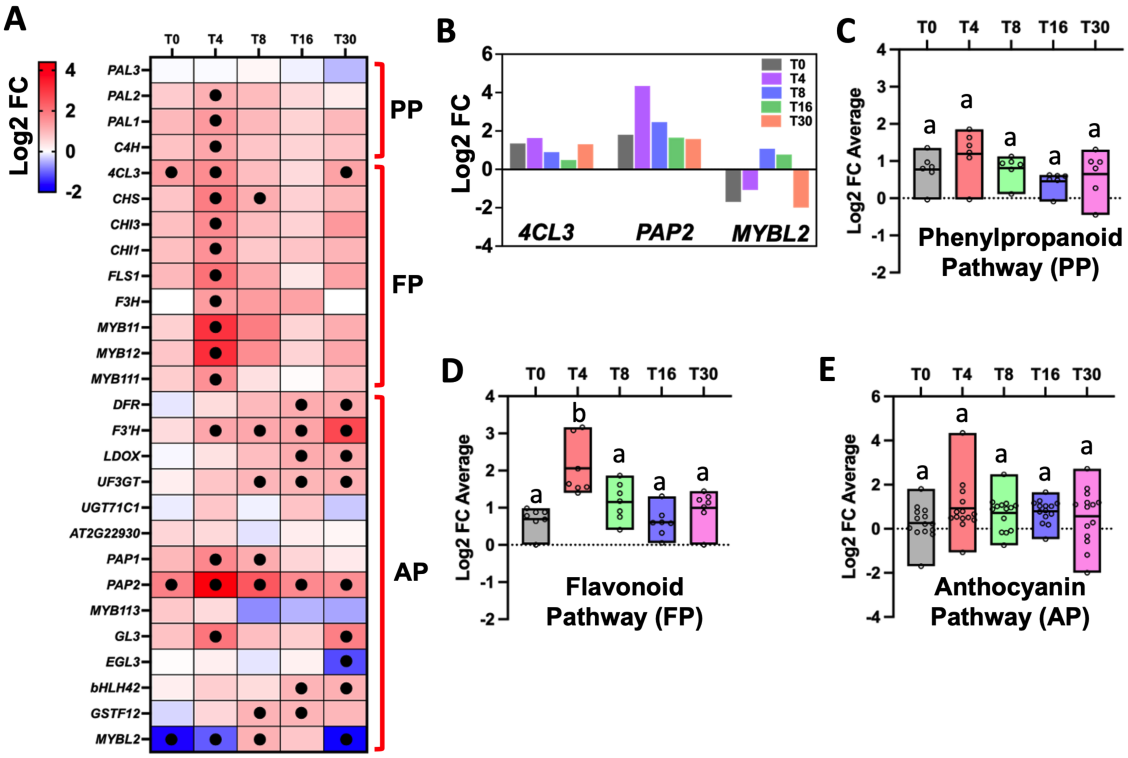

Figure 5. Targeted transcriptome analysis of genes directly involved in anthocyanin biosynthesis. (A) Log2 fold change (FC) of genes involved in the whole anthocyanin production across all time points measured, (B) Log2 FC of *4CL3*, *PAP2*, and *MYBL2* which are differentially expressed at T0, and Log2 FC average of genes that are

involved in the Phenylpropanoid biosynthesis (C), Flavonoid biosynthesis (D), and exclusively in the anthocyanin biosynthesis (E). Different letters indicate significance groups at $P < 0.05$ by Šidák's and Tukey's multiple comparison tests, respectively, as determined by two-way ANOVA. "•" in the heatmap indicates significance.

Further analysis of differentially upregulated KEGG pathways at T0 and T4 revealed significant enrichment of primary metabolism-related pathways. At T0, starch and sucrose metabolism showed one of the highest differentially expressed gene counts along with carbon metabolism and protein processing (Figure S2B). On the other hand, at T4, photosynthesis and other flavonoid-related pathways are more significantly enriched (Figure S2C), suggesting that ILP1 may directly or indirectly affect a multitude of primary and secondary pathways to regulate gene transcription.

3.1.4 Disrupted carbon metabolism in *ilp1* mutants

To identify which specific signal is responsible for the initiation of the anthocyanin biosynthetic pathway, ROS production and phytohormone biosynthesis were analyzed (Figure S3). Transcripts of ROS-induced chloroplastic *GLUTATHIONE PEROXIDASE7* (*GPX7*) increased significantly after 4 hrs of HL while cytosolic *ASCORBATE PEROXIDASE1* (*APX1*) exhibited a WT-like response until 12 hrs of HL in *ilp1-1* (Figure S3A, S3B). Superoxide and H_2O_2 staining of *ilp1-1* using NBT and DAB, respectively, under normal light and HL, revealed a WT-like phenotype, suggesting that ROS production is not the primary trigger of anthocyanin production in *ilp1-1* (Figure S3C, S3D).

Then, log2 FC average of genes involved in hormone biosynthesis during HL was calculated. Interestingly, no significant changes in expression profiles of genes involved in hormone biosynthesis were observed in *ilp1-1* during HL (Figure S3E). Even different hormone supplementation at increasing concentrations did not restore the *ilp1-1* root phenotype (Figure S3F). These findings imply that disrupted hormone production is not the causative factor for the elevated anthocyanin levels in *ilp1-1*.

A recent study showed that sugar molecules exported out of the chloroplast are the primary signals that initiate anthocyanin biosynthesis during HL (Zirngibl et al,

2022). The analyzed transcriptomic data indicated significant effects on carbon metabolism, particularly on starch and sugar metabolism, in *ilp1-1* (Figure S2B, S2C), prompting a detailed examination of these pathways. A transcriptomic landscape of sugar and starch metabolism during HL was mapped (Figure S4), revealing various constitutively and differentially expressed genes, including *GPT2*, one of the two glucose-6-phosphate/phosphate translocators in the chloroplast (Figure 6A). This observation is supported by the increase of both neutral (glucose, fructose, sucrose) and phosphorylated sugars (trehalose-6-phosphate, sucrose-6-phosphate) after 8 hrs of HL exposure (Figure 6D-6H).

Quantification and visualization of starch content using Lugol's staining in *ilp1-1* mutants showed higher starch levels at the end of the night (EoN), before HL (T0), and after HL exposure (T24) (Figure 6B-6C). Even under normal day/night cycles, *ilp1-1* accumulated more starch than Col-0 (Figure S5A). Starch synthesis and degradation rates were also analyzed, revealing no substantial differences between WT and *ilp1-1* (Figure S5B, S5C). These results suggest that increased starch levels in *ilp1-1* may be a result of either a gradual accumulation during its development or a sudden burst at a specific growth stage.

To check whether the increased starch and cytosolic sugar accumulation in *ilp1-1* is a direct consequence of an elevated photosynthetic rate, gas exchange parameters were analyzed, focusing on net CO_2 uptake rates before and after HL exposure. Measurements revealed that *ilp1-1* exhibited significantly higher photosynthetic rates than WT, both under normal light conditions (T0) and following HL exposure (Figure S6A, S6B). This enhanced CO_2 assimilation efficiency provides a mechanistic explanation for the greater starch reserves and elevated cytosolic sugar levels observed in *ilp1-1*, as increased carbon fixation would lead to an abundance of photosynthetic assimilates.

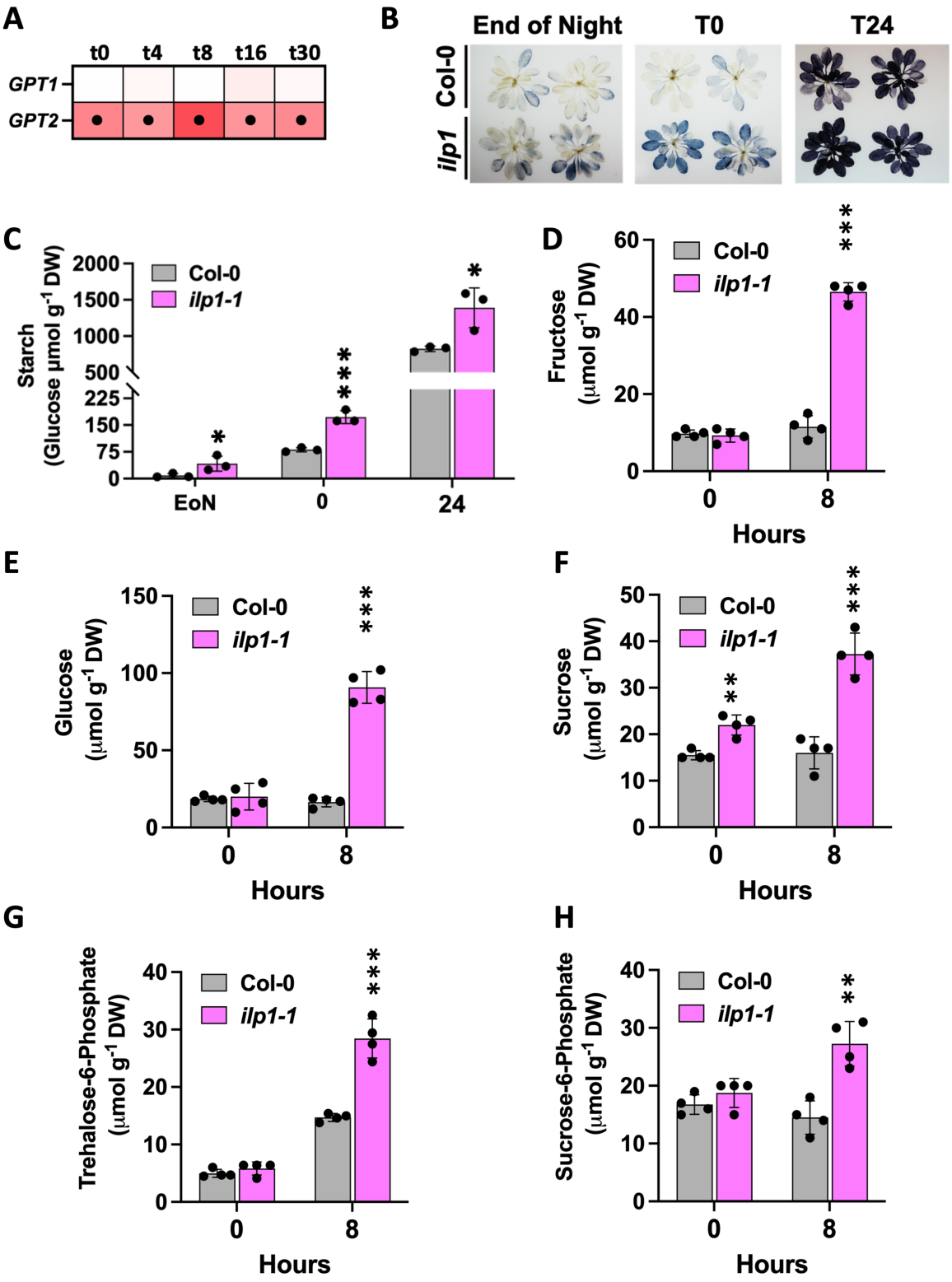

Figure 6. Imbalance in carbon metabolism in the *ilp1-1* mutant. (A) Differential expression of *GPT2* across timepoints, (B) Lugol's staining of and (C) starch content in *ilp1-1* mutant at the end of the night (EoN), before and after HL, (D) Fructose, (E) Glucose, (F) Sucrose,

(G) Trehalose-6-Phosphate, and (H) Sucrose-6-Phosphate levels before and after 8 hrs of HL. Data are mean ± SD (n = 4). Asterisks indicate statistical significance compared to Col-0 by Student's t-test (*P <0.05, **P <0.01, ***P <0.001). "•" in the heatmap indicates significance.

To assess potential changes in photosynthetic machinery, steady-state levels of selected photosynthetic proteins were also analyzed under HL conditions. The analysis revealed that LHCA1, a core component of Photosystem I (PSI) (Wientjes et al., 2011), was more abundant in *ilp1-1* than in WT after 8 hours of HL exposure (Figure S6C). This suggests a possible reprogramming and remodeling of PSI composition, potentially to compensate for HL-induced stress and optimize light capture and energy distribution.

Conversely, D1, a key subunit of PSII reaction centers (Russell et al., 1995), exhibited a decline in protein abundance during HL exposure compared to T0 across all genotypes. This reduction aligns with the natural turnover and degradation of D1, which is known to occur under HL conditions due to photodamage and repair cycles in PSII (Greenberg et al., 1987; Salter et al., 1992. Kato et al., 2012).

Similarly, LHCB6, a member of the light-harvesting complex of PSII (LHCII), exhibited a gradual decrease in protein levels across WT and *ilp1-1*, supporting a previous study that LHCII components are downregulated under HL stress in a protease-dependent hydrolysis (Luciński et al., 2011). In contrast, CP43 (another PSII core protein) and petA (a cytochrome f subunit of the cytochrome b6f complex) displayed unchanging protein levels at all time points, indicating stable expression of these components during HL exposure.

Transcriptomic analysis revealed contrasting regulatory patterns between nuclear-encoded and chloroplast-encoded photosynthetic genes in *ilp1-1* in response to HL exposure. Nuclear-encoded photosynthetic genes exhibited transcriptional repression during HL treatment (Figure S7A), while chloroplast-encoded genes, such as *psbA*, were upregulated in *ilp1-1* (Figure S7B). These findings align with the well-established concept that elevated carbohydrate levels suppress the expression of nuclear-encoded photosynthetic genes (Rolland et al., 2002; Figure S7A). In contrast, chloroplast-encoded genes like *psbA* are upregulated in response

to increasing light intensity as part of a photoprotective repair mechanism, ensuring the replacement of damaged PSII reaction centers (Chotewutmontri and Barkan, 2018; Schuster et al., 2020). This differential regulation of nuclear- and chloroplast-encoded genes highlights a possible function of ILP1 in coordinating proper long-term HL response. While nuclear gene repression likely prevents the overproduction of photosynthetic components to avoid excess energy accumulation, chloroplast gene upregulation prioritizes photoprotection and repair processes, ensuring photosynthetic stability under HL stress.

Ruban et al. (2016) previously demonstrated that photosynthetic efficiency is influenced by multiple factors, including chlorophyll content, expression of photosynthetic genes, non-photochemical quenching (NPQ), and other photoprotective mechanisms. To determine how these parameters correlate with photosynthetic rate, chlorophyll levels were first quantified under both normal and HL conditions. Analysis revealed no significant difference in chlorophyll content between WT and *ilp1-1*, both before HL exposure and after 8 and 24 hrs of HL treatment (Figure S7C). These findings indicate that chlorophyll content alone does not account for the higher photosynthetic rate observed in *ilp1-1* under HL conditions.

To assess in more detail the photosynthetic performance of *ilp1-1* under HL conditions, multiple photosynthetic parameters were measured, including variable to maximal fluorescence (Fv/Fm), photochemical quenching (qP), non-photochemical quenching (NPQ), effective quantum yield of PSII (Y(II)), and non-regulated energy dissipation (Y(NO)) (Figure S8).

Before and 8 hrs after HL exposure, Fv/Fm, a key indicator of photosynthetic efficiency, was higher in WT compared to *ilp1-1*. However, after 24 hrs of HL exposure, photosynthetic efficiency in WT declined, whereas *ilp1-1* exhibited an increase in Fv/Fm, suggesting a differential acclimation response between the two genotypes. Other photosynthetic parameters exhibited distinct regulatory patterns where NPQ/4, Y(NPQ) (regulated energy dissipation), qP, and Y(II) were higher in *ilp1-1* after 8 hrs of HL and remained relatively stable even after 24 hrs of HL exposure (Figure S8). The sustained high levels of NPQ and Y(NPQ) in *ilp1-1* suggest that the absence of ILP1 enhances the efficiency of both light-dependent

and light-independent photosynthetic processes under HL conditions. In particular, it indicates that in *ilp1-1*, there is (1) a strong photoprotective mechanism, allowing the plants to dissipate excess light energy efficiently, and thereby reducing photoinhibition and potential oxidative damage, and (2) more active carbon fixation processes, including Rubisco activity and metabolic flux through the Calvin-Benson cycle, potentially contributing to the observed increase in carbon assimilation and sugar accumulation under HL conditions.

3.1.5 DCMU treatment inhibits anthocyanin production

To further verify that sugars produced during photosynthesis drive anthocyanin biosynthesis during HL in *ilp1-1*, plants were treated with 3-(3,4-dichlorophenyl)-1,1-dimethylurea (DCMU), a specific and competitive inhibitor that blocks the plastoquinone binding site of photosystem II, thereby inhibiting photosynthetic activity. Inhibiting photosynthesis in *ilp1-1* suppressed anthocyanin accumulation during HL (Figure 7). Transcripts involved in anthocyanin biosynthesis like *PAP1*, *PAP2*, and *DFR* were suppressed in the DCMU-treated plants after 8 hrs of HL (Figure 7B-7E). Interestingly, *MYBL2* showed significant upregulation during HL when photosynthesis was blocked (Figure 7F), suggesting that the absence of sugar production during HL may have triggered the transcription of this repressor.

Analysis of *DARK INDUCIBLE1* (*DIN1*), *DIN10*, and *DIN6*, which are marker genes regulated by SnRK1 and dependent on trehalose-6-phosphate (Baena-González et al., 2007), revealed transcript upregulation in DCMU-treated plants during HL (Figure 7F, 7G, S9H). Venn diagram analysis of genes that are significantly downregulated in *ilp1-1* and significantly upregulated by KIN10, a catalytic subunit of SnRK1 (Baena-González et al., 2007), identified 52 common genes (Figure S9F), two of which were *DIN1* and *MYBL2*. This observation implies that *MYBL2* may also be regulated by SnRK1, further supporting recent findings indicating that *MYBL2* expression is directly or indirectly influenced by SnRK1 (Brocke et al., 2023).

Quantification of starch and neutral sugar levels after 24 hrs of HL revealed that both Col-0 and *ilp1-1* exhibited nearly negligible starch levels and suppression of cytosolic sugars like fructose, glucose, and sucrose (Figure S9A-S9D), validating previous notions that DCMU inhibits carbon metabolism. Conversely, levels of

essential amino acids such as phenylalanine and methionine were already elevated before DCMU treatment but declined afterward (Figure S9E), potentially limiting the availability of carbon skeletons required for amino acid synthesis. Interestingly, *GLUCOSE-6-PHOSPHATE/PHOSPHATE TRANSLOCATOR2* (*GPT2*), a transcript differentially expressed across all time points, maintained high transcript levels in *ilp1-1* compared to WT even after DCMU treatment (Figure S9G).

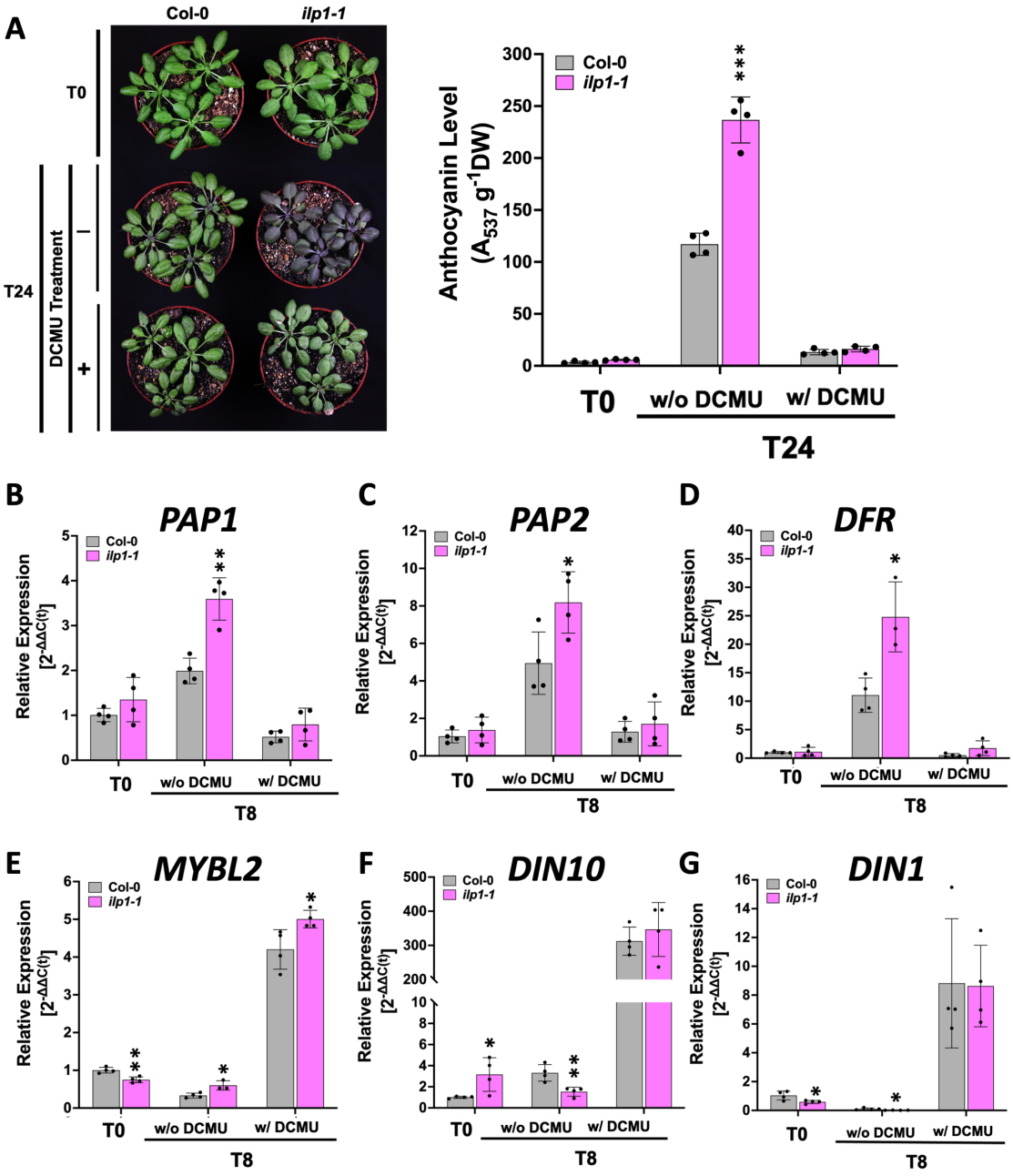

Figure 7. Phenotypic and transcriptomic changes in 4-week-old *ilp-1* after DCMU treatment during HL. (A) Anthocyanin levels before and after HL, and relative expressions of (B) *PAP1*, (C) *PAP2*, (D) *DFR*, (E) *MYBL2*, (F) *DIN10*, and (G) *DIN1* before and after 8 hrs of HL. Data are mean ± SD (n = 4). Asterisks indicate statistical significance compared to Col-0 by Student's t-test (**P* <0.05, ***P* <0.01, ****P* <0.001).

3.1.6 Convergence of metabolic and transcriptomic architectures

To understand how a non-functional ILP1 affected the metabolic response during HL, metabolite levels were quantified before and after HL exposure, and a metabolic map was constructed (Figure 8). The metabolic map generated provided a comprehensive overview of how *ILP1* loss-of-function influences key metabolic pathways during HL acclimation. Metabolite such as 3-Phosphoglyceric acid (3-PGA), a biochemically important intermediate for glucose production, showed higher levels before HL and during the first 8 hrs of HL exposure in *ilp1-1* (Figure 8), suggesting a possible disruption of glycolysis and Calvin-Benson cycle.

Most metabolites associated with amino acid biosynthesis, the tricarboxylic acid (TCA) cycle, and the urea cycle showed no significant differences in *ilp1-1* before HL exposure. However, following HL treatment, a pronounced decline in amino acid levels was observed in *ilp1-1* mutant compared to WT. Even metabolites like arginine, ornithine, and citrulline, which are key components of the urea cycle, also exhibited reduced levels during HL. Supplementing with exogenous ornithine or sodium nitroprusside, a nitric oxide donor, also did not complement the root and anthocyanin accumulation phenotype of *ilp1-1* (Figure S10B, S10C, S10E). This reduction of amino acid levels and metabolites of the urea cycle highlights a potential role of ILP1 in regulating amino acid homeostasis and nitrogen metabolism under stress conditions.

In contrast, succinate, which is a key intermediate in the TCA cycle and a crucial component of cellular metabolism and energy production, maintained consistently high levels during HL (Figure 8). This accumulation may have acted as a bottleneck in the conversion to fumarate and malate, leading to their reduced levels during HL and the subsequent recovery phase.

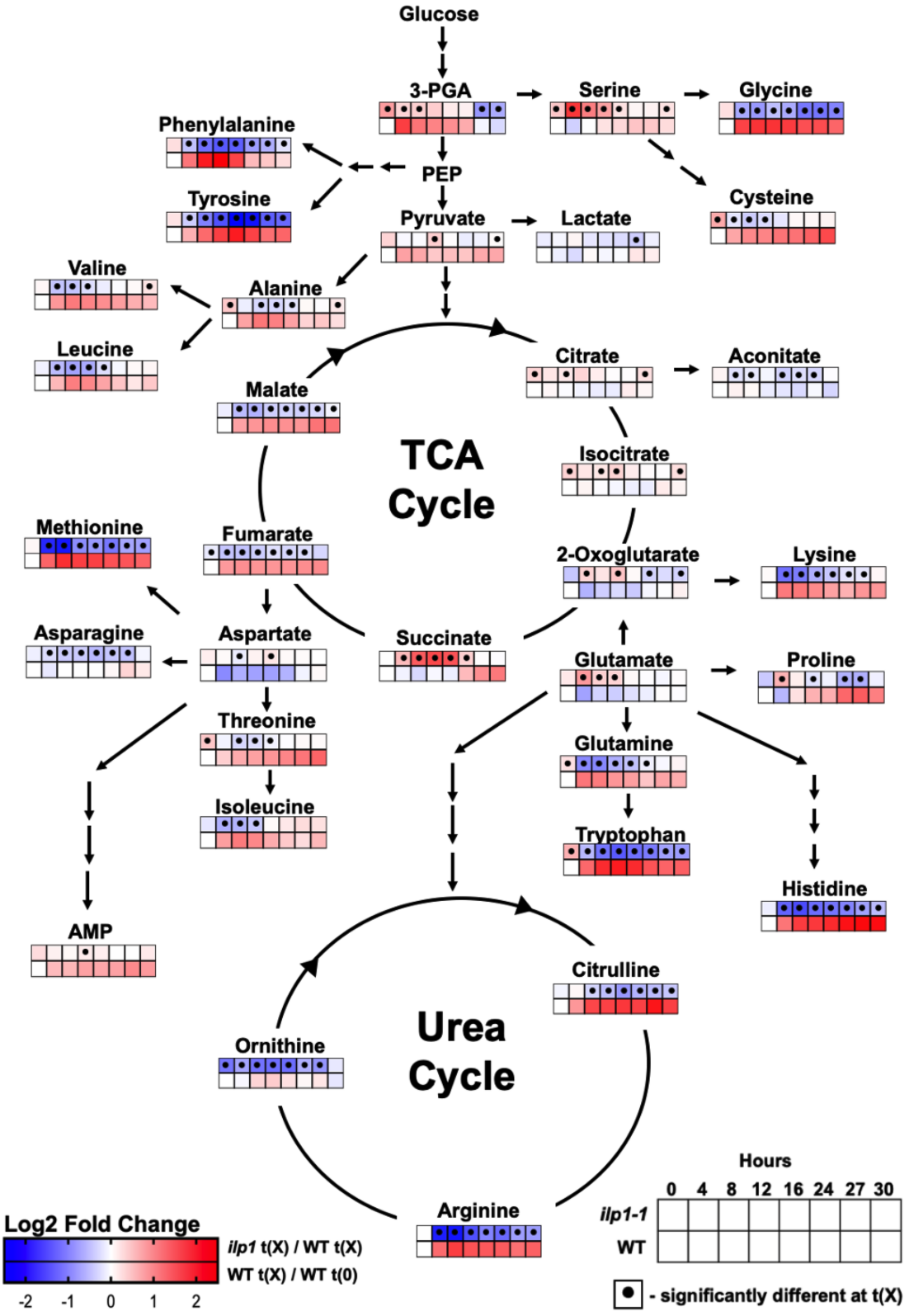

Figure 8. Metabolic map of quantified metabolites in WT and *ilp1-1* before, during, and after HL exposure. "•" in the heatmap indicates significance.

Analyzing the transcriptomic data of the genes involved in the TCA cycle showed differential expressions of four genes during HL, namely *MITOCHONDRIAL LIPOAMIDE DEHYDROGENASE1* (*mtLPD1*), *SUCCINATE DEHYDROGENASE2* (*SDH2*), *FUMARASE2* (*FUM2*), and *PHOSPHOENOLPYRUVATE CARBOXYKINASE2* (*PCK2*) (Figure S10A). Since *FUM2*, which encodes a crucial mitochondrial enzyme responsible for the reversible hydration of fumarate to malate, exhibited consistent downregulation across all time points, this suggests that *ilp1-1* had inherently low fumarate levels from the outset. To verify this, exogenous fumarate was supplemented to *ilp1-1*. However, no rescue of the anthocyanin phenotype was observed after 24 hrs of HL (Figure S10E).

Moreover, *SDH2,* which encodes a subunit of the succinate dehydrogenase (SDH) complex (Complex II) of the electron transport chain (ETC) and plays a dual role in the TCA and ETC during cellular respiration, displayed elevated levels during HL. To examine how the absence of *SDH2* affects acclimation response, a knockout mutant allele, *sdhaf2* (Huang et al., 2013), was exposed to HL for 24 hrs. Quantification of anthocyanin levels revealed WT-like phenotype of the *sdhaf2*, contrasting with the pronounced anthocyanin accumulation observed in *ilp1-1* (Figure S10D).

Another striking observation is the transient accumulation of glutamate within the first 12 hrs of HL exposure, after which it reverted to WT-like level. As a precursor for amino acid biosynthesis like glutamine and a key nitrogen donor in transamination and the urea cycle, the initial rise in glutamate corresponded with a decline in glutamine levels during HL exposure. This early glutamate surge after the onset of HL suggests that it initially acts as a nitrogen buffer or a nitrogen sink before being rapidly utilized in biosynthetic processes that fail to sustain amino acid pools under prolonged HL exposure.

3.2 Overexpression and complementation lines

Since knocking out *ILP1* resulted in overaccumulation of anthocyanins during HL, it was necessary to determine whether *ILP1* overexpression could suppress the accumulation of these metabolites. To investigate this, overexpression (*OE1* and

OE12) and genetic complementation constructs (*ILP1 #2*, *ILP1 #3*, *ILP1 #5*, and *ILP1 #6*) were generated in the *ilp1-1* background (Figure S11A, S11B).

Both OE and complementation lines exhibited a WT-like phenotype under normal conditions, including root, rosette, and flowering traits (Figure S11C-S11E). After 24 hrs of HL, neither the OE nor the complementation constructs suppressed anthocyanin accumulation (Figure 9A). Transcript analysis revealed that key genes in the early biosynthetic (EBG) and late biosynthetic (LBG) pathways, including *4CL3* and *DFR*, along with *FLS1*, displayed WT-like mRNA accumulation both before and during HL exposure in the OE and complementation lines (Figure 9B-9D). This pattern likely explains why anthocyanin levels in OE and complementation lines remained similar to Col-0 after 24 hrs of HL.

Similarly, when OE and genetic complementation lines were exposed to cold conditions (4°C) for 7 days, anthocyanin accumulation remained at WT-like levels (Figure S11F). Additionally, metabolic analysis revealed that OE and complementation lines already exhibited WT-like metabolite profiles (Figure S12). The accumulation of metabolites such as phenylalanine and glutamine was no longer repressed in OE and complementation lines, unlike in *ilp1-1* during HL, indicating that *ILP1* overexpression resulted in a metabolic response similar to Col-0 (Figure 9E, 9F).

Quantification of starch content also revealed that OE and complementation lines maintained WT-like levels before and during HL. However, analysis of cytosolic sugar contents showed lower levels of glucose, fructose, and sucrose levels during HL acclimation in the OE and complementation lines compared to WT and *ilp1-1* (Figure 9H-9J). This pattern suggests that ILP1 may regulate carbon metabolism by acting as a repressor, aligning with previous findings that ILP1 is a transcriptional repressor in vivo (Yoshizumi et al., 2006).

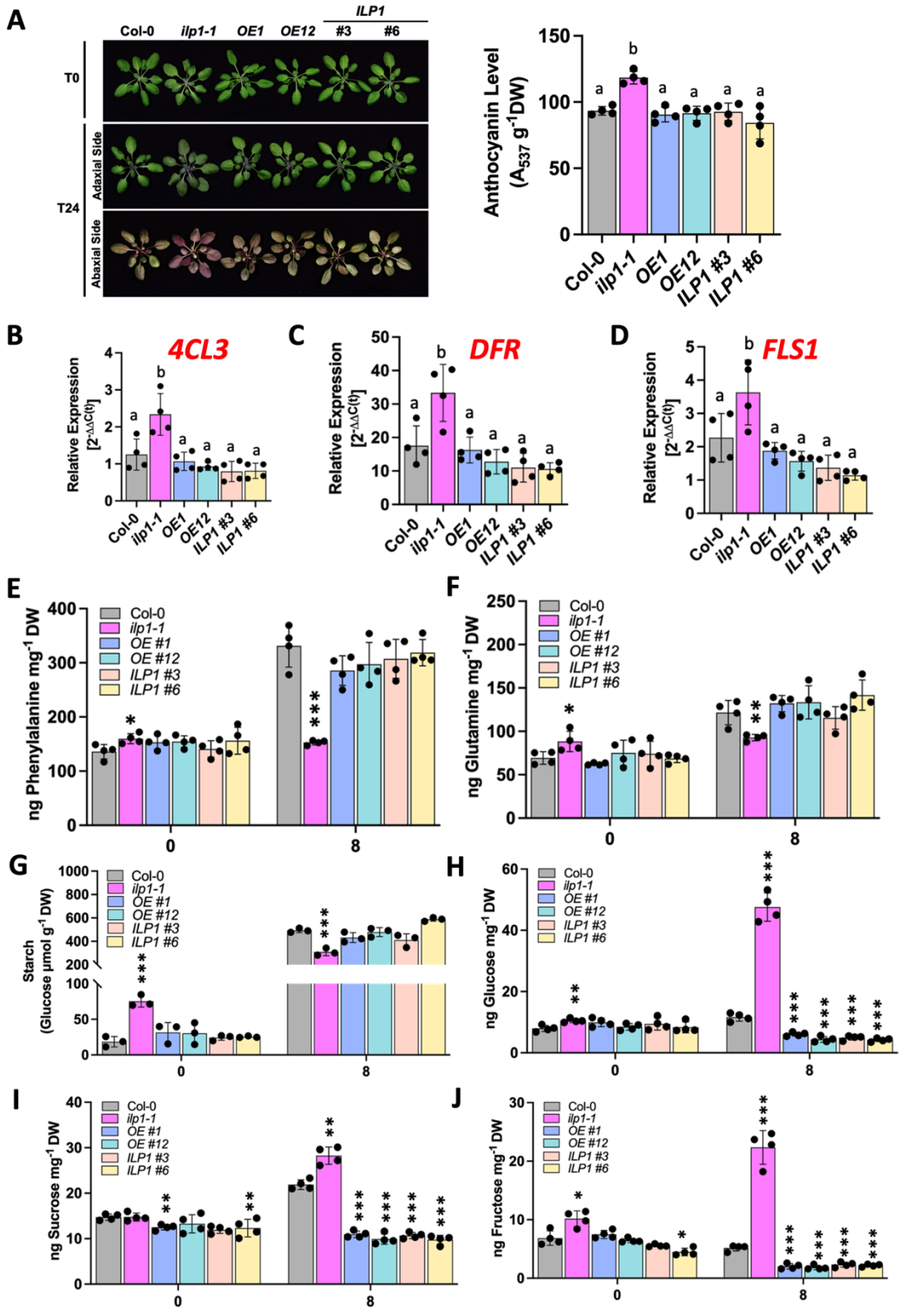

Figure 9. Phenotypic, transcriptomic, and metabolic analyses of the overexpression and genetic complementation lines. (A) Anthocyanin levels of 4-week-old plants after 24 hrs HL, relative expression levels of (B) *4CL3*, (C) *DFR*, and (D) *FLS1* after 8 hrs of HL, changes in metabolites like (E) phenylalanine and (F) glutamine before and after 8 hrs of HL, and (G) starch, (H) glucose, (I) sucrose, and (J) fructose levels before and after 8 hrs of HL exposure. Data are mean ± SD (n = 4). For B-D, different letters

indicate significance groups at $P < 0.05$ by Šidák's and Tukey's multiple comparison tests, respectively, as determined by two-way ANOVA. For E-J, asterisks indicate statistical significance compared to Col-0 by Student's t-test (*P <0.05, **P <0.01, ***P <0.001).

To test this speculation, the expression of *GPT2*, a notable gene that is differentially expressed in all timepoints in *ilp1-1* (Figure 6A, S4, S9G) was analyzed in more detail. Because the expression of *GPT2* has been reported before to be sugar-dependent, its levels were examined during EoN of a normal day-night cycle, a time when plants experience carbon starvation due to depleted starch and soluble sugars. At EoN, *GPT2* transcript levels in *ilp1-1* were 15-fold higher than in WT and were still significantly elevated after 2 hrs in normal light (NL) (Figure S13A). Interestingly, during HL exposure, *GPT2* expression was significantly repressed at all time points in both OE and complementation lines (Figure S13B), further reinforcing that *GPT2* expression depends on cellular sugar levels.

3.3 ILP1 localization and repressor activity

Yoshizumi et al. (2006) demonstrated that *ILP1* contains a nuclear localization sequence that directs it to the nucleus and that the GC-rich DNA binding domain in the C-terminal region of ILP1 functions as a transcriptional repressor in vitro and in vivo. To reconfirm this localization, *ILP1-GFP* was generated under the control of the 35S promoter and transiently expressed in tobacco leaves (Figure S14). ILP1-GFP was observed in the nucleus (red arrows) (Figure S14C). Additionally, partial colocalization was detected with the ER marker (HDEL-mCherry) and the plasma membrane marker (CBL1-OFP) (Figure S14A, S14B). Notably, a Z-stack projection of 10 different slices revealed net-like structures of ILP1 (yellow arrows) (Figure S14C), resembling cytoskeleton-localized proteins (Hackbusch et al., 2005; Cao, et al., 2016; Zang et al., 2021). These observations suggest that ILP1 may localize not only to the nucleus but also to other subcellular compartments, potentially performing functions other than splicing.

ILP1's function as a transcriptional repressor was also examined using a quantitative in vivo assay (Figure S15). In the absence of ILP1, *proPAP1:LUC*

exhibited a strong luminescent signal, with an intensity twice that of *proDFR:LUC*. However, in the presence of ILP1, both signals showed a slight reduction, suggesting a repressive effect on transcriptional activity. Based on the targeted transcriptomic and kinetic analysis of the anthocyanin biosynthetic pathway, *PAP1* and *DFR* were not differentially expressed at T0 in *ilp1-1*, indicating that there was no immediate effect of ILP1 on their transcription. However, differential expression was observed at later time points in *ilp1-1*, with *PAP1* becoming differentially expressed at T4 and *DFR* at T12 (Figure 4A, 4B, 5A). This temporal shift in gene expression suggests that ILP1 may exert its repressive effects in a time-dependent manner, most likely through indirect regulatory mechanisms. These results further underscores ILP1's function as a transcriptional repressor in vivo and suggest that it plays a role in modulating the expression of late biosynthetic genes in response to HL exposure, possibly through other transcriptional regulators such as MYBL2.

3.4 ILP1 truncated variants

To investigate the functions of the different ILP1 domains in greater detail, two independent lines of HA-tagged truncated ILP1 variants were generated (Figure 10A, S16A-S16B). Analysis of phenotypic traits revealed that No-N (without N-terminal domain) and No-GC (without GC-rich DNA binding domain) mutants, both containing a nuclear localization sequence (NLS), exhibited WT-like root length and rosette development (Figure S16C, S16D). In contrast, Only-GC mutants (with only GC-rich DNA binding domain), which lacks NLS, retained the *ilp1-1* mutant phenotype, indicating that the GC-rich DNA binding domain alone is insufficient to fully restore ILP1 function and suggests that nuclear localization is necessary for ILP1 to regulate developmental processes effectively.

Given that *ILP1* loss-of-function leads to overaccumulation of anthocyanins under HL exposure, the truncated variants were further examined to determine their role in anthocyanin regulation. After 24 hrs of HL, No-N accumulated anthocyanin levels comparable to WT (Figure 10B), indicating that this truncation does not disrupt ILP1-mediated regulation of anthocyanin biosynthesis. However, both No-GC and Only-GC mutants exhibited significantly higher anthocyanin accumulation than Col-0 and *ilp1-1*, suggesting that the GC-rich domain is essential for regulating

anthocyanin production. The elevated accumulation of anthocyanins in both No-GC and Only-GC mutants further implies that ILP1 nuclear localization is required for proper anthocyanin regulation and that its absence leads to deregulation of the pathway.

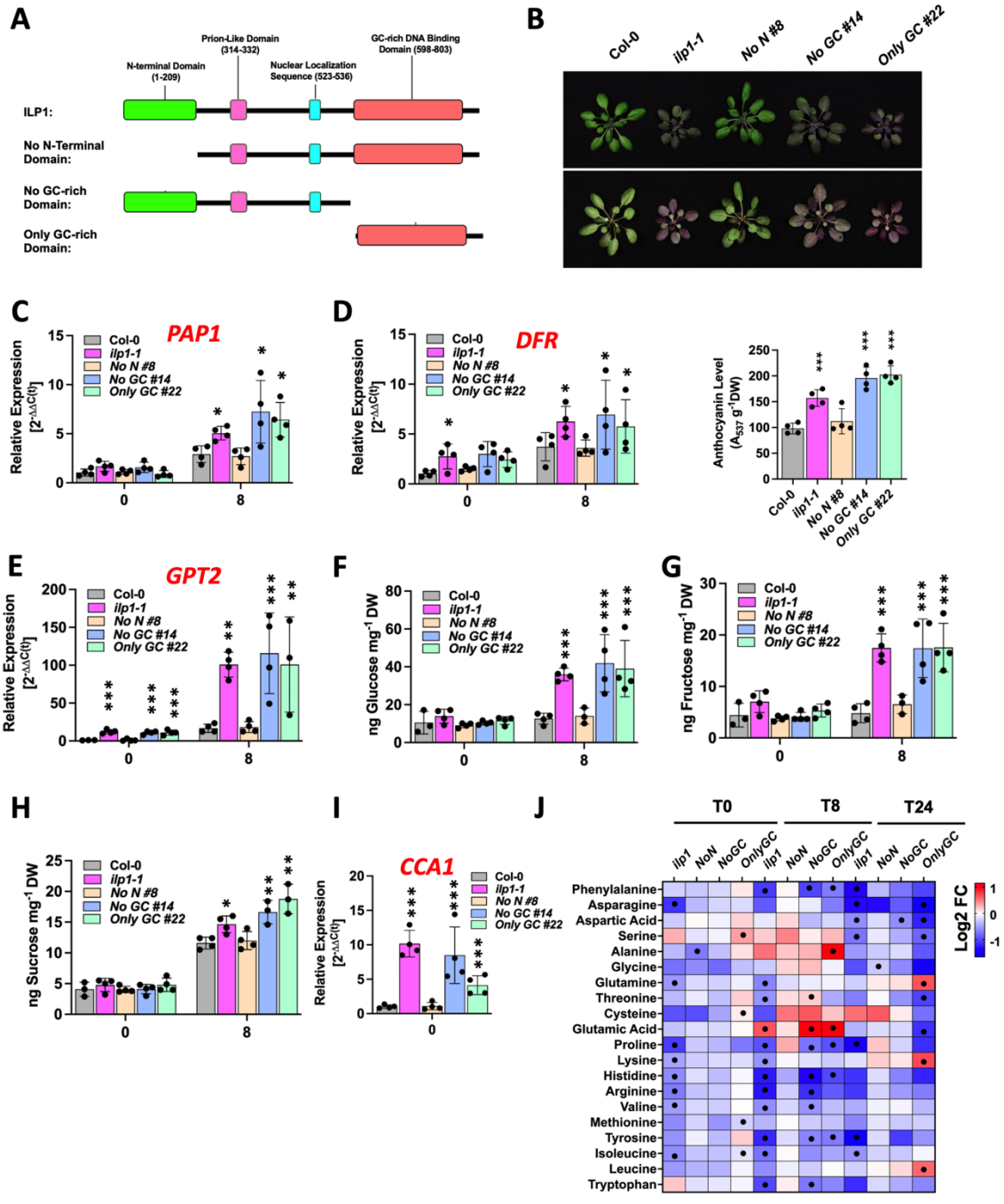

Figure 10. Comparative analysis of the truncated versions of ILP1. (A) Schematic diagram of the different truncations, (B) Anthocyanin levels 4-week-old plants after 24 hrs of HL, relative expressions of (C) *PAP1*, (D) *DFR*, and (E) *GPT2* before and after 8 hrs of HL, levels of (F) glucose, (G) fructose, and (H) sucrose before and after 8 hrs of HL, (I) splicing analysis of *CCA1*, and (J) log2FC of quantified amino acids before and after 8 hrs and 24 hrs of HL. Data are mean ± SD (n = 4). Asterisks indicate statistical significance compared

to Col-0 by Student's t-test (*P <0.05, **P <0.01, ***P <0.001). "•" in the heatmap indicates significance.

To decipher the molecular basis of anthocyanin overaccumulation in No-GC and Only-GC mutants, the core mRNA transcripts involved in anthocyanin biosynthesis such as *DFR* and *PAP1* were analyzed. Both truncated versions of ILP1 had higher relative expression levels of *PAP1* and *DFR* after 8 hrs of HL, closely resembling the expression profile observed in the *ilp1-1* mutant (Figure 10C, 10D). This pattern suggests that the GC-rich binding domain of ILP1 is essential for regulating the transcription of genes involved in anthocyanin biosynthetic pathway.

Additionally, *GPT2*, which has been identified as a sugar-dependent gene linked to carbon metabolism, exhibited an expression pattern in No-GC and Only-GC mutants similar to that in *ilp1-1* before and after 8 hrs of HL (Figure 10E). This observation reveals that both the GC-rich DNA binding domain of ILP1 and its nuclear localization might be integral in maintaining proper carbon metabolism.

To elucidate more in detail how the different domains of ILP1 contribute to its overall function in maintaining proper metabolic equilibrium during HL, both carbon and nitrogen pools during HL exposure were analyzed. Cytosolic sugars of No-GC and Only-GC mutants had similar levels compared to *ilp1-1* before and during HL while No-N mutant resembled the WT (Figure 10F-10H). The similar expression patterns of anthocyanin-related mRNA transcripts (*PAP1* and *DFR*) and the similar sugar levels in the No-GC and Only-GC mutants compared to *ilp1-1*, support the hypothesis that nuclear-localized ILP1 GC-rich domain represses transcriptional activation and sugar production, influencing carbon metabolism during HL.

Further analysis of log2 FC of quantified amino acids of both No-GC and Only-GC mutants displayed similar patterns of change like *ilp1-1*, especially after 8 hrs of HL (Figure 10J). Several amino acids, including phenylalanine, arginine, and glutamine, remained at lower levels in *ilp1-1* compared to WT, whereas glutamate exhibited a marked accumulation after 8 hrs of HL. These results collectively demonstrate the importance of the nuclear ILP1, specifically a functional GC-rich

DNA binding domain, in metabolic adjustment and anthocyanin biosynthesis during HL exposure.

3.5 Double point mutant of the PrD, $Q^{318,319}A$

Because there is still scarcity on the available knowledge about ILP1, its structural properties and biochemical behavior were analyzed using various bioinformatic tools. Using Alphafold (Jumper et al., 2021) and PONDR (Predictor Of Naturally Disordered Regions) algorithms (Xue et al., 2010), ILP1 was identified as an intrinsically disordered protein (IDP, 61.89% disordered) with three disordered regions (Figure S17A, S17B).

Aside from the previously characterized N- and C-terminal domains and NLS (Yoshizumi et al., 2006), further structural analysis using the Prion-Like Amino Acid Composition (PLAAC) algorithm (Lancaster et al., 2014) predicted the presence of a Prion-Like Domain (PrD) within the second intrinsically disordered region (IDR) (Figure S17B, S17C). The presence of PrDs in protein structures, particularly poly-glutamine (poly-Q) residues, has been shown to play an important role in driving liquid-liquid phase separation (LLPS) and regulating growth and development in plants (Jung et al., 2020).

To bring light how the PrD in ILP1 affects its overall function, two independent double mutant lines of HA-tagged residues Q318A and Q319A (referred to as $Q^{318,319}A$ hereafter) in the *ilp1-1* background (S17D, S17E) were generated. Based on the bioinformatic analysis, these point mutations were sufficient already to disrupt the PrD in ILP1 (Figure S17C). Phenotypic characterization of the mutants displayed WT-like root length, and rosette and flowering phenotypes (Figure S17F, S17G), indicating that this PrD is not required for normal growth and developmental processes. This also suggests that ILP1's role in these physiological aspects is independent of its prion-like characteristics.

To check if the poly-Q also plays a role in acclimation plasticity, anthocyanin accumulation was quantified in the $Q^{318,319}A$ point mutants following HL exposure. The analysis revealed that these mutants exhibited anthocyanin levels comparable

to WT (Figure S18A), suggesting that the poly-Q region is not required for anthocyanin regulation under HL conditions.

Relative expressions of genes involved in anthocyanin biosynthesis (*DFR*, *PAP1*, and *PAP2*) also showed WT-like increase after 8 hrs of HL in the poly-Q mutants (Figure S18B-S18D), indicating that the ILP1 PrD is not required for its transcriptional control over anthocyanin-related genes.

DELAY OF GERMINATION1 (*DOG1*) and *CIRCADIAN CLOCK ASSOCIATED1* (*CCA1*) which are misspliced in *ilp1-1* (Dolata et al., 2015) were also not misspliced in the $Q^{318,319}A$ mutants (Figure S18E, S18F), suggesting that this PrD does not play a significant role in ILP1-mediated gene regulatory mechanisms during acclimation response.

To determine whether mutating the PrD of ILP1 also disrupts metabolic equilibrium during HL response, the levels of starch and neutral sugars (fructose, glucose, sucrose) were quantified. In *ilp1-1*, starch content was higher before HL exposure, whereas cytosolic sugar levels increased after 8 hrs of HL (Figure S18G-S18J). In contrast, the $Q^{318,319}A$ mutants exhibited WT-like levels of starch and soluble sugars both before and during HL exposure (Figure S18G-S18J), suggesting that the PrD mutation does not affect carbon storage or sugar dynamics under HL conditions.

Analysis of amino acid content in $Q^{318,319}A$ mutants revealed a distinct pattern. Before HL exposure, amino acid levels closely resembled those observed in *ilp1-1*, but after 8 hrs of HL, they returned to WT-like levels (Figure S18K). This discrepancy indicates that while carbon metabolism remains unaffected, amino acid biosynthesis is perturbed in the absence of an intact PrD, particularly under normal conditions. These observations denote that the PrD is still an important ILP1 domain and that Q318 and Q319 are essential amino acid residues that play a role in maintaining proper amino acid production under normal conditions.

3.6 ILP1 and miRNA processing

ILP1 has been identified as a component of the non-canonical spliceosomal complex and has been implicated in miRNA biogenesis (Wang et al., 2019). To check whether miRNAs are also involved in HL acclimation response, a mutant of *SERRATE1* (*se1*), a core component of miRNA processing (Laubinger et al., 2008; Lobbes et al., 2006), was analyzed and its growth and acclimation responses were compared with those of *ilp1-1* under HL exposure.

Phenotypic analysis of *se1* revealed a distinct serrated rosette phenotype (Figure S19C) and a short hypocotyl length, similar to *ilp1-1* (Figure S19B). However, root length in *se1* remained comparable to WT (Figure S19A), indicating that *SERRATE1* mutation affects shoot development but does not significantly alter root growth.

Exposure of *se1* mutants to 24 hrs of HL revealed a markedly different acclimation response compared to *ilp1-1* (Figure S19C). Unlike *ilp1-1*, *se1* mutants exhibited WT-like anthocyanin accumulation (Figure S19C). The *se1* mutants also displayed WT-like transcript levels of key anthocyanin biosynthetic genes (Figure S19D-S19F) and normal amino acid profiles during HL acclimation (Figure S19G). These findings suggest that based on the analyzed parameters, miRNAs only play a minor role in ILP1-mediated acclimation responses, and that ILP1's function in HL acclimation may be more dependent on its regulatory role in alternative splicing, transcriptional repression, or metabolic reprogramming rather than direct involvement in miRNA-mediated pathways.

3.7 Splicing anomalies in *ilp1-1*

Previous studies by Dolata et al. (2015) demonstrated that knocking out *ILP1* leads to the missplicing of over a hundred genes, suggesting a significant role in pre-mRNA processing. To validate whether these reported misspliced transcripts are consistently affected and differentially regulated, *CCA1* was selected as a representative gene for further analysis.

CCA1 contains an intron retention event in intron 6 (Dolata et al., 2015), making it an ideal candidate for assessing ILP1's impact on splicing fidelity. To detect potential splicing defects, primers were designed to span exon 6 and intron 6, where ILP1-dependent missplicing was previously reported. Expression analysis revealed that the *ilp1-1* mutant, along with the truncated No-GC and Only-GC mutants, exhibited significantly higher expression levels of *CCA1* compared to WT (Figure 10I). This increased expression indicates that intron 6 retention occurs in these mutants, further confirming that ILP1 is required for proper splicing of *CCA1* pre-mRNA.

To determine the extent of missplicing in *ilp1-1* during HL acclimation, various types of alternative splicing (AS) events were analyzed (Figure S20). Among the different classes of alternative splicing, intron retention (RI) was the most prevalent form of missplicing, with a substantial number of differentially spliced transcripts detected before and during HL exposure, and throughout the recovery phase (Figure S20A). The persistent accumulation of transcripts with retained introns suggests a widespread splicing defect in *ilp1-1*, potentially affecting multiple biological pathways critical for HL acclimation.

In addition to RI, other types of splicing anomalies were also detected. Exon skipping (SE) accounted for approximately 500 misspliced transcripts before HL exposure, further indicating that ILP1 deficiency disrupts normal exon recognition and processing. Additionally, alternative 3' and 5' splice site selection (A3S and A5S, respectively) contributed to splicing defects, though to a lesser extent than RI and SE.

Since RI events were the most dominant and widespread variant of missplicing across all timepoints, further analysis was conducted to identify genes consistently affected by this splicing anomaly. Comparative analysis revealed a set of 45 common genes exhibiting persistent intron retention throughout HL acclimation and recovery phase (Figure S20B). Among these is *REVEILLE8* (*RVE8*), a MYB-like transcription factor similar to *CCA1* that regulates the circadian clock by modulating the pattern of histone 3 (H3) acetylation (Farinas and Paloma, 2011). The presence of intron retention in both *RVE8* and *CCA1* transcripts suggests that ILP1 dysfunction impairs proper splicing of circadian clock-associated genes, possibly

disrupting clock-controlled metabolic and developmental processes such as flowering time. This splicing defect may also contribute to the late flowering phenotype observed in *ilp1-1* (Figure 3E), highlighting the essential role of ILP1 in coordinating circadian-controlled developmental transitions.

Recent findings have indicated a lack of correlation between gene expression levels and alternative splicing events in *ilp1-1* at a global scale during HL acclimation (Araguirang et al., 2024). To further investigate the functional significance of ILP1-mediated alternative splicing, GO-term enrichment analysis was performed at T0 and T8, focusing specifically on transcripts exhibiting intron retention. At T0, a substantial proportion of mRNA transcripts with retained introns were associated with RNA splicing regulation, spliceosome-mediated mRNA splicing, mRNA metabolic processes, and both primary and specialized metabolism (Figure S20C). These findings suggest that, under normal conditions, ILP1 plays a critical role in maintaining the fidelity of splicing events, particularly for transcripts involved in RNA processing and metabolic regulation.

After 8 hrs of HL exposure, the majority of transcripts exhibiting intron retention were enriched for biological processes related to primary metabolism, mRNA stability, and mRNA-related metabolic functions (Figure S20D). This shift in functional enrichment indicates that HL acclimation influences the spectrum of misspliced transcripts, with ILP1 loss-of-function affecting genes crucial for metabolic adaptation and mRNA homeostasis.

Taken together, these results reveal that ILP1 deficiency broadly disrupts pre-mRNA processing and suggest that ILP1 is integral for maintaining splicing accuracy, not only under normal conditions but also in response to HL exposure and subsequent recovery phase. Its loss of function also leads to the accumulation of improperly processed transcripts, which contribute to broader physiological and metabolic defects observed in HL acclimation responses.

3.8 Spliceosomal complex components

The splicing analysis revealed a significant enrichment of transcripts associated with mRNA splicing via the spliceosome (Figure S20C). This finding suggests that

spliceosome-mediated regulation plays a crucial role in transcriptome dynamics, particularly under HL conditions. To uncover whether deficiencies of other spliceosome components influence the ability of plants to adapt to HL exposure, mutants of various spliceosome-associated proteins were examined.

3.8.1 ILP1 and NTR1

NTR1 has been reported to physically and directly interact with ILP1 in the nucleus as components of the intron lariat spliceosome (ILS) (Wang et al., 2019), suggesting a potential functional link between these two proteins during HL acclimation. To further investigate this relationship, the growth phenotypes of *ilp1-1* and a knockout mutant allele of *NTR, ntr1-1* (Figure S21A) were analyzed. Both mutants exhibited short root and hypocotyl phenotypes, indicating a shared role in developmental regulation (Figure 11A, 11B). As an additional control to rule out the impact of anthocyanin biosynthesis induction on sugar content in the spliceosome mutants, *pap1-D*, a mutant with constitutive anthocyanin accumulation, was also included in the analysis (Figure 11D).

Upon HL exposure, both *ilp1-1* and *ntr1-1* accumulated significantly higher levels of anthocyanins than WT (Figure 11D), correlating with an increase in the transcript levels of key anthocyanin biosynthetic genes (*DFR*, *PAP1*, and *FLS1*) after 8 hrs of HL (Figure 11I-11K). This parallel response suggests that ILP1 and NTR1 function in a common pathway regulating anthocyanin biosynthesis under HL conditions.

In addition to their similar anthocyanin accumulation patterns, *ilp1-1* and *ntr1-1* mutants also exhibited identical metabolic responses, particularly in terms of starch and cytosolic sugar dynamics (Figure 11E-11H) and amino acid production during HL (Figure 11C). Both mutants displayed a significant increase in fructose, glucose, and sucrose after 8 hrs of HL, along with high levels of glutamic acid, while most other amino acids decreased (Figure 11C). These findings suggest that ILP1 and NTR1 collectively influence carbon and nitrogen metabolism during HL.

Interestingly, unlike *ilp1-1* and *ntr1-1*, the *pap1-D* mutant, despite accumulating high levels of anthocyanins, exhibited a WT-like metabolic profiles at the carbon and

nitrogen level, resembling Col-0 rather than *ilp1-1* and *ntr1-1* (Figure 11C, 11F-11H). This distinction suggests that excessive anthocyanin accumulation alone is not responsible for the metabolic imbalance observed in *ilp1-1* and *ntr1-1*. Instead, the perturbations in carbon and nitrogen metabolism are likely a consequence of *ILP1* and *NTR1* mutation, emphasizing their broader role beyond anthocyanin biosynthesis, potentially in metabolic regulation and HL acclimation.

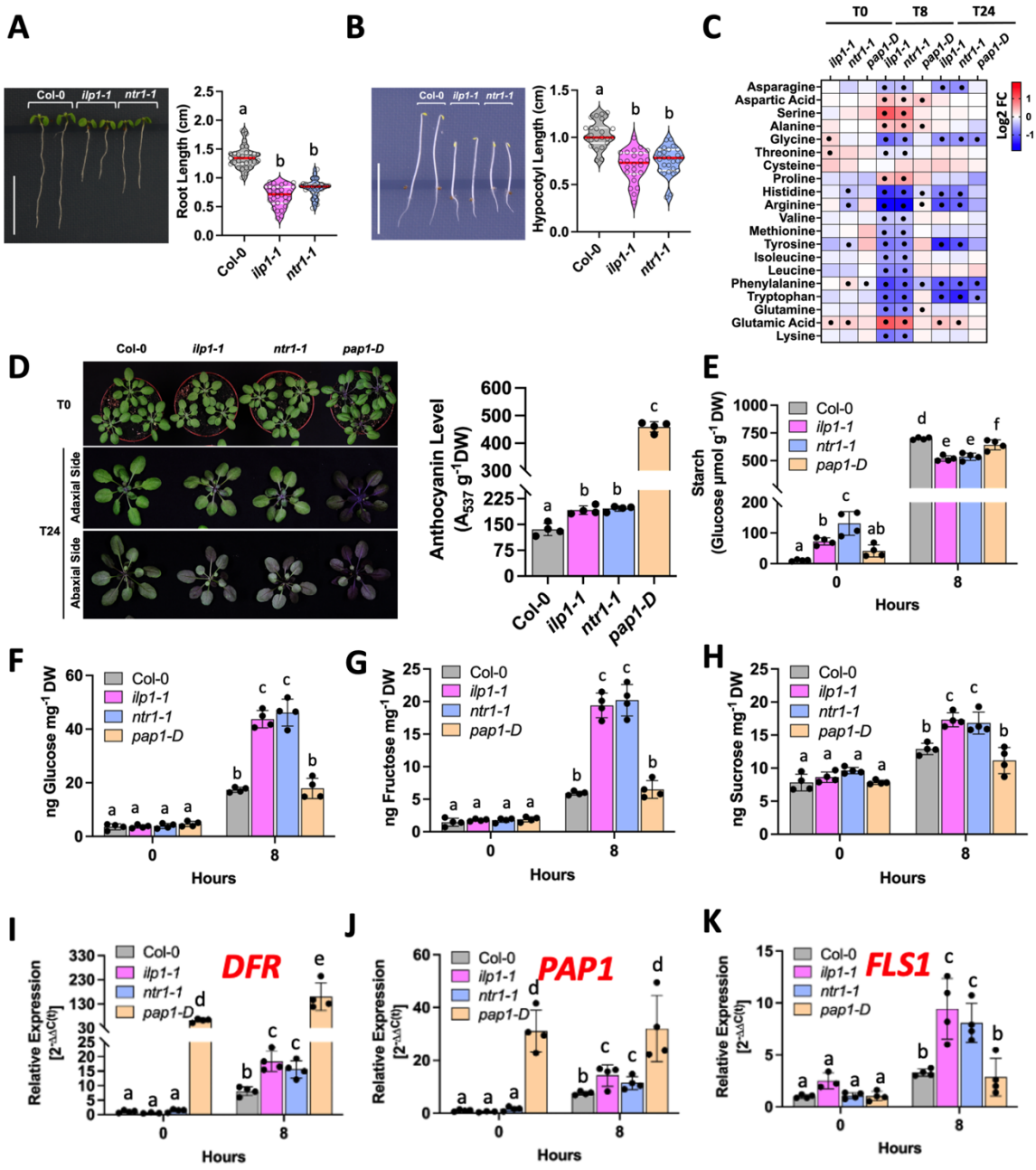

Figure 11. *ntr1-1* mutant resembles the phenotypes of *ilp1-1*. (A) Root lengths of 6DAG seedlings, (B) hypocotyl lengths of 4DAG dark-grown seedlings, (C) log2 FC of amino acid contents at different timepoints, (D) anthocyanin levels of 4-week-old plants after HL exposure, (E) starch contents and (F) glucose, (G) fructose, and (H) sucrose levels before

and after 8 hrs of HL, and relative expressions of (I) *DFR*, (J) *PAP*1, and (K) *FLS1* after 8 hrs of HL. For D-K, data are mean ± SD (n = 4). The red lines inside the violins show the median of values and the white lines the quartiles. Different letters indicate significance groups at $P < 0.05$ by Šidák's and Tukey's multiple comparison tests, respectively, as determined by two-way ANOVA. "●" in the heatmap indicates significance.

3.8.2 ILP1 and PRL1

Isolation of the different *raa* mutants led to the identification of *raa7* and *raa14* as allelic mutants of another spliceosomal component called *Pleiotropic Regulatory Locus1* (*PRL1*). *PRL1* has also been shown to maintain cortical actin integrity for root development (Wang et al., 2024a) and positively regulate the accumulation of small RNAs, including miRNAs and siRNAs (Zhang et al., 2014a). To examine how a non-functional allele of *PRL1* affects the ability of plants to acclimate during HL, the *prl1-2* mutant (Figure S21B) was compared with *ilp1-1* and *ntr1-1*.

Phenotypic characterization revealed that *prl1-2* exhibited shorter root and hypocotyl growth compared to WT and were even shorter than *ilp1-1* and *ntr1-1*, indicating a more severe developmental impairment (Figure 12A, 12B). Beyond its stunted growth, *prl1-2* also accumulated higher anthocyanin levels than *ilp1-1* after 24 hrs of HL exposure (Figure 12C). The expression of key anthocyanin biosynthetic genes, including *DFR* (Figure 12H) and *PAP1* (Figure 12I), showed more than a 20% increase in mRNA levels compared to the WT, suggesting an enhanced transcriptional activation of the anthocyanin pathway.

Sugar metabolism was also disrupted in *prl1-2*, mirroring the starch and cytosolic sugar profiles observed in *ilp1-1* (Figure 12D-12G). After 8 hrs of HL exposure, both *ilp1-1* and *prl1-2* also exhibited similar metabolic responses, characterized by the accumulation of high levels of amino acids such as aspartic acid and proline, alongside a reduction in histidine and arginine levels (Figure 12J).

Taken together, these results indicate that PRL1, like ILP1 and NTR1, is also essential in maintaining metabolic equilibrium during HL acclimation. The shared metabolic and transcriptomic responses among these mutants highlight the global function of the spliceosomal complex in the regulation of anthocyanin biosynthesis and carbon-nitrogen balance during HL exposure.

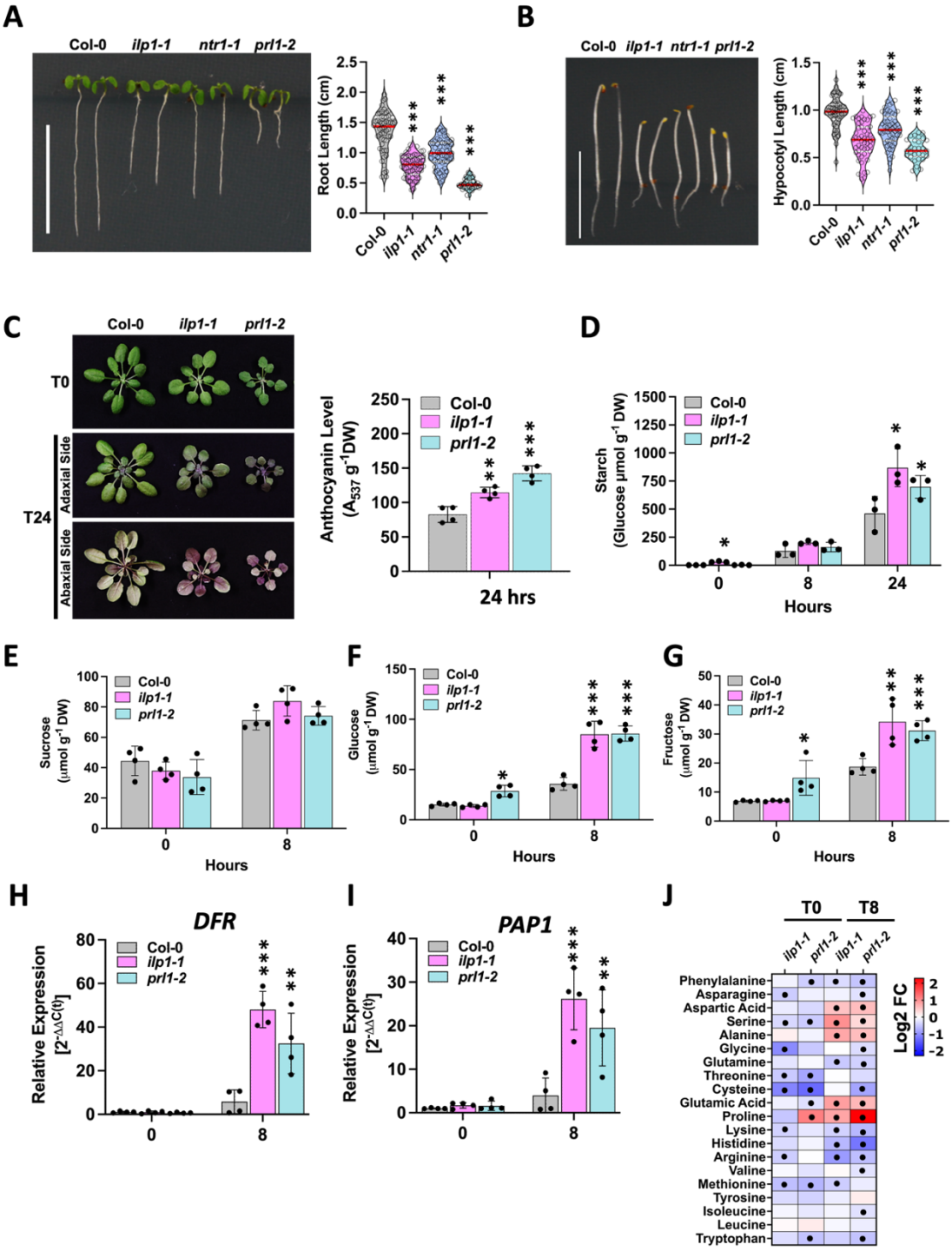

Figure 12. Mutation in *PRL1* also shows defective acclimation response. (A) Root lengths of 7 DAG seedlings, (B) hypocotyl of 4 DAG dark-grown seedlings, (C) anthocyanin levels of 4-week-old plants after 24 hrs of HL, levels of (D) starch, (E) sucrose, (F) glucose, and (G) fructose before and after 8 hrs of HL, relative expressions of (H) *DFR* and (I) *PAPI* before and after 8 hrs of HL, and (J) log2 FC of quantified amino acids before and after 8 hrs of amino acids. For C-I, data are mean ± SD (n = 4). The red lines inside the violins show the median of values and the white lines the quartiles. Asterisks indicate statistical significance compared to Col-0 by Student's t-test (**P* <0.05, ***P* <0.01, ****P* <0.001). "•" in the heatmap indicates significance.

3.8.3 ILP1 and PRP8

After recognizing that mutants of *PRL1*, *ILP1*, and *NTR1* shared similar acclimation responses, a broader screening of multiple spliceosomal mutants involved in different stages of the splicing cycle was further conducted. This analysis identified two allelic mutants, *prp8-7* and *prp8-12*, of *Pre-mRNA-Processing 8* (*PRP8*) showed a contrasting phenotypic response during HL exposure.

PRP8, a 275-kDa protein, is the largest and most highly conserved protein component that homes at the very core of the spliceosomal complex (Kuhn et al., 2002; Grainger and Beggs, 2005; Figure S22A). Both *prp8-7* and *prp8-12* are point mutants of the same amino acid (G1820), which resides at its catalytic core (Figure S22B). The GGA-to-AGA mutation in *prp8-7* led to a missense mutation, changing glycine to glutamic acid (G1820E) while GGA-to-GAA mutation in *prp8-12* replaced glycine with arginine (G1820R) (Figure S22C), substitutions that are oppositely charged with each other.

To elaborate in greater detail whether the charge-dependent conformational changes in PRP8 influence acclimation responses, a comparative analysis was conducted among WT, *prp8-7*, *prp8-12*, and *ilp1-1*. Phenotypic evaluation revealed that both *prp8-7* and *prp8-12* exhibited a shorter root phenotype than WT, although root length remained slightly longer than that of *ilp1-1* (Figure 13A). Additionally, rosette size in both *prp8* mutants was comparable to *ilp1-1*, further indicating that these mutations affect vegetative development (Figure 13B). However, flowering time remained WT-like in both *prp8-7* and *prp8-12*, distinguishing them from the delayed flowering phenotype observed in *ilp1-1* (Figure S22D).

After 24 hrs of HL exposure, *prp8-12* exhibited anthocyanin accumulation levels comparable to *ilp1-1*, whereas *prp8-7* displayed a markedly repressed anthocyanin response (Figure 13B). This contrast in anthocyanin accumulation suggests that the G1820R (*prp8-12*) and G1820E (*prp8-7*) substitutions differentially impact spliceosome-mediated HL acclimation, with *prp8-12* mirroring *ilp1-1* response and *prp8-7* exhibiting an attenuated response.

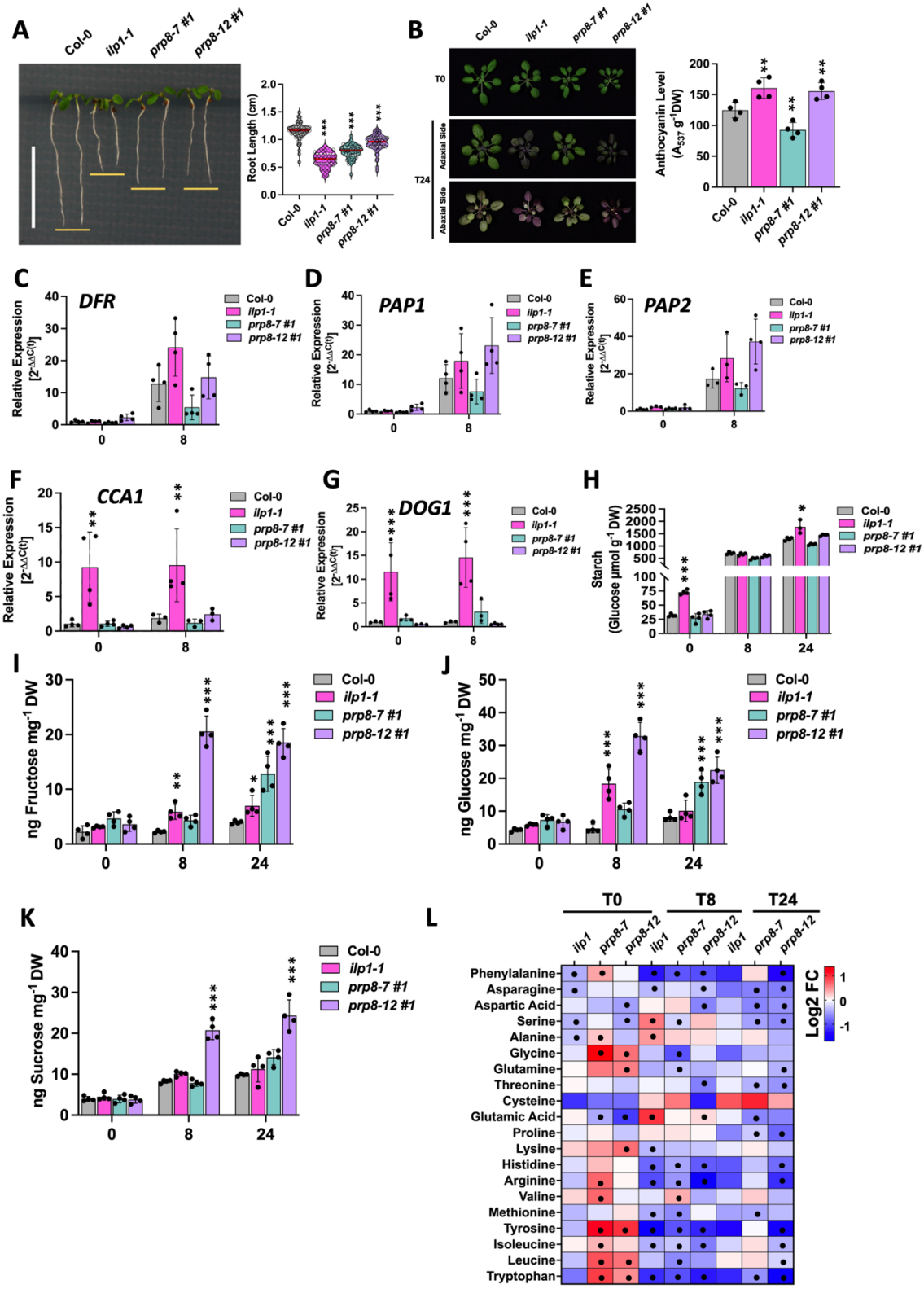

Figure 13. Two different mutant alleles of *PRP8* displayed different responses to high light. (A) Root lengths of 7DAG seedlings, (B) anthocyanin content phenotype after 24 hrs of HL, relative expressions of anthocyanin biosynthetic genes (C) *DFR*, (D) *PAP1*, and (E) PAP2 and relative expressions of genes that are misspliced in *ilp1-1* (F) *CCA1* and (G) *DOG1*, contents of (H) starch, (I) fructose, (J) glucose, (K) sucrose before and after 8 hrs

and 24 hrs of HL, and log2 FC of quantified amino acids before and after 8 hrs and 24 hrs of HL. For B-K, data are mean ± SD (n = 4). The red lines inside the violins show the median of values and the white lines the quartiles. Asterisks indicate statistical significance compared to Col-0 by Student's t-test (*P <0.05, **P <0.01, ***P <0.001). "●" in the heatmap indicates significance.

Further analysis of anthocyanin biosynthetic gene expression revealed that *DFR*, *PAP1*, and *PAP2* transcript levels in *prp8-12* closely resembled those of *ilp1-1*, reinforcing the observation that the *prp8-12* mutant follows a similar regulatory trajectory as *ilp1-1* in HL-induced anthocyanin production (Figure 13C-13E). In contrast, *prp8-7* displayed more repressed gene expression than WT, aligning with its lower anthocyanin accumulation after HL exposure. These findings indicate that the specific charge introduced by the G1820 mutation within PRP8's catalytic site plays a key role in determining the extent of anthocyanin biosynthesis activation during HL acclimation.

To examine if the misspliced variants in *ilp1-1* were also misspliced in the *prp8* mutants, *CCA1* and *DOG1* transcripts were analyzed. Compared to *ilp1-1*, analysis of *CCA1* and *DOG1* revealed that splicing defects were absent in both *prp8* mutants (Figure 13F, 13G). This observation supports previous studies that missense alleles in *prp8* can restore splicing of a subset of misspliced mRNAs and increase splicing fidelity by reducing the use of novel splice sites (Cabezas-Fuster et al., 2022; Llinas et al., 2022).

To determine the impact of *prp8* mutations in primary metabolism during HL, starch, cytosolic sugars, and amino acids were quantified. The *prp8-12* mutant exhibited starch accumulation levels similar to *ilp1-1*, along with elevated cytosolic sugar content (Figure 13H-13K). This suggests that PRP8 mutations impact sugar partitioning and storage dynamics, most likely through alterations in the regulation of transcripts involved in metabolic pathways.

Amino acid profiling further revealed that at T0, both *prp8* mutants exhibited higher total amino acid content than *ilp1-1*, with *prp8-7* displaying the most elevated levels (Figure 13L). However, the *prp8* mutants also displayed altered amino acid homeostasis during HL, with levels progressively decreasing at 8 hrs of HL exposure, indicating that PRP8 mutations alter the balance among amino acid synthesis, degradation, and redistribution during HL acclimation. The observed

metabolic patterns also imply that PRP8 plays a role in maintaining nitrogen metabolism, not only during HL stress responses but also under non-stress conditions, ensuring proper regulation of amino acid pools for metabolic flexibility. Taken together, these results suggest that structural modifications in PRP8 due to missense mutations can significantly impact nitrogen metabolism, further reinforcing the critical role of spliceosomal regulation in metabolic adaptation during HL acclimation.

3.9 Virus-Induced Gene Silencing lines

Wang et al. (2009) further showed that the double knockout mutant *ilp1-1 ntr1-1* is embryonic lethal, highlighting the essential role of these genes in embryonic development. To shed light on how the simultaneous loss of ILP1 and NTR1 affects growth and development, an alternative approach was employed using Virus-Induced Gene Silencing (VIGS) (Burch-Smith et al., 2006; Liu et al., 2002). This method allowed the targeted suppression of *ILP1* expression in the *ntr1-1* knockout background, circumventing the lethality associated with the double knockout mutation.

Successfully silenced *ntr1-1* plants infected with *TRV2-ILP1* exhibited severe growth defects, characterized by stunted development and curling of younger leaves (Figure 14A). Expression analysis confirmed the effective downregulation of *ILP1* in these VIGS mutants (Figure S23A), suggesting that simultaneous disruption of *ILP1* and *NTR1* results in additive developmental abnormalities.

Given that both *ilp1-1* and *ntr1-1* mutants exhibited anthocyanin overaccumulation after 24 hrs of HL exposure, further analysis was conducted to determine whether the VIGS mutants would display a similar or enhanced response. Surprisingly, these mutants showed a three-fold suppression of anthocyanin accumulation after 24 hrs of HL exposure compared to the single mutants (Figure 14B). To understand the underlying physiological mechanisms, anthocyanin biosynthetic gene expression was examined before and during HL acclimation. Expression levels of key regulatory genes such as *PAP1* and *DFR* remained comparable to WT levels both before and after 8 hours of HL exposure (Figure S23B, S23C). These results

suggest that ILP1 and NTR1 together play a critical role in activating anthocyanin biosynthesis under HL stress, and their simultaneous suppression disrupts the ability to upregulate anthocyanin-related transcriptional networks during HL exposure.

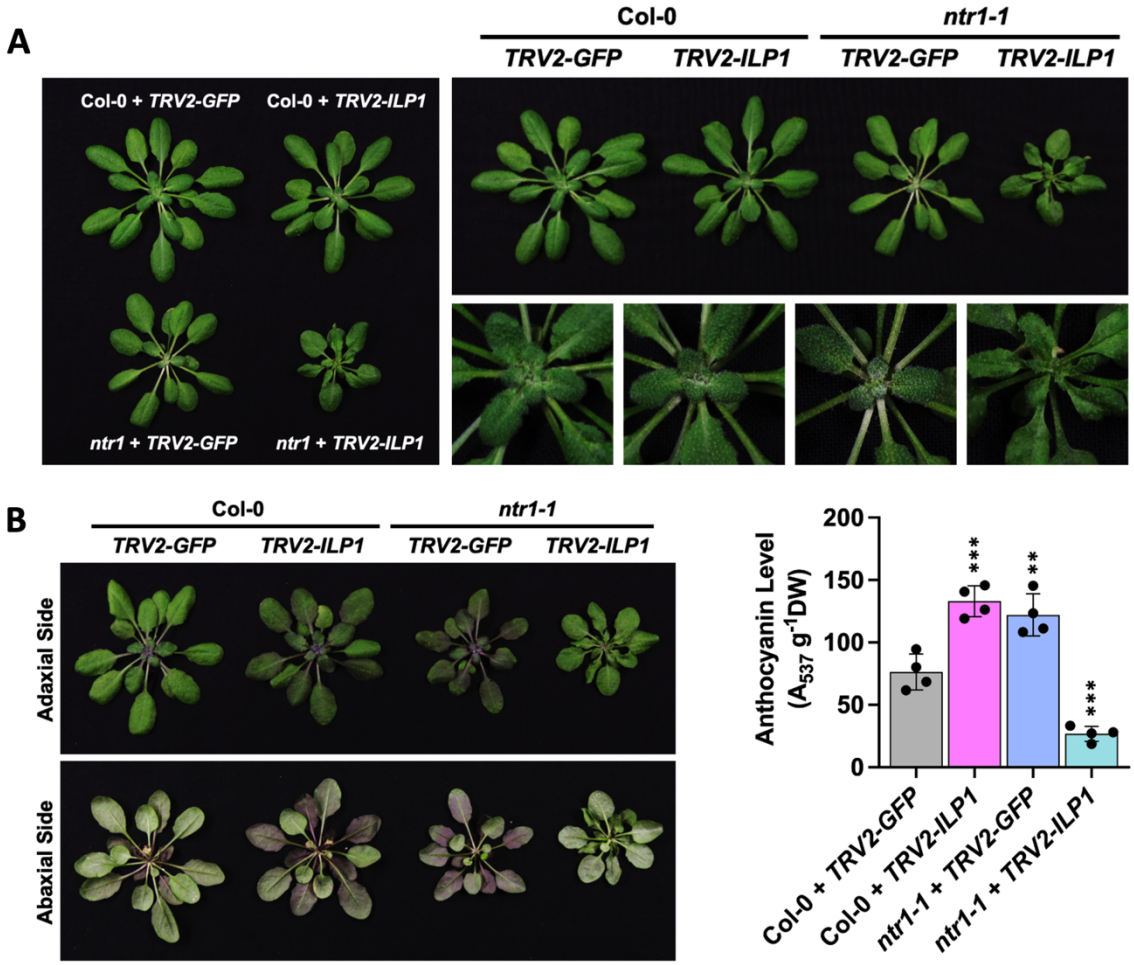

Figure 14. Phenotypes of the silenced plants before and after HL exposure. (A) Rosette phenotypes of 6-week-old plants showing the curling of the younger leaves and (B) anthocyanin phenotypes after 24 hrs of HL. Data are mean ± SD (n = 4). Asterisks indicate statistical significance compared to Col-0 by Student's t-test (*P <0.05, **P <0.01, ***P <0.001).

Metabolite quantification further revealed that amino acid levels in *ilp1-1*, *ntr1-1*, and VIGS mutants were already lower than WT levels even before HL exposure. Notably, after 8 hrs of HL, amino acid levels in VIGS mutants remained suppressed, while certain metabolites in *ilp1-1* and *ntr1-1* started to recover. This suggests that the absence of both ILP1 and NTR1 leads to a prolonged disruption in amino acid

homeostasis, impairing the plant's ability to restore normal metabolic functions after HL exposure.

These findings collectively demonstrate that loss or reduced functionality of both ILP1 and NTR1 causes severe developmental abnormalities, suppression of HL-induced acclimation responses, and prolonged metabolic imbalance. The unexpected repression of anthocyanin accumulation in VIGS mutants, despite the individual overaccumulation phenotypes of *ilp1-1* and *ntr1-1*, suggests that ILP1 and NTR1 interact in a complex regulatory network that governs HL acclimation responses at multiple levels, including transcriptional regulation, alternative splicing, and metabolic coordination.

3.10 Nitrogen metabolism in spliceosome mutants

The consistently observed lower amino acid levels in *ilp1-1* suggested a potential limitation in nitrogen transport or metabolism, raising the possibility that knocking out *ILP1* affects nitrogen homeostasis during both growth and HL acclimation. To test this hypothesis, the impact of nitrogen availability on root development and overall growth was assessed in *ilp1-1*, along with *ntr1-1* and *prl1-2* mutants. Growth responses were compared across media containing no nitrogen (No N) and increasing nitrogen concentrations (10%, 50%, and 100% of the nitrogen content in commercial MS media) (Figure 15A).

In the No N media, WT, *ilp1-1*, and *ntr1-1* displayed early chlorosis or yellowing of the leaves, a typical hallmark of nitrogen deprivation. Additionally, root growth in WT was significantly reduced in the No N media, showing no difference compared to *ilp1-1* and *ntr1-1* (Figure 15A), suggesting that nitrogen limitation affects root elongation across genotypes.

On the other hand, a strikingly different response was observed in *prl1-2*, where no root growth occurred under nitrogen-free conditions, indicating that nitrogen is essential for root initiation in this mutant. This severe phenotype suggests that PRL1 plays a critical role in nitrogen-dependent root development, possibly by regulating the splicing or expression of genes involved in nitrogen assimilation and root meristem activity.

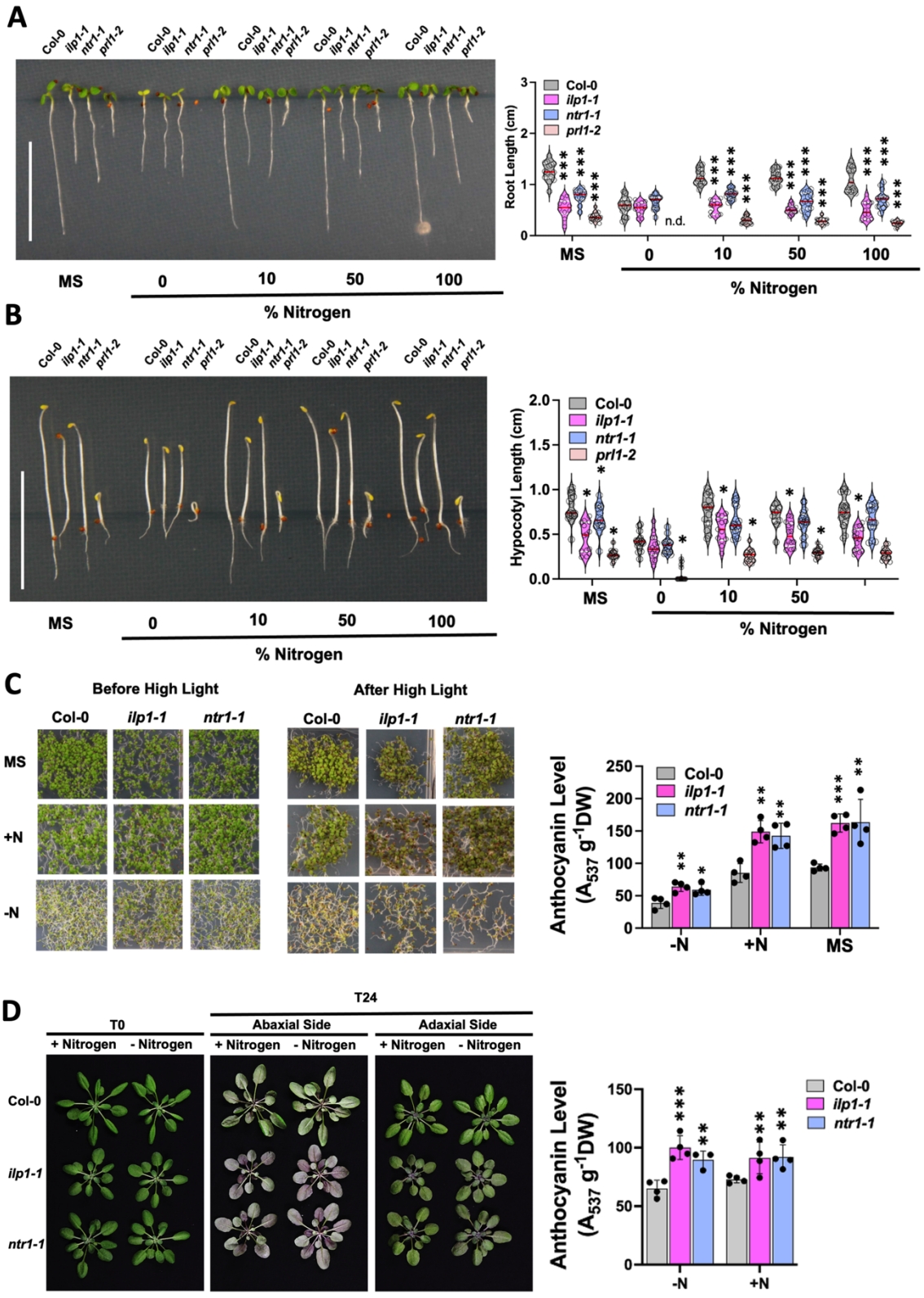

Figure 15. Growth and acclimation responses in the presence or absence of nitrogen. (A) Root lengths of 7DAG seedlings in the presence of increasing concentration of nitrogen, (B) hypocotyl lengths 4DAG dark-grown seedlings in the presence of increasing concentration of nitrogen, (C) anthocyanin contents of 7DAG seedlings grown in MS, and with or without nitrogen, and (D) anthocyanin contents of 4-week-old plants grown with

or without nitrogen (0.2 N g L^{-1} fertilizer). For C and D, data are mean ± SD (n = 4). The red lines inside the violins show the median of values and the white lines the quartiles. Asterisks indicate statistical significance compared to Col-0 by Student's t-test (*P <0.05, **P <0.01, ***P <0.001).

At 10% nitrogen concentration, WT root growth was fully restored, highlighting that a minimal nitrogen supply is sufficient to resume normal development (Figure 15A). Similarly, in *prl1-2* mutants, 10% nitrogen was also sufficient for root growth initiation (Figure 15A), confirming that the absence of PRL1-dependent processes can be partially compensated by an external nitrogen source. However, unlike WT and *prl1-2*, *ilp1-1* and *ntr1-1* mutants exhibited no improvement in root growth nor elongation, regardless of nitrogen availability (Figure 15A), suggesting that the lack of nitrogen is not the causative factor for the short root phenotype of both *ilp1-1* and *ntr1-1*.

Similar to root growth, hypocotyl lengths of WT, *ilp1-1*, *ntr1-1*, and *prl1-2* in the 0% nitrogen showed a decrease in the average length after 4 days of incubation in the dark (Figure 15B). But unlike roots of *prl1-2* that were not able to initiate growth and elongation in the No N media, hypocotyl elongation was observed partially among the pool of *prl1-2* seedlings. This suggests that shoot elongation mechanisms remain partially functional in *prl1-2*, despite severe nitrogen limitations affecting root initiation.

Increasing the concentration of nitrogen to at least 10% already reverted the hypocotyl lengths of all genotypes back to measured lengths in MS-grown seedlings. This response indicates that even minimal nitrogen availability is sufficient to restore normal hypocotyl elongation, underpinning the necessity of nitrogen for coordinated seedling development.

Additionally, these root and hypocotyl experiments with increasing nitrogen concentrations highlight two key observations that (1) despite nitrogen deprivation, *prl1-2* seedlings can still undergo skotomorphogenesis, demonstrating that hypocotyl elongation mechanisms remain partially independent of nitrogen availability and (2) nitrogen is essential for proper root initiation and sustained hypocotyl elongation, signifying that distinct nitrogen-dependent regulatory pathways govern shoot and root development.

Previous studies showed that nitrogen deprivation can trigger anthocyanin accumulation (Lea et al., 2007; Liang and He, 2018; Liao et al., 2022). To determine whether nitrogen deficiency is responsible for the elevated anthocyanin levels observed in *ilp-1* and *ntr1-1* during HL acclimation, exogenous nitrogen was supplied to both seedlings and mature plants throughout developmental stages before HL exposure. Despite the continuous availability of nitrogen, *ilp1-1* and *ntr1-1* seedlings exhibited elevated anthocyanin accumulation across all conditions, including without nitrogen (-N), nitrogen-supplemented (+N), and MS media (Figure 15C). These results indicate that anthocyanin overaccumulation in *ilp1-1* and *ntr1-1* seedlings is not a consequence of nitrogen limitation. Instead, the high anthocyanin levels observed in these mutants likely result from defects in alternative regulatory mechanisms, such as transcriptional or post-transcriptional control of anthocyanin biosynthesis and metabolic imbalances, rather than nutrient availability.

In mature plants, a similar trend for the untreated and nitrogen-supplemented trays (0.02% nitrogen) was observed. Both *ilp1-1* and *ntr1-1* accumulated higher levels of anthocyanins in the two set-ups compared to WT after 24 hrs of HL exposure (Figure 15D). Further analysis of nitrogen, carbon, and sulfur content (Figure S24F), along with total protein levels in WT, *ilp1-1*, and *ntr1-1* (Figure S24F), revealed no significant differences among genotypes, suggesting that even in later developmental stages, nitrogen deficiency is not the underlying factor driving excessive anthocyanin accumulation in *ilp1-1* and *ntr1-1* during HL acclimation.

Given the apparent abnormalities in amino acid biosynthesis, pyridoxal-5'-phosphate (PLP) was hypothesized to be involved, as it serves as a key cofactor for multiple aminotransferases essential in amino acid metabolism (Eliot and Kirsch, 2004). To check this possibility, the expression levels of enzymes involved in PLP biosynthesis and aminotransferases responsible for amino acid production were analyzed. Among all the genes observed, *PS2* or *PYROPHOSPHATE-SPECIFIC PHOSPHATE1* from PLP biosynthesis showed significant upregulation across all time points (Figure S24C, S24D). This indicates that PLP biosynthesis may be disrupted, potentially leading to imbalanced cofactor availability, which could impact aminotransferase activity and amino acid homeostasis.

To determine whether PLP availability influences growth phenotypes, increasing concentrations of exogenous PLP were supplied to *ilp1-1*, *ntr1-1*, and *prl1-2* mutants. However, PLP supplementation in MS media failed to restore root phenotypes (Figure S24A). Root lengths of *ilp1-1*, *ntr1-1*, and *prl1-2* remained relatively unchanged across all PLP concentrations, suggesting that deficiencies in PLP-dependent enzymatic activity do not directly contribute to the short-root phenotype of these mutants.

Similarly, hypocotyl elongation in WT, *ilp1-1*, *ntr1-1*, and *prl1-2* showed no significant differences between the mock treatment and PLP-supplemented conditions. After four days of dark incubation, hypocotyls of *ilp1-1*, *ntr1-1*, and *prl1-2* remained shorter than WT, with *prl1-2* exhibiting the most severe reduction in hypocotyl length (Figure S24B). These results indicate that PLP supplementation does not rescue the hypocotyl elongation defects, further suggesting that the root and hypocotyl growth impairments are not directly caused by PLP deficiency.

To resolve whether PLP deficiency contributes to anthocyanin overaccumulation in *ilp1-1*, *ntr1-1*, and *prl1-2* during HL exposure, exogenous PLP was supplemented to these mutants. After 24 hrs of HL exposure, *ilp1-1*, *ntr1-1*, and *prl1-2* continued to exhibit elevated anthocyanin levels compared to WT, regardless of PLP availability (Figure S24G), indicating that PLP deficiency is not the causative factor driving excessive anthocyanin biosynthesis in these mutants.

4 Discussion

4.1 The multifaceted role of ILP1

During acclimation response, ILP1 emerges as a critical regulatory node influencing multiple physiological processes. From anthocyanin biosynthesis to sugar metabolism and amino acid production, ILP1 appears to act as a key modulator in how plants manage energy allocation and stress responses. The identification of the *raa20* mutation (a SNP at chromosome 5, position 2767004), leading to intron retention in *ILP1* mRNA (Figure S1), is particularly striking because it provides genetic and functional evidence that ILP1's loss-of-function results in widespread physiological changes. The resemblance between *ILP1* intron retention mutant (*ilp1 SNP)* and complete knockouts (*ilp1-1* and *ilp1-2*) (Figure 3) suggests that splicing regulation plays a pivotal role in ILP1's functionality, adding another layer of post-transcriptional control to its regulatory mechanism. But what makes *ILP1* so intriguing is not just its molecular function but also the cascade of metabolic shifts that arise in its absence.

4.1.1 ILP1 is a gatekeeper of anthocyanin biosynthesis

One of the most visually noticeable phenotypes of *ILP1* mutants is the dramatic increase in anthocyanin accumulation, particularly under HL exposure (Figure 3F). Anthocyanins serve multiple ecological and physiological roles, acting as UV shields, antioxidants, and stress-responsive pigments (Agati et al., 2020; Araguirang and Richter, 2022). Temporal analysis of anthocyanin accumulation revealed a kinetic pattern where anthocyanin accumulation in *ilp1-1* remains comparable to WT in early timepoints. Then, it increased exponentially between 16 and 24 hours (Figure 4C). This suggests a delayed metabolic shift, wherein *ilp1* mutants initially cope with HL stress normally, but eventually, a secondary compensatory response such as anthocyanin biosynthesis is triggered.

The transcriptomic analysis validates this hypothesis, showing that *PAP1* and *DFR* are only significantly upregulated after 4 and 12 hours of HL exposure, respectively (Figure 4A, 4B). This time lag aligns with the idea that a metabolic checkpoint, possibly governed by sugar signaling and energy balance, is involved and this metabolic signal drives anthocyanin accumulation in *ilp1-1* mutants. This further infers that ILP1 normally suppresses anthocyanin biosynthesis until sugar levels reach a certain threshold. Hence, ILP1 is a metabolic gatekeeper, ensuring that anthocyanin biosynthesis is only induced when necessary.

4.1.2 ILP1 links carbon and nitrogen pools

ILP1's non-functionality reprograms sugar metabolism to favor long-term carbon storage while simultaneously increasing sugar export from plastids. Because ILP1 acts as a metabolic "brake", it prevents excessive sugar accumulation under normal conditions. The observed high cytosolic sugars and starch contents in *ilp1-1* (Figure 6) suggests that mutating *ILP1* alters carbon partitioning in response to HL, leading to excessive starch storage. In the absence of a functional ILP1, sugars build up, inadvertently triggering anthocyanin biosynthesis via sugar-related pathways. This connection between sugar levels and anthocyanin biosynthesis in *ilp1-1* mutants also suggests a broader trade-off between primary and specialized metabolism during HL acclimation response.

The DCMU treatment experiment also provides the most convincing piece of evidence supporting the sugar-driven anthocyanin accumulation model. DCMU is a photosynthesis inhibitor that blocks electron transport in photosystem II, effectively halting sugar production from CO_2 fixation. In the DCMU-treated plants, anthocyanin levels were repressed during HL exposure (Figure 7A). *PAP1*, *PAP2*, and *DFR* expressions declined in both WT and *ilp1-1*, reinforcing the sugar-dependent regulation of these genes (Figure 7B-7D). On the other hand, *MYBL2* was upregulated in both genotypes (Figure 7E), suggesting that sugar depletion reactivates MYBL2 to suppress flavonoid biosynthesis. These observations further cement the role of sugar as the primary driver of anthocyanin accumulation in *ilp1-1* mutants. during HL. This also suggests that anthocyanin production in *ilp1-1* is not a direct response to stress, but rather a metabolic adaptation to excess sugar

levels, serving as a carbon overflow mechanism during HL exposure. So when *ilp1-1* plants accumulate too much sugar during HL exposure, they divert some of it into anthocyanin production as a way to regulate cellular homeostasis.

The persistence of higher photosynthetic activity even after HL exposure (Figures S6, S7, S8) suggests that *ilp1-1* maintains efficient carbon fixation despite prolonged light stress, possibly through enhanced photoprotection and photosynthetic resilience, optimized energy dissipation, or modifications in carbon partitioning (Nico et al., 2019; Sharma et al., 2023). This also implicates that ILP1 regulates photosystem balance between light-harvesting efficiency and photoprotection, ensuring that energy capture is neither excessive (causing oxidative stress) nor insufficient (limiting carbon fixation). This further underscores a distinct physiological trait in *ilp1-1*, where elevated photosynthetic performance contributes to altered carbon metabolism, leading to higher carbohydrate accumulation during HL. The accumulation of high starch and cytosolic sugars in *ilp1-1* may also contribute to the suppression of specific photosynthetic genes and protein adjustments (Figure S6C, S7A, S7B), potentially as parts of a feedback regulatory mechanism to balance energy production and metabolic demand under HL acclimation. Overall, the differential regulation observed in *ilp1-1* suggests that ILP1 might coordinate nuclear-chloroplast communication, regulating energy allocation, repair cycles, and metabolic flux during HL conditions.

The prominent elevated levels of 3-PGA before HL and during the first 8 hrs of exposure aligns with previous findings (Figure 8) (Balcke et al., 2023) and may also be a reason for the observed high levels of sugars in *ilp1-1* during HL. It is also possible that this 3-PGA accumulation indicates a bottleneck in downstream carbon metabolism, likely due to impaired integration with nitrogen assimilation pathways.

Given that glutamate contributes 88% of cellular nitrogen and serves as a critical donor for amino acid biosynthesis (Reitzer, 2003), the temporal spike of glutamate between 4 and 12 hrs of HL suggests that ILP1 may facilitate a rapid nitrogen assimilation response during the early timepoints of HL. This also emphasizes glutamate's centrality in nitrogen assimilation and redistribution during HL acclimation response. The subsequent depletion of glutamate and the decline of metabolites in the urea cycle during HL also suggests an impaired capacity for

nitrogen recycling, which may compromise polyamine biosynthesis (Alcázar et al., 2006; Groppa and Benavides, 2008), nitric oxide signaling (Mur et al., 2013; Graska et al., 2023), and overall stress adaptation. This observation further supports the idea that ILP1 is crucial for sustaining nitrogen balance beyond the initial stress response. The shift in metabolic balance, particularly the observed high levels of starch and cytosolic sugars before and after HL exposure and the decrease in amino acid contents during HL, suggest a compensatory shift towards alternative carbon partitioning strategies. This further highlights the hypothesis that ILP1 also functions in modulating and coordinating carbon-to-nitrogen fluxes during acclimation response.

4.1.3 ILP1 is a negative regulator of sugar metabolism

The generation of overexpression (OE) and complementation lines of *ILP1* aimed to assess whether ILP1 level influences anthocyanin production or metabolic reprogramming under HL exposure. Interestingly, while OE and complementation lines restored WT-like growth phenotypes under normal conditions, they failed to suppress anthocyanin accumulation under HL, indicating that ILP1 overexpression does not override the transcriptional circuitry governing anthocyanin biosynthesis (Figure 9A). This also implies that anthocyanin production is tightly regulated by upstream signaling pathways independent of ILP1 protein levels.

Transcriptomic analyses revealed that key anthocyanin biosynthesis genes (*4CL3*, *DFR*, and *FLS1*) exhibited WT-like mRNA accumulation in OE lines (Figure 9B-9D), which likely explains their similarity to WT in terms of anthocyanin levels. The unchanged expression pattern of these genes provides a mechanistic explanation for why anthocyanin levels remained comparable to WT, despite *ILP1* overexpression. This suggests that ILP1 does not act as a direct repressor of anthocyanin biosynthesis genes but may instead function as a modulator of upstream regulatory networks influencing metabolic adaptation under HL conditions.

Notably, OE lines also displayed normal amino acid profiles (Figure S11), further underpinning the idea that ILP1 is a key regulator of metabolic homeostasis under

HL stress. However, the repression of cytosolic sugars in OE lines during HL exposure, which was also mirrored in the pronounced repression of *GPT2* expression (Figure S12B), suggests an inhibitory role of ILP1 in carbon metabolism, particularly cytosolic sugar production. These findings further support ILP1's role as a negative regulator of carbohydrate metabolism, potentially influencing sugar-dependent stress signaling pathways that integrate photosynthetic activity, energy availability, and secondary metabolite production during HL exposure.

4.2 ILP1 variants and their functional implications

The nuclear localization sequence (NLS) directs ILP1 to the nucleus while its GC-rich DNA-binding domain is essential for transcriptional repression (Yoshizumi et al., 2006). The dissection of ILP1's domain architecture provided critical insights into the functional domains required for its regulatory role while the transient expression assays revealed its nuclear localization and potential interactions in different subcellular compartments. The partial colocalization of ILP1 with ER and plasma membrane markers suggests that it might engage in membrane-associated processes aside from its nuclear role (Figure S13A, S13B). On the other hand, the presence of net-like structures in Z-stack projections, reminiscent of cytoskeletal-associated proteins (Cao, et al., 2016; Zang et al., 2021), raises intriguing possibilities that ILP1 might also modulate cellular architecture in addition to its transcriptional function (Figure S13C).

Truncation analyses further delineated the functional contributions of ILP1's distinct domains, revealing that nuclear localization is a key determinant of ILP1 function. Notably, the absence of the N-terminal domain did not impair ILP1's ability to restore WT-like growth and metabolic phenotypes in *ilp1-1* mutants, as long as the protein retained its nuclear localization (Figure 10). This finding indicates that the N-terminal part of ILP1 is not the main domain regulating proper growth and metabolic homeostasis in both normal and HL conditions.

In contrast, the GC-rich DNA-binding domain alone, without the nuclear localization signal (NLS), failed to restore WT-like phenotypes in *ilp1-1*, suggesting

that proper nuclear targeting is crucial for ILP1 function (Figure 10). These results emphasize that while the GC-rich domain is important for ILP1 activity, its effectiveness is highly dependent on nuclear localization, reinforcing the notion that ILP1 primarily exerts its regulatory functions within the nucleus.

Truncated ILP1 variants lacking the GC-rich DNA-binding domain but still capable of nuclear localization failed to restore WT-like acclimation phenotypes, instead retaining the *ilp1-1*-like anthocyanin overaccumulation and metabolic imbalance. This reinforces the critical role of ILP1's C-terminal domain in regulating metabolic homeostasis and anthocyanin biosynthesis during HL acclimation. The requirement for the GC-rich DNA binding domain in anthocyanin repression and metabolic homeostasis further suggests that this region mediates additional regulatory interactions beyond transcriptional repression, such as modulation of metabolic rewiring and stress acclimation under HL conditions. Taken together, these insights collectively provide strong evidence that ILP1 functions as a metabolic switch, through its GC-rich DNA binding domain, ensuring a balanced allocation of carbon and nitrogen resources during HL acclimation. Future studies focusing on a nuclear-localized ILP1 variant (with only GC-rich DNA binding domain) will help uncover the precise molecular mechanisms underlying ILP1's role in stress adaptation and metabolic homeostasis.

4.3 ILP1 and its prion-like domain

Prion-like domains (PrDs) in plants have been implicated in various biological processes such as thermosensing (Jung et al., 2020), seed germination and water sensing (Dorone et al., 2021), and cold acclimation (Legen et al., 2024), demonstrating their diverse roles in environmental adaptation and developmental pathways. A defining characteristic of PrDs is their ability to undergo liquid-liquid phase separation (LLPS), a property crucial for dynamic cellular organization and biomolecular condensate formation (Banani et al., 2017). The deletion of PrDs has been shown to prevent phase separation, resulting in loss-of-function phenotypes (Dorone et al., 2021).

Bioinformatic analysis identified a PrD near the N-terminal domain of ILP1 (Figure S17B, S17C), suggesting possible undiscovered regulatory functions during HL acclimation. However, mutating the two glutamine (Q) residues ($Q^{318,319}A$) within the ILP1 PrD and transforming the mutant construct into the *ilp1-1* background resulted in WT-like morphology, splicing, and sugar production under normal conditions and during HL acclimation (Figure S18). These findings indicate that, at least under HL conditions, the PrD of ILP1 is not essential for HL acclimation, splicing fidelity, nor carbohydrate metabolism, as starch and cytosolic sugar levels in $Q^{318,319}A$ mutants remained similar with WT before and after HL exposure (Figure S18E, S18F).

Surprisingly, despite exhibiting a WT-like phenotype during HL acclimation, the $Q^{318,319}A$ mutants displayed an amino acid profile that closely resembled the *ilp1-1* mutant rather than WT under normal conditions (Figure S18K). This finding suggests that the ILP1 PrD plays a specific role in amino acid metabolism under non-stress conditions, expanding the functional repertoire of PrDs beyond stress adaptation and biomolecular condensate formation. Given that the ILP1 PrD is embedded within an intrinsically disordered region (Figure S17B), which provides structural flexibility, it is likely that this domain functions as a molecular scaffold, facilitating interactions with key metabolic enzymes or RNA-binding proteins involved in amino acid biosynthesis.

4.4 ILP1 independence from miRNA pathways

Previous studies across multiple plant species, including Arabidopsis (Gou et al., 2011), sweet potato (He et al., 2019), poplar (Wang et al., 2020), potato tubers (Wu et al., 2022), and kiwifruit (Li et al., 2020), have established a strong link between miRNA regulation and anthocyanin biosynthesis. Given this broad regulatory role of miRNAs in anthocyanin biosynthesis, the involvement of ILP1 in miRNA biogenesis could also possibly influence HL acclimation through miRNA-mediated pathways. However, experimental findings using the *SERRATE1* mutant (*se1*) and *ilp1-1* strongly contradict this assumption (Figure S19). Under normal conditions, *se1* resembled WT-like developmental phenotypes such as root and hypocotyl lengths (Figure S19A, S19B). The stark contrast between the WT-like anthocyanin

accumulation and transcript levels of biosynthetic genes in *se1* and the overaccumulation of anthocyanins in *ilp1-1* compared to the WT (Figure S19C-S19F) indicate that ILP1-mediated HL acclimation is largely independent of miRNA biogenesis, despite ILP1 being implicated in miRNA processing (Wang et al., 2019).

While the results suggest that ILP1-driven HL acclimation is not miRNA-dependent (or it only plays a minor role), there may still be indirect regulatory interactions between ILP1 regulation and miRNA networks. For instance, ILP1-mediated regulation may influence transcripts encoding miRNA-processing factors, such as *DICER-LIKE1* (*DCL1*) (Kurihara and Watanabe, 2004; Kim et al., 2009; Wei et al., 2021) or *ARGONAUTE* (*AGO*) (Zhang et al., 2014b; Liu et al., 2018) proteins, thereby affecting miRNA activity under certain conditions. To fully understand this regulatory network, future research should explore whether ILP1 affects miRNAs directly during HL exposure or engages with transcription factors regulated by miRNAs in response to stress conditions.

4.5 *ilp1-1* and its splicing defects

A comprehensive analysis of alternative splicing (AS) events in *ilp1-1* during HL exposure identified intron retention (RI) as the most prevalent splicing anomaly, persisting from normal conditions through HL exposure and the subsequent recovery phase (Figure S20). Additional splicing defects, including exon skipping (SE) and alternative 3' and 5' splice site selection (A3S and A5S), further demonstrate ILP1's role in regulating precise splicing events across multiple biological pathways. Before HL exposure (Figure S20C), the accumulation of transcripts with intron retention enriched in RNA splicing, spliceosome-mediated mRNA processing, and metabolic pathways suggests that ILP1 serves as a core regulator of RNA processing fidelity and metabolic transcript stability under normal growth conditions. The shift in functional enrichment patterns under HL exposure to intron-containing transcripts predominantly enriched in primary metabolism, mRNA stability, and metabolic adaptation-related processes (Figure S20D) indicates that ILP1 is essential for maintaining transcriptome integrity

during HL exposure. This reinforces ILP1's role as a critical regulator of alternative splicing, particularly in metabolic homeostasis and HL acclimation. Although no correlation was found between gene expression levels and splicing fidelity in *ilp1-1* (Araguirang et al., 2024), ILP1 deficiency still leads to widespread splicing defects of key metabolic and stress-responsive transcripts, thereby affecting growth and stress acclimation response. These insights further establish ILP1 as a central molecular integrator, bridging transcriptional and post-transcriptional regulation and metabolic adaptation, with broader implications for plant development and environmental responses.

4.6 Spliceosomal components as acclimation markers

The parallel developmental, metabolic, and transcriptional responses observed in *ilp1-1* and *ntr1-1* mutants (Figure 11) support the idea that ILP1 and NTR1, which are both components of the spliceosomal ILS (Wang et al., 2019), operate within a shared regulatory pathway that governs growth, metabolic equilibrium, and stress responses under HL conditions. The embryonic lethality of *ilp1-1 ntr1-1* double homozygous mutants posed a challenge for genetic analysis. To circumvent this limitation, Virus-Induced Gene Silencing (VIGS) was employed as an alternative functional genomics approach (Burch-Smith et al., 2006; Liu et al., 2002). This strategy allowed for transient knockdown of *ILP1* in the *ntr1-1* background, enabling the investigation of their combined functional effects without the constraints of lethality. The persistent metabolic imbalance in the VIGS mutants of *ilp1-1 ntr1-1* highlights the critical role of ILP1 and NTR1 in maintaining homeostasis under both normal and HL conditions. The involvement of ILP1 and NTR1 in diverse biological processes, including precise RNA splicing (Dolata et al., 2015), miRNA biogenesis (Wang et al., 2019), and C:N flux in HL acclimation (Araguirang et al., 2024), suggests that these genes function not as independent regulators, but rather as integral components of a spliceosome-dependent regulatory network. This network likely serves as a key integration point for developmental and environmental signals, coordinating gene expression and metabolic responses to ensure cellular homeostasis and adaptive plasticity under changing conditions. Future investigations focusing on the molecular mechanisms

underlying ILP1 and NTR1 co-regulation will provide deeper insights into how plants modulate gene expression and metabolism in response to HL conditions.

The inclusion of *prl1-2* (Figure 12), a mutant of *PRL1* which is another component of the spliceosome, strengthens the role of the spliceosomal complex in the regulation of anthocyanin biosynthesis and C:N homeostasis during HL acclimation. The metabolic shifts observed in *prl1-2*, *ilp1-1,* and *ntr1-1* indicate that these spliceosomal complex components collectively regulate C:N fluxes, suggesting that the spliceosomal complex acts as a central regulatory hub, integrating light stress responses, metabolic pathways, and gene expression regulation during HL exposure.

Additionally, the presence of contrasting mutations at the same critical catalytic site of PRP8 (Figure S22C) suggests that spliceosome-mediated HL acclimation may be influenced by charge-dependent structural modifications in this core splicing factor. The divergence in anthocyanin accumulation, biosynthetic gene expressions, and metabolic profiles between *prp8-7* and *prp8-12* (Figure 13) indicate that structural alterations in PRP8 may also affect spliceosome efficiency or specificity in processing stress-responsive transcripts and coordinating metabolic equilibrium during HL acclimation. Further investigation into how these mutations differentially impact RNA processing and metabolic adaptation will provide deeper insights into the functional diversity of spliceosomal components in plant stress responses.

The identification of ILP1, NTR1, PRL1, and PRP8 as key regulatory factors influencing anthocyanin accumulation in response to HL exposure underscores the crucial role of spliceosomal components in orchestrating transcriptomic and metabolomic reprogramming during HL acclimation. These results highlight how the spliceosomal machinery emerges as a fundamental component in the plant's adaptive responses to HL conditions. More importantly, the spliceosome mutants represent valuable genetic markers for studying HL acclimation, providing powerful tools for future research aimed at unraveling the interplay between RNA processing, metabolic regulation, and acclimation response.

4.7 Impaired nitrogen metabolism of spliceosome mutants

The inability of *ilp1-1* and *ntr1-1* seedlings to respond to nitrogen supplementation suggests that these spliceosomal components may regulate the expression or processing of transcripts essential for root elongation and nutrient assimilation (Figure 15). It also implies that spliceosomal components possibly regulate distinct aspects of nitrogen metabolism. However, the persistence of anthocyanin overaccumulation despite nitrogen supplementation suggests that regulatory defects in anthocyanin biosynthesis pathways, rather than nutrient limitations, are responsible for the observed phenotype (Figure 15D).

The failure of exogenous PLP to complement the short-root and hypocotyl phenotypes in *ilp1-1*, *ntr1-1*, and *prl1-2* suggests that (1) *ilp1-1*, *ntr1-1*, and *prl1-2* are not PLP-deficient and thus, external PLP supplementation did not restore normal growth and anthocyanin accumulation and (2) there is an excessive PLP accumulation that leads to negative feedback inhibition, suppressing root and hypocotyl elongation by altering the regulation of PLP-dependent pathways involved in growth and metabolism.

The consistent anthocyanin overaccumulation in the spliceosomal mutants, even after exogenous PLP supplementation (Figure S24G), indicates that ILP1, NTR1, and PRL1 regulate anthocyanin metabolism through mechanisms independent of PLP-dependent enzymatic pathways. This further suggests that anthocyanin accumulation in *ilp1-1*, *ntr1-1*, and *prl1-2* is not a direct consequence of PLP limitation, but rather a compensatory response to metabolic or transcriptional deregulation. These findings further imply that PLP metabolism and anthocyanin biosynthesis function within distinct regulatory networks, with ILP1, NTR1, and PRL1 acting as upstream modulators of gene expression and metabolic reprogramming rather than direct cofactors in PLP-dependent enzymatic reactions.

5 Conclusions & Outlook

For decades, there has been a long-standing debate on which among the proposed factors (hormones, ROS, sugars) trigger anthocyanin biosynthesis. The recently published study on how sugars exported out of the chloroplast inactivate the SnRK1 complex to induce anthocyanin accumulation provided direct pieces of evidence that sugars are the key molecules of anthocyanin production, particularly during HL acclimation (Zirngibl et al., 2022). Results from this research further support this notion and also present a new understanding on how spliceosomal complex components like ILP1, NTR1, PRL1, and PRP8, or to an extent the whole spliceosome, maintain normal carbon and nitrogen fluxes during HL acclimation response.

Mapping of the starch and sugar metabolism based on the analyzed RNA-seq data provided a stronger support on ILP1 as a regulator of carbon metabolism. Mutation in *ILP1* showed disruption of expression profiles of genes involved in starch and sugar synthesis. The *ilp1-1* mutant also exhibited elevated levels of starch and cytosolic sugars during HL exposure. *ILP1* overexpression and genetic complementation lines displayed repression of neutral sugars, adding a new layer of knowledge that ILP1 is not only a repressor of cell cycle genes (Yoshizumi et al., 2006), but also a possible regulator of carbon metabolism in vivo.

Truncation and point mutation analyses of ILP1 have provided significant insights into the structural and functional requirements of this spliceosomal component. These analyses revealed that the nuclear-localized GC-rich DNA binding domain is indispensable for ILP1 function, particularly in maintaining splicing fidelity and metabolic homeostasis under HL stress. Variants lacking this domain exhibited splicing defects, deregulation of anthocyanin biosynthetic transcripts, and metabolic imbalances, resembling *ilp1-1* mutants. These findings establish this domain as a key regulatory element, enabling ILP1 to integrate spliceosomal activity, transcriptional regulation, and metabolic equilibrium to ensure an effective acclimation response under HL conditions.

Comprehensive metabolic profiling of *ilp1-1*, *ntr1-1*, *prl1-1*, and *prp8* mutants revealed a significant reduction in most amino acids, including phenylalanine and glutamine, during HL exposure, compared to WT. In contrast, other amino acids like glutamate exhibited a marked accumulation after 8 hrs of HL. The increase in carbon metabolism-related products and the subsequent decline in amino acid contents suggests a tight link between C:N homeostasis and HL acclimation.

ILP1, NTR1, PRL1, and PRP8 are proposed to play a regulatory role in directing carbon skeleton influx from nitrogen metabolism during HL acclimation. To validate this hypothesis, stable isotope labeling experiments using C-labeled tracers should be conducted to track carbon flux dynamics under HL conditions. Such an approach would provide quantitative insights into metabolic reconfiguration and confirm whether these spliceosomal components actively influence carbon partitioning and metabolic homeostasis during HL acclimation. It is also highly possible that the observed abnormalities in the carbon and nitrogen metabolism during HL are two independent pleiotropic effects of spliceosomal mutants. Thus, the interplay among spliceosome-mediated gene regulation, C:N fluxes, and specialized metabolism warrants further investigation to uncover how these spliceosomal components integrate metabolic and stress-responsive pathways during HL acclimation.

Overall, this research proposes the use of mutants of ILP1, NTR1, PRL1 and PRP8 as acclimation markers because of their indispensable roles in modulating transcriptomic and metabolomic reprogramming during HL acclimation. These factors are crucial for the regulation of gene expression and metabolic profiles, ensuring a balanced distribution of metabolites when plants are exposed to HL stress.

By elucidating the interaction among spliceosomal functions, gene regulation, and metabolic adaptation, the findings presented herein also offer valuable and unprecedented insights into the fundamental mechanisms underlying plant environmental responses and resilience. The time-resolved transcriptomic and metabolomic datasets generated in this dissertation serve as valuable resources for understanding HL acclimation dynamics, providing a comprehensive view of how plants reprogram gene expression and metabolism in response to HL stress. More

importantly, this study further opens new avenues for research, particularly on (1) the importance of the spliceosomal complex during HL acclimation, (2) how the ratio of C:N affects plant acclimation plasticity, and (3) potential novel functions of ILP1, NTR1, PRL1, and PRP8 as metabolic regulators, possibly uncovering their involvement in emerging biochemical phenomena such as liquid-liquid phase separation (LLPS) and other stress-adaptive mechanisms.

Appendix A: Supplementary Information

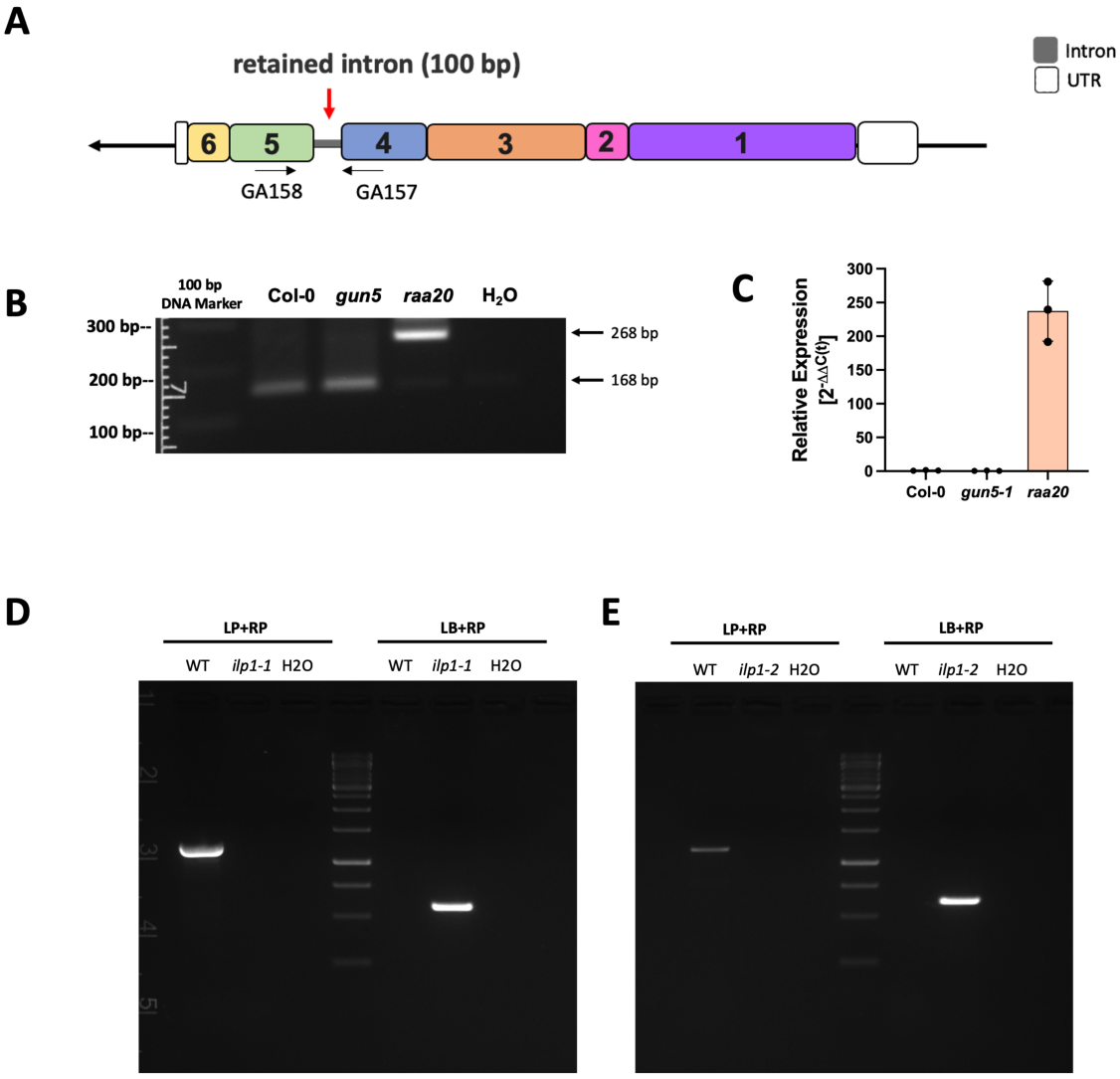

Figure S1. Validation of the SNP/intron retention and T-DNA insertions in the *ilp1* mutants. (A) Schematic diagram of the position of the intron retention in *ilp1 SNP*, (B) band size difference when retained intron was amplified, (C) relative expression of the retained intron in different plants, and genotyping of *ilp1-1* (D) and *ilp1-2* (E) knockout mutants. Data are mean ± SD (n = 3).

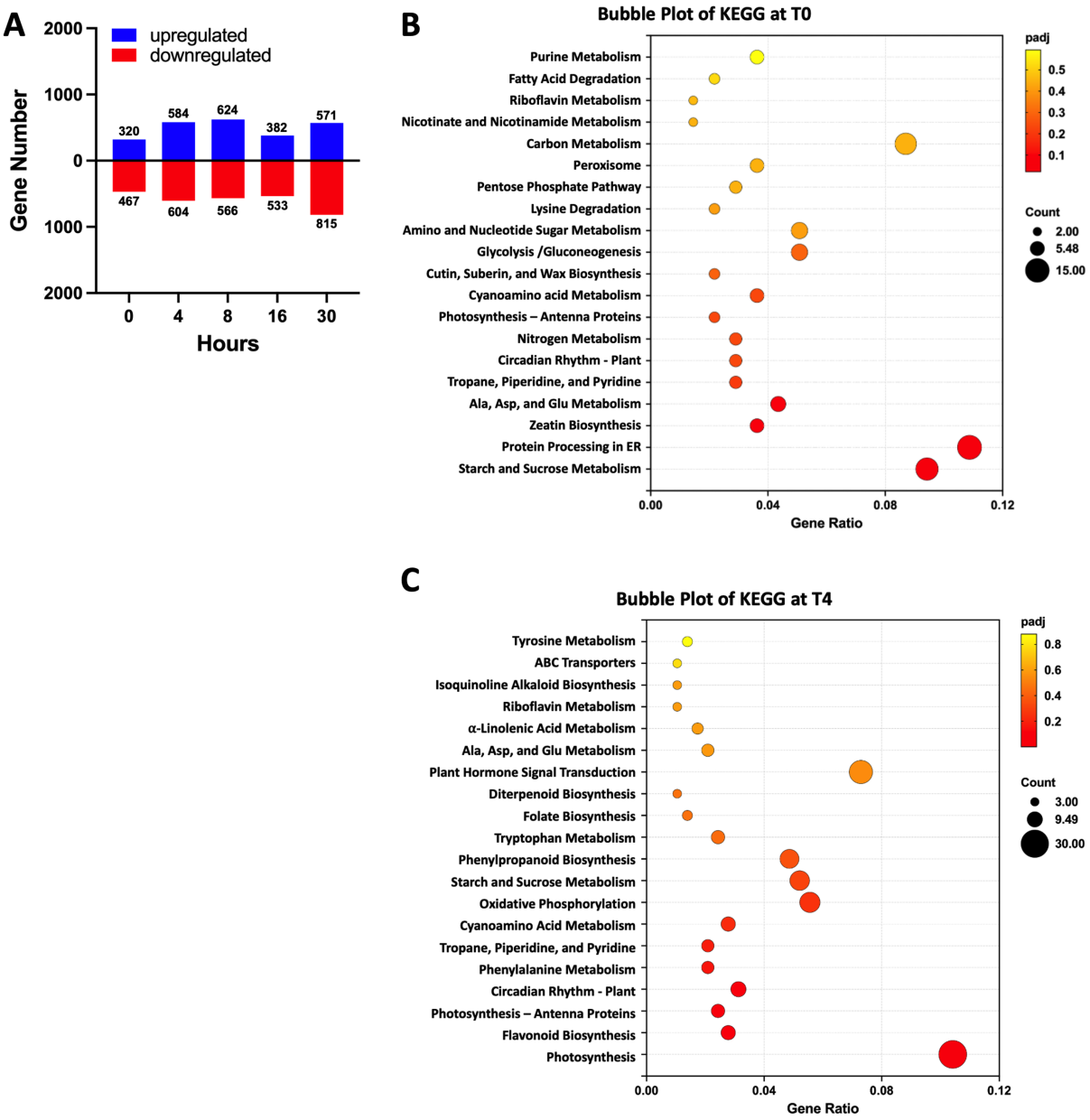

Figure S2. Transcriptome analysis of DEGs during high light exposure**.** (A) Total number of genes that are differentially upregulated and downregulated, and KEGG pathway analysis of differentially expressed genes (DEGs) at T0 (B) and T4 (C). Bubble plots showing the significant pathways for up- and downregulated DEGs. Larger bubbles indicate higher number of genes. The color of each bubble reflects significance (*p*-value).

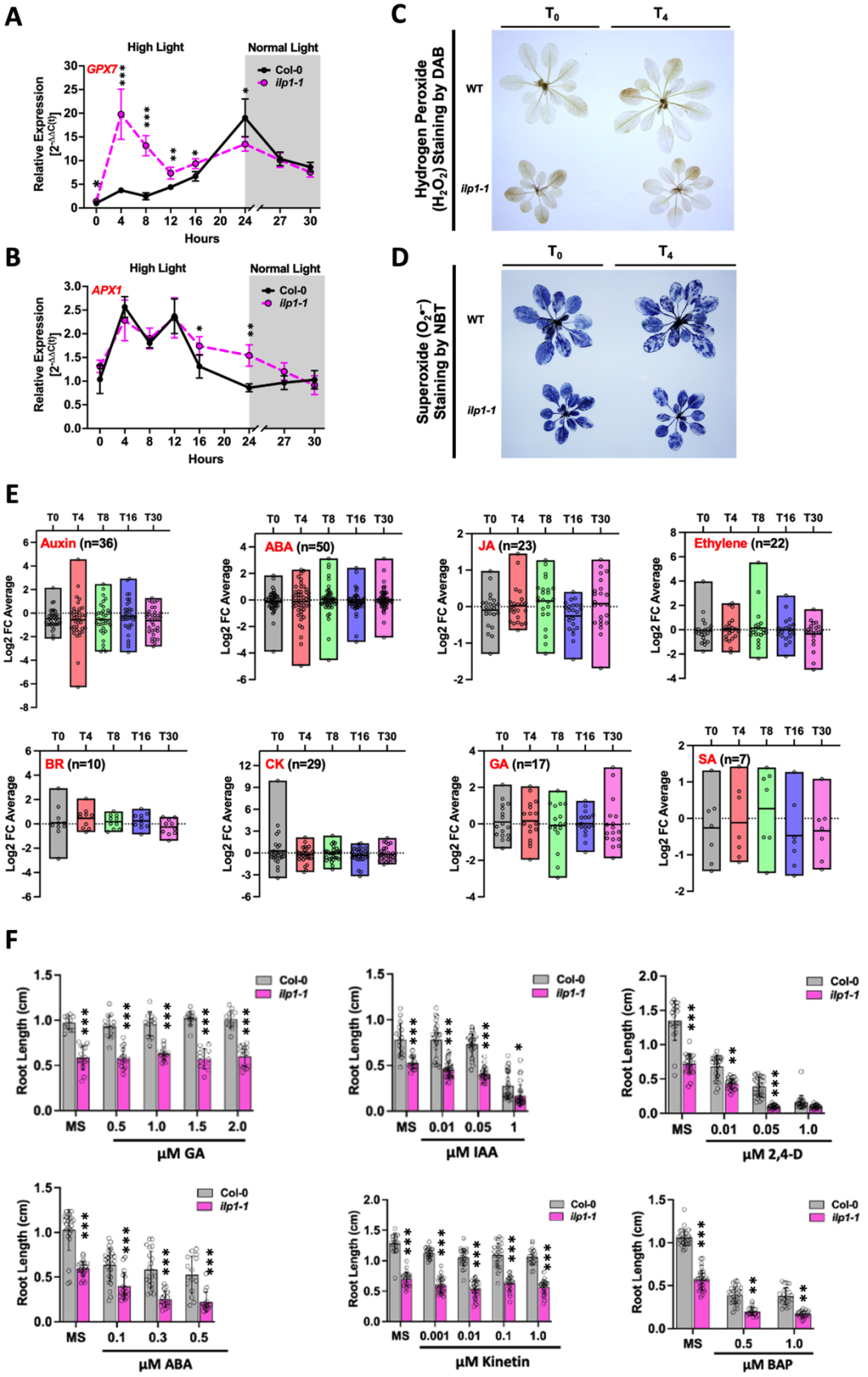

Figure S3. Analysis of other known factors affecting anthocyanin production in Col-0 and *ilp1-1*. Time-course analysis of (A) *GPX7* and (B) *APX1* relative expressions, (C) DAB

staining and (D) NBT staining before and after 4 hrs of HL, (E) Log2 FC average of all the genes involved in each hormone biosynthesis, and (F) root length complementation assays of 6-DAG seedlings using different concentrations of exogenous hormones. For A-B, data are mean ± SD (n = 4). Asterisks indicate statistical significance compared to Col-0 by Student's t-test (*P <0.05, **P <0.01, ***P <0.001). GA, gibberellic acid; IAA, indole-3-acetic acid; 2,4-D, 2,4-dichlorophenoxyacetic acid; ABA, abscisic acid; and BAP, 6-benzylaminopurine.

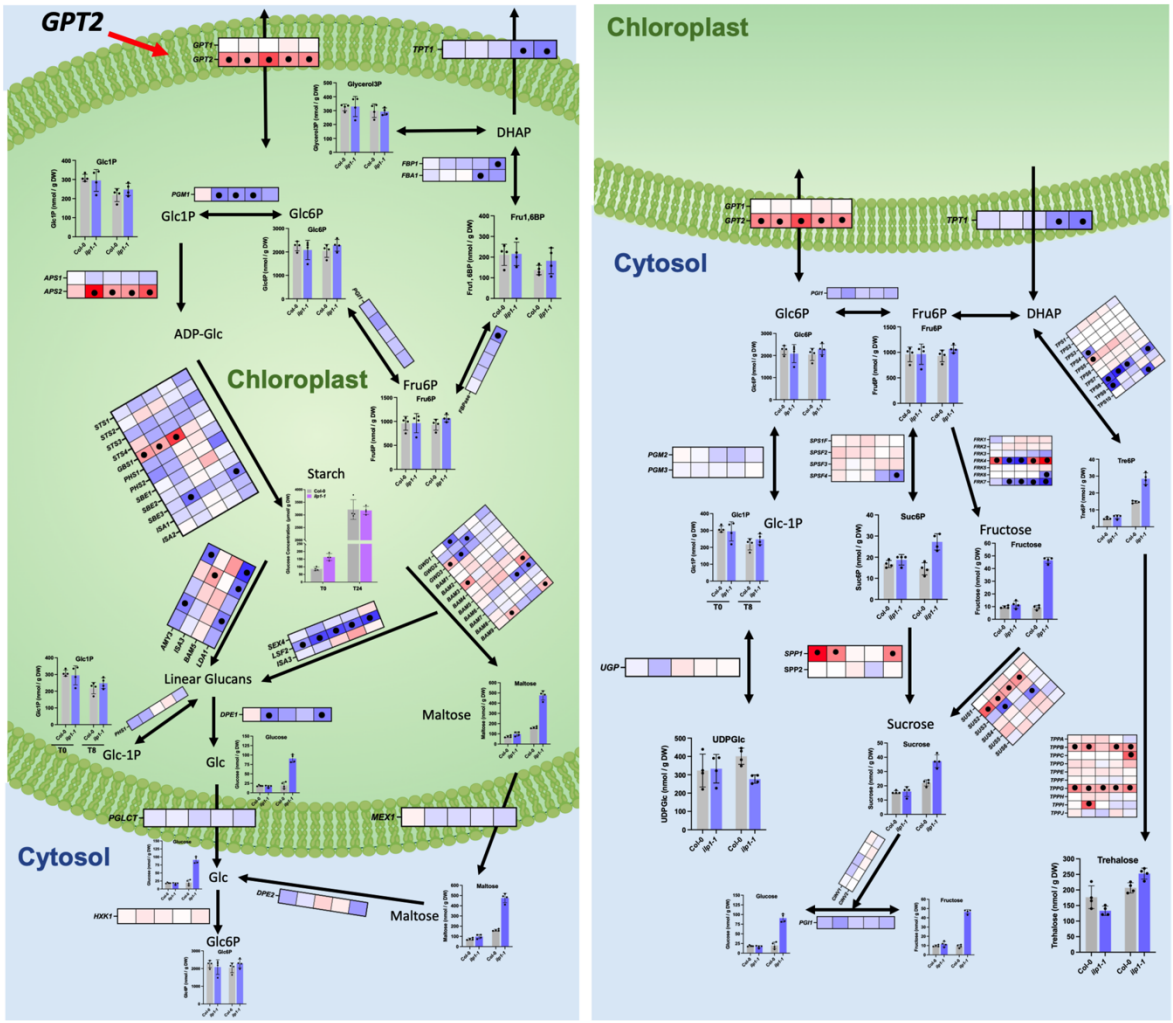

Figure S4. Transcriptomic landscape of starch and sugar metabolism in *ilp1-1* during HL exposure. "•" in the heatmap indicates significance.

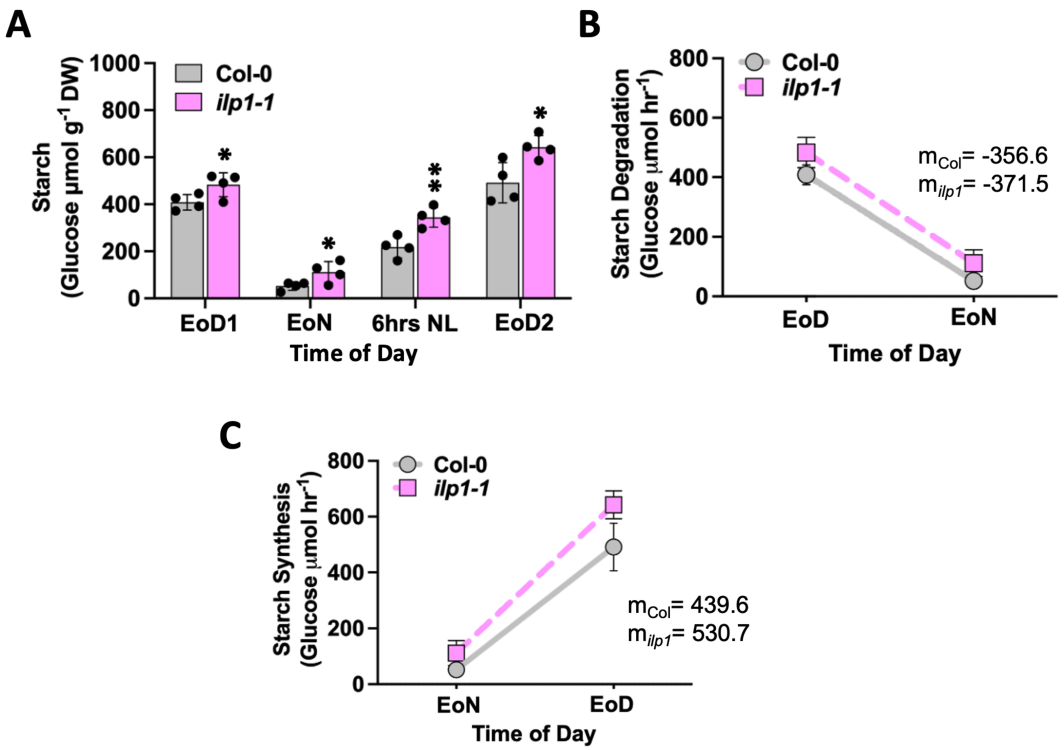

Figure S5. Starch analysis in *ilp1-1* and Col-0 plants during a normal day/night cycle. (A) Starch contents in 4-week-old plants from End of Day1 (EoD1) to End of Day2 (EoD2). (B) Starch degradation and (C) starch synthesis rates in *ilp1-1* under a normal day/night cycle. Data are mean ± SD (n = 4). Asterisks indicate statistical significance compared to Col-0 by Student's t-test (*P <0.05, **P <0.01, ***P <0.001).

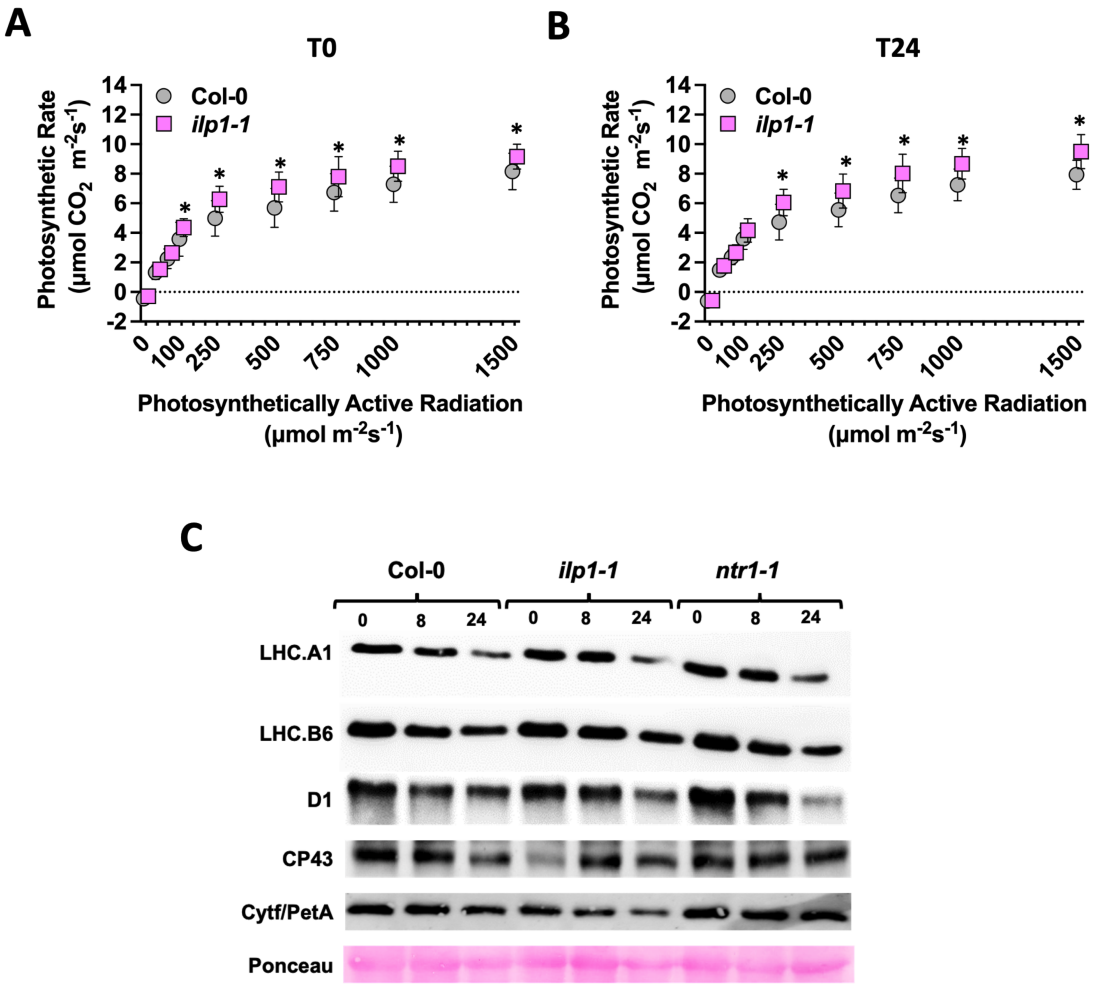

Figure S6. *ilp1-1* mutants have higher photosynthetic rates. (A) Net photosynthetic CO_2 uptake rates of 7-week-old Col-0 and *ilp1-1* ($n \geq 12$) in response to increasing light intensities (0, 25, 50, 100, 250, 500, 750, 1000, and 1500 µmol photons $m^{-2} sec^{-1}$) before (T0) and (B) after (24 hrs) HL exposure. Data are mean ± SD. Asterisks indicate statistical significance compared to WT by Student's t-test (*$P < 0.05$). (C) Steady-state levels of photosynthetic proteins in Col-0, *ilp1-1*, and *ntr1-1* before and during HL (8 and 24 hrs).

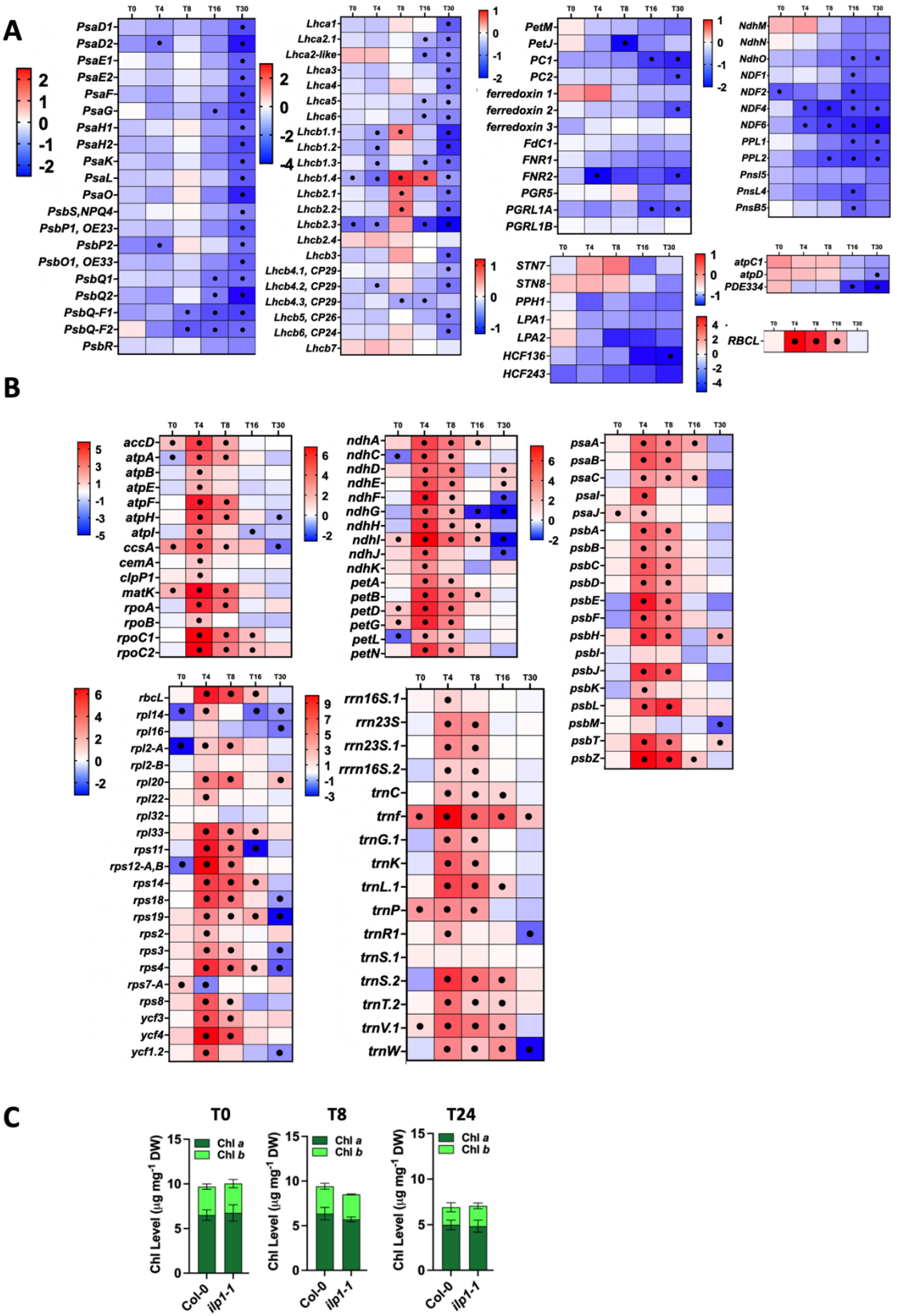

Figure S7. Expression analysis (Log2 FC) of (A) nuclear-encoded genes and (B) chloroplast-encoded genes of known photosynthetic proteins. (C) Total chlorophyll contents of 4-week-old Col-0 and *ilp1-1* at T0, T8, and T24. Data are mean ± SD (n = 4). "•" in the heatmap indicates significance.

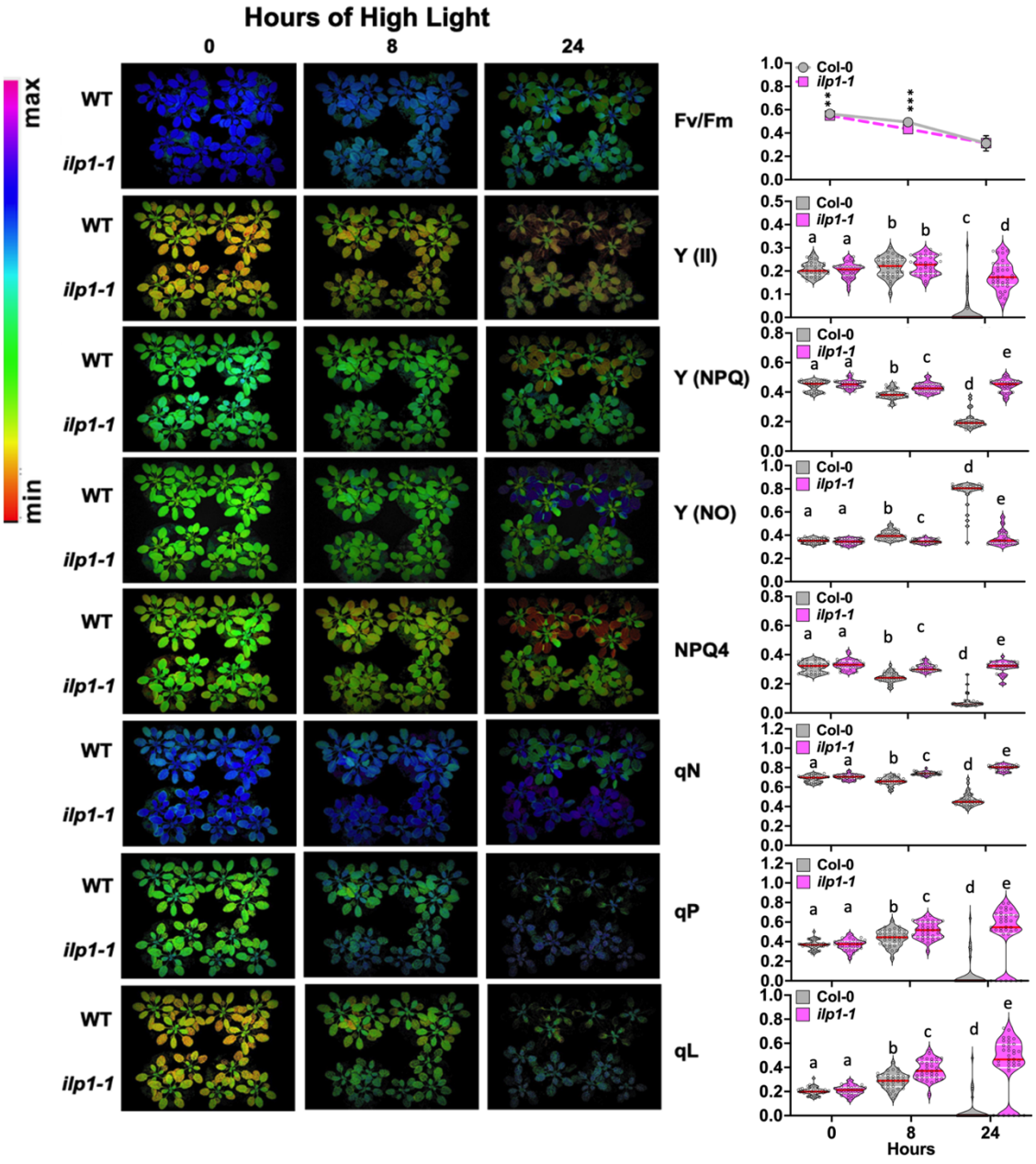

Figure S8. Measurements of different photosynthetic parameters in *ilp1-1* during HL. Fv/Fm, coefficients of photochemical quenching (qP), non-photochemical quenching (NPQ, qN), non-regulated energy dissipation Y (NO), and PSII quantum yield (Y(II)) of Col-0 and *ilp1-1* at T0, T8, and T24 of high light using an Imaging-PAM system (Walz) and are displayed on a rainbow colour scale. Right panel: Quantitative analyses from six plants per genotype and six leaves (n = 36) were analysed at 286 µmol photons $m^{-2} sec^{-1}$. Data are mean ± SD. Asterisks indicate statistical significance compared to Col-0 by Student's t-test (*P < 0.05). The red lines inside the violins show the median of values and the white lines the quartiles. Different letters indicate significance groups at P < 0.05 by Šidák's and Tukey's multiple comparison tests, respectively, as determined by two-way ANOVA.

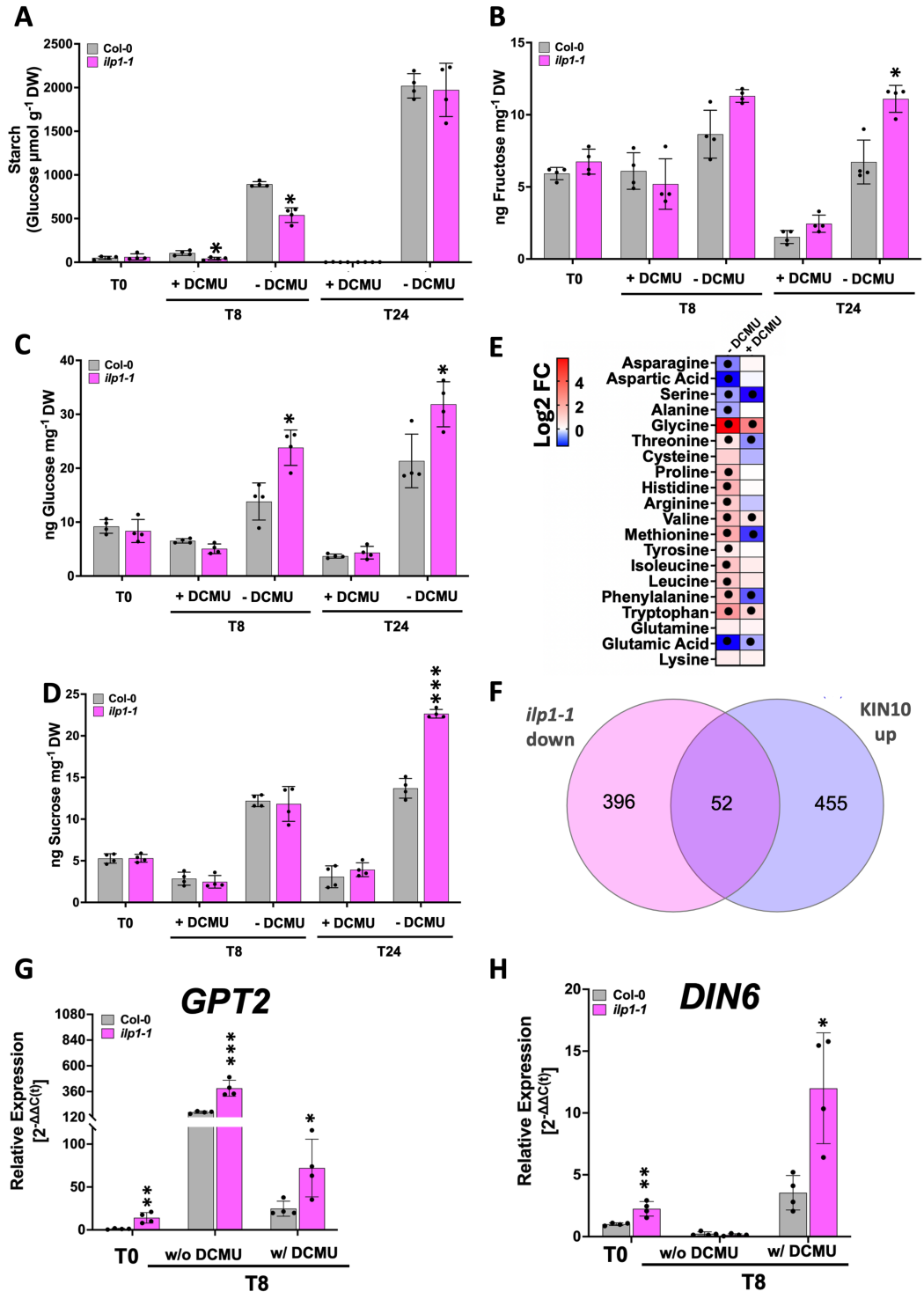

Figure S9. Metabolic changes in the *ilp1-1* mutant after DCMU treatment during HL. Contents of (A) starch, (B) fructose, (C) glucose, and (D) sucrose, (E) log2 FC of the quantified amino acids before and after treatment of DCMU, (F) venn diagram analysis showing the shared genes between differentially downregulated genes in *ilp1*-1 and differentially upregulated by KIN10, and relative expressions of (G) *GPT2* and (H) *DIN6* before and after 8 hrs of HL exposure. Data are mean ± SD. The venn diagram was constructed using https://www.interactivenn.net/ (Heberle et al., 2015). "•" in the heatmap indicates significance. Asterisks indicate statistical significance compared to Col-0 by Student's t-test (*P < 0.05; **P< 0.01, ***P < 0.001).

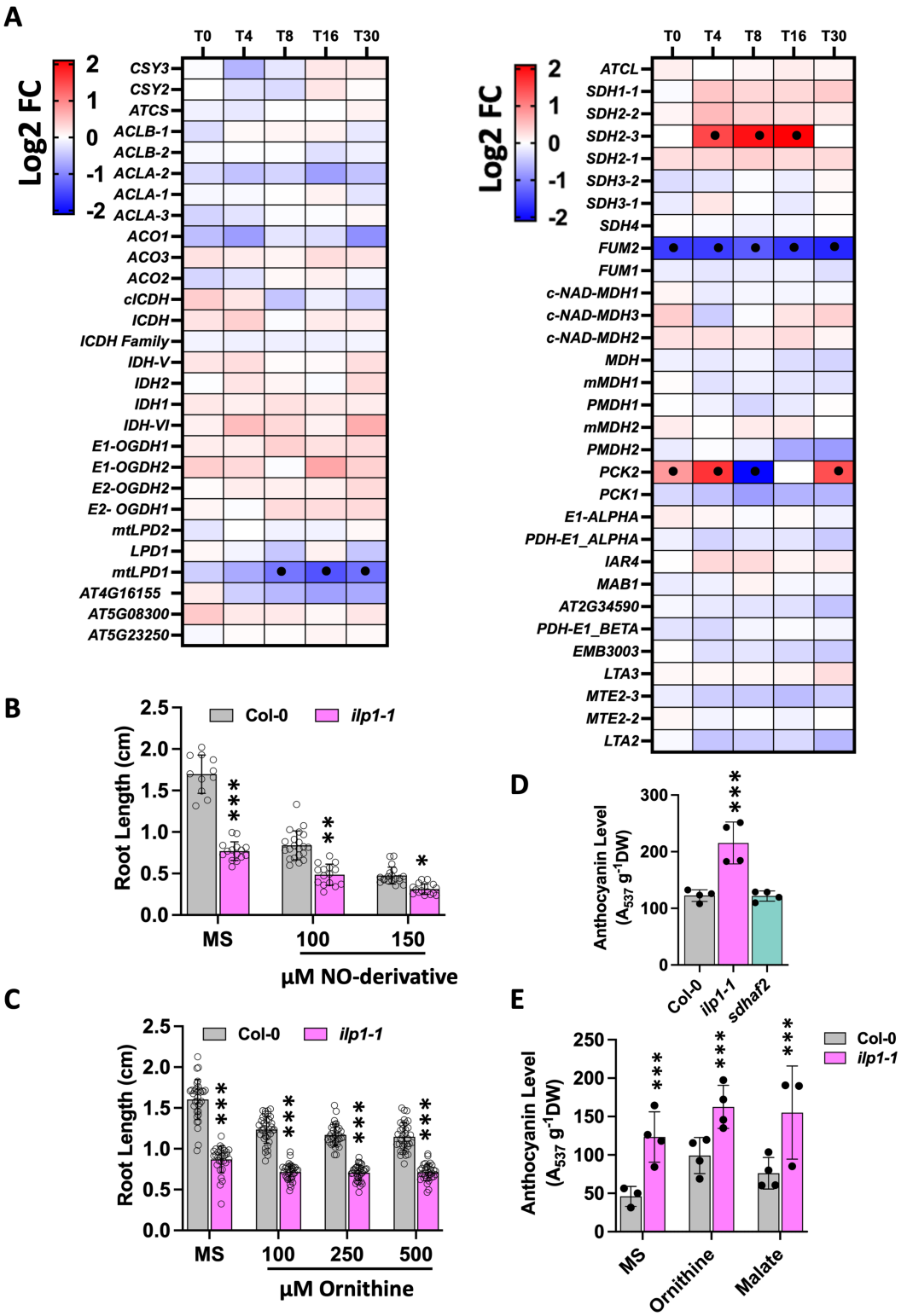

Figure S10. Disruption of TCA cycle-related profiles. (A) Expression profiles of genes involved in the TCA cycle, root lengths after exogenous supplementation with increasing concentrations of (B) sodium nitroprusside (a Nitric Oxide-derivative) and (C) ornithine, (D) anthocyanin levels in the *sdhaf2* mutant compared to WT and *ilp1-1*, and (D) anthocyanin levels in *ilp1-1* and WT seedlings after exogenous supplementation with 100 µM ornithine and malate. Data are mean ± SD. Asterisks indicate statistical significance compared to Col-0 by Student's t-test (*P < 0.05; **P< 0.01, ***P < 0.001). "•" in the heatmap indicates significance.

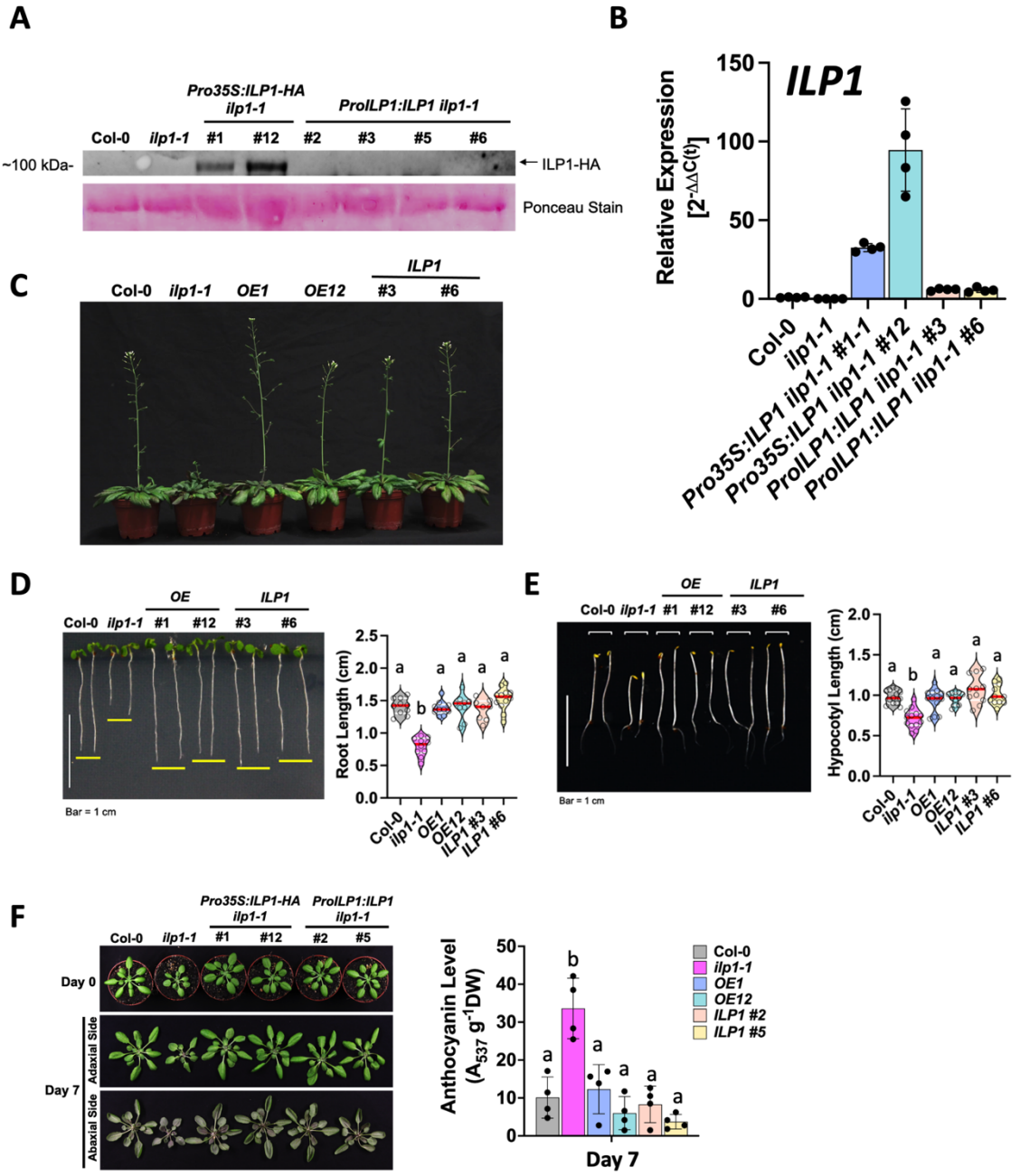

Figure S11. Generation, validation, and phenotypic characterization of the overexpression (OE) and genetic complementation lines of *ilp1-1*. (A) Western blot to check the presence of ILP1-HA in 4-week-old Col-0, *ilp1-1*, and OE lines and genetic complementation lines, (B) relative expression of *ILP1* in all lines, (C) flowering time after 11 weeks in short day conditions, (D) root lengths of 7DAG seedlings, (E) hypocotyl lengths of 4DAG dark-grown seedlings, and (F) anthocyanin phenotype after 7 days in the cold. Data are mean ± SD. Different letters indicate significance groups at $P < 0.05$ by Tukey's multiple comparison test as determined by one-way ANOVA. The red lines inside the violins show the median of values and the white lines the quartiles.

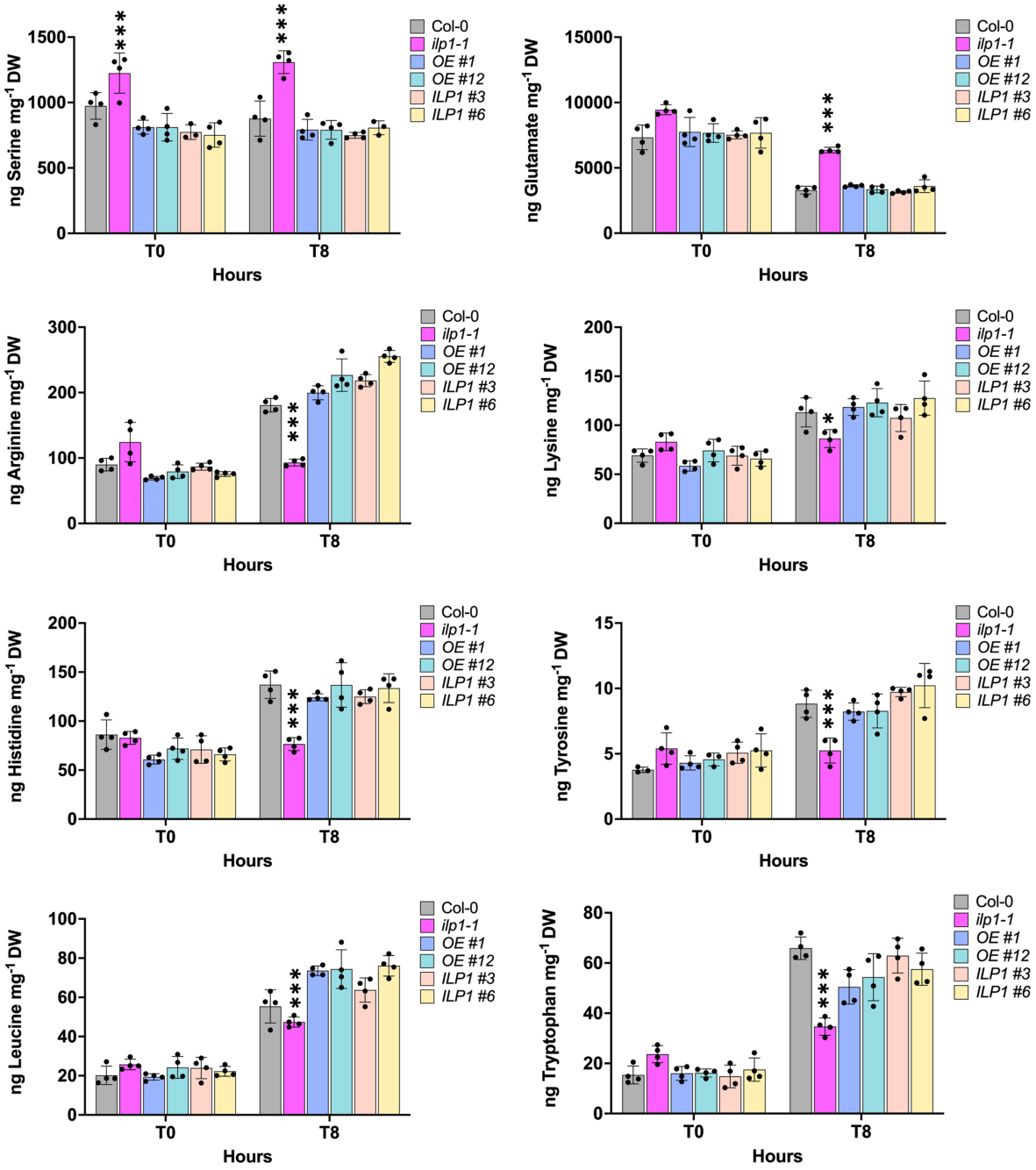

Figure S12. Representative metabolites showing WT-like levels in the OE and genetic complementation lines compared to *ilp1-1*. Data are mean ± SD. Asterisks indicate statistical significance compared to Col-0 by Student's t-test (*P < 0.05; ***P < 0.001).

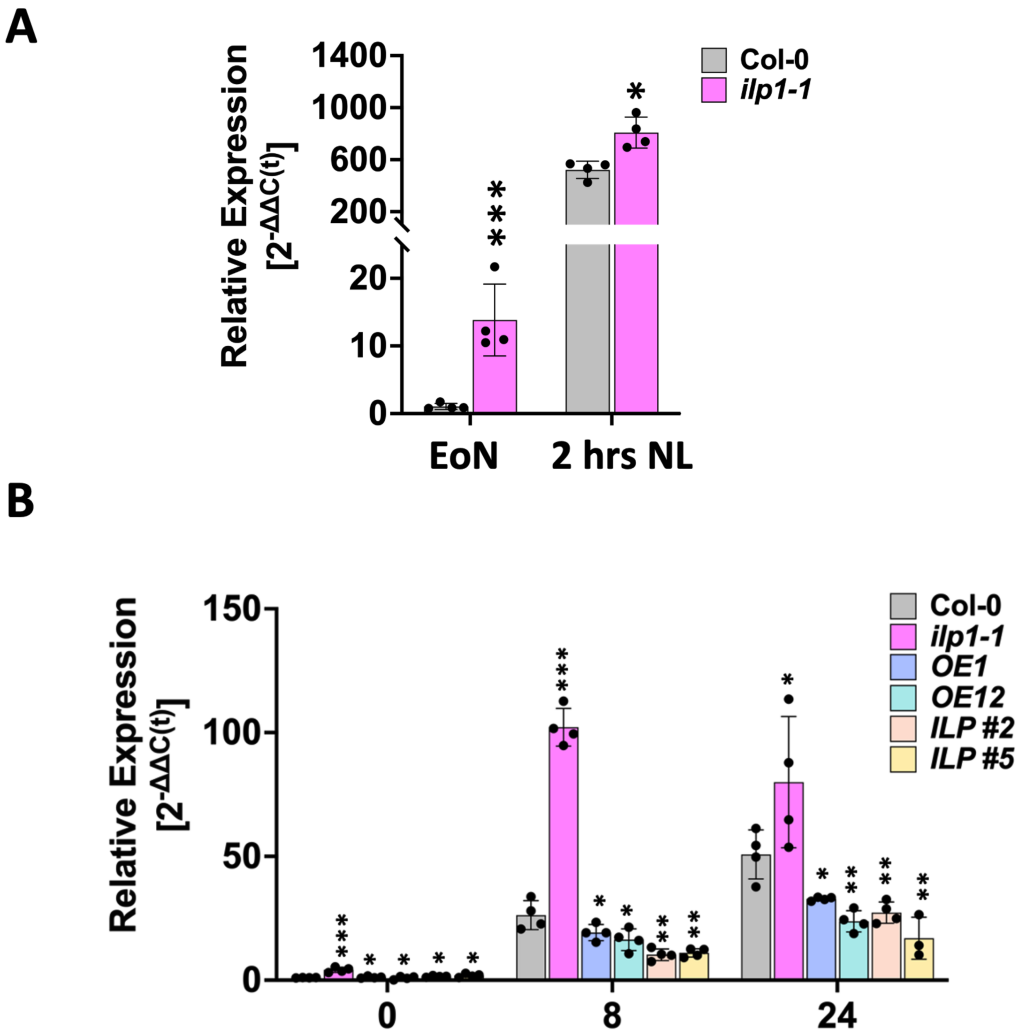

Figure S13. Relative expressions of *GPT2*. Transcript levels of *GPT2* in (A) 4-week-old plants during a normal day/night cycle at the End of Night (EoN) and 2 hours after normal light (NL) and (B) in 4-week-old OE and genetic complementation lines during HL exposure. Data are mean ± SD (n = 4). Asterisks indicate statistical significance compared to Col-0 by Student's t-test (*$P < 0.05$, ** $P < 0.01$, ***$P < 0.001$).

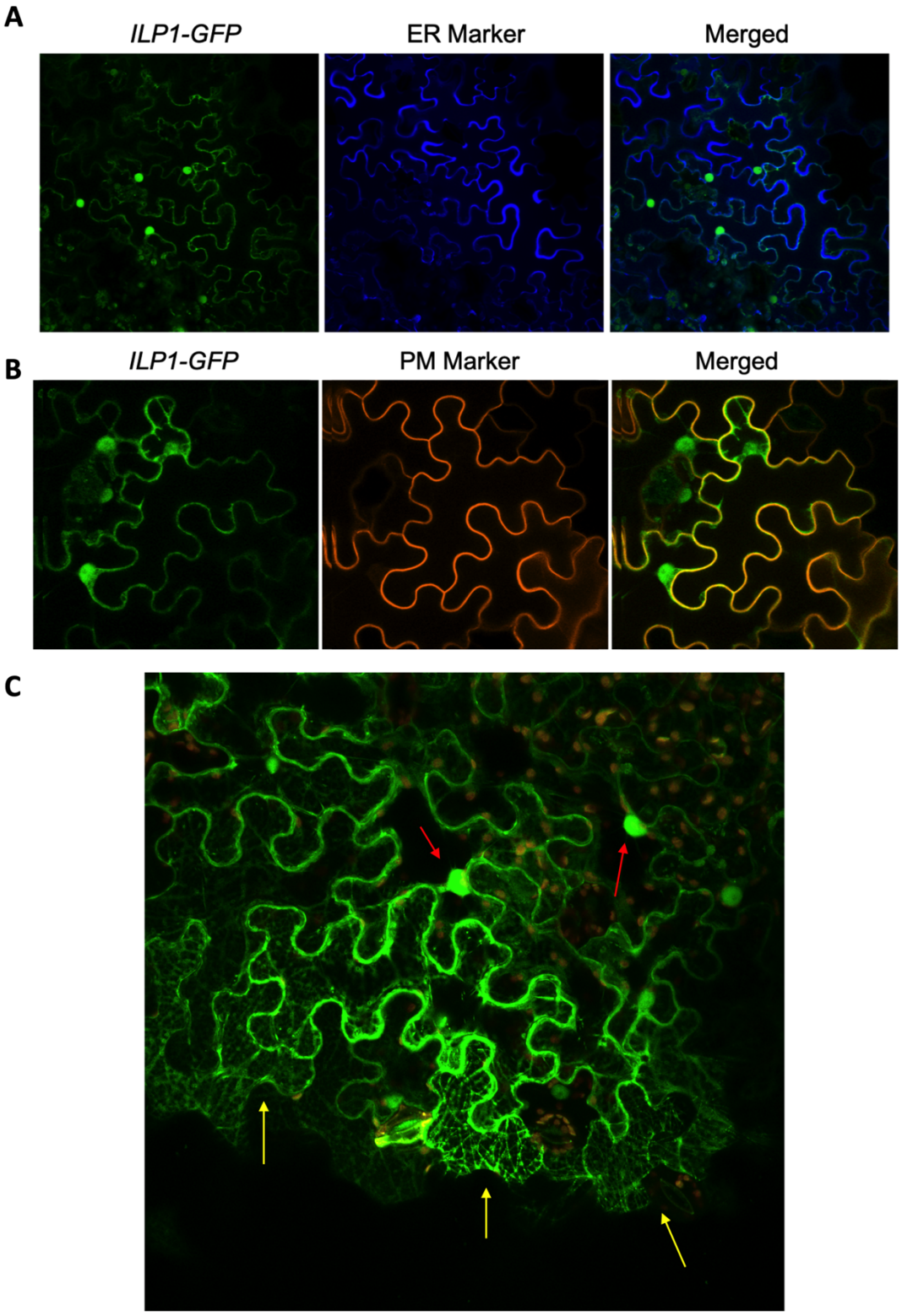

Figure S14. Subcellular localization of ILP1-GFP by transient expression in tobacco leaves. (A) Co-expression of ILP1-GFP and an ER marker (HDEL-mCherry), (B) co-expression of ILP1-GFP and a plasma membrane marker (CBL1-OFP), and (C) a Z-stack projection from 10 different slices.

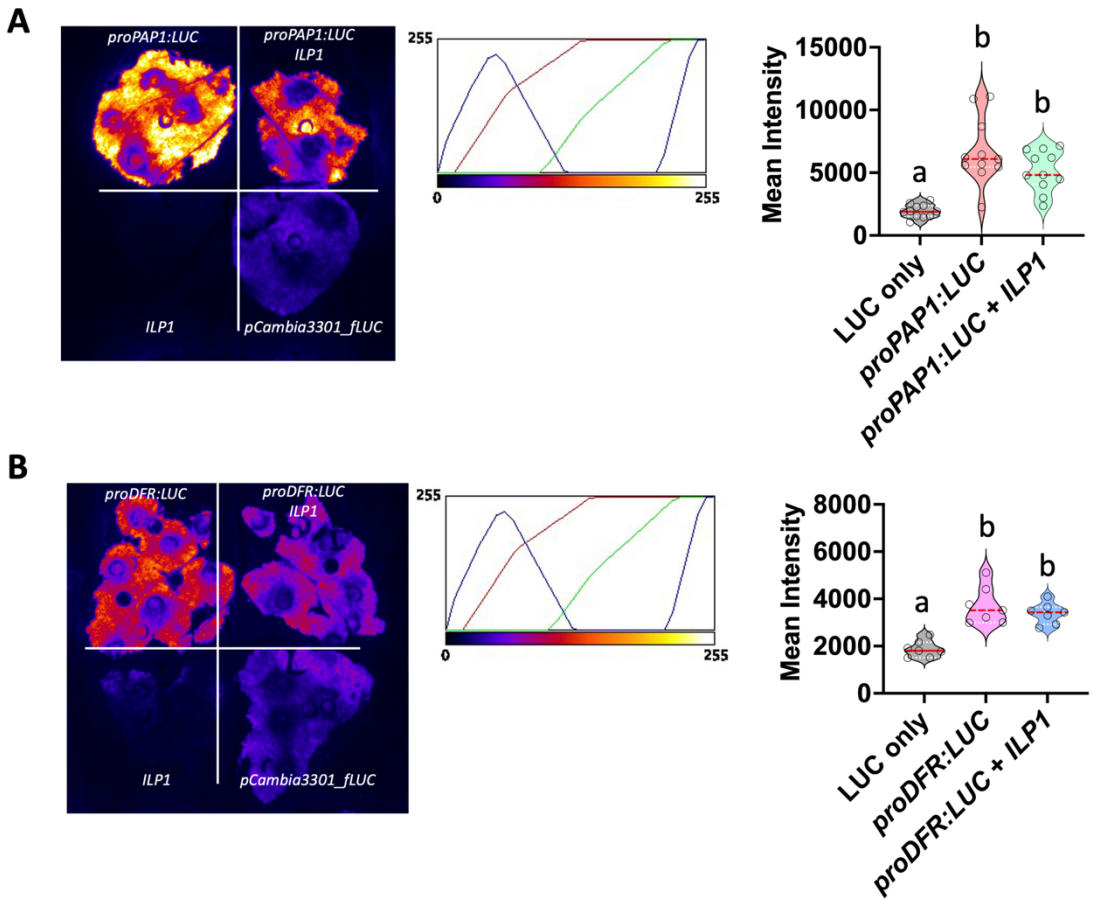

Figure S15. Quantitative in vivo transcriptional assay in tobacco leaves. Partial transcriptional repression of (A) *proPAP1:LUC* and (B) *proDFR:LUC* expressions in the presence of ILP1. The red lines inside the violins show the median of values and the white lines the quartiles. Different letters indicate significance groups at $P < 0.05$ by Šidák's and Tukey's multiple comparison tests, respectively, as determined by one-way ANOVA.

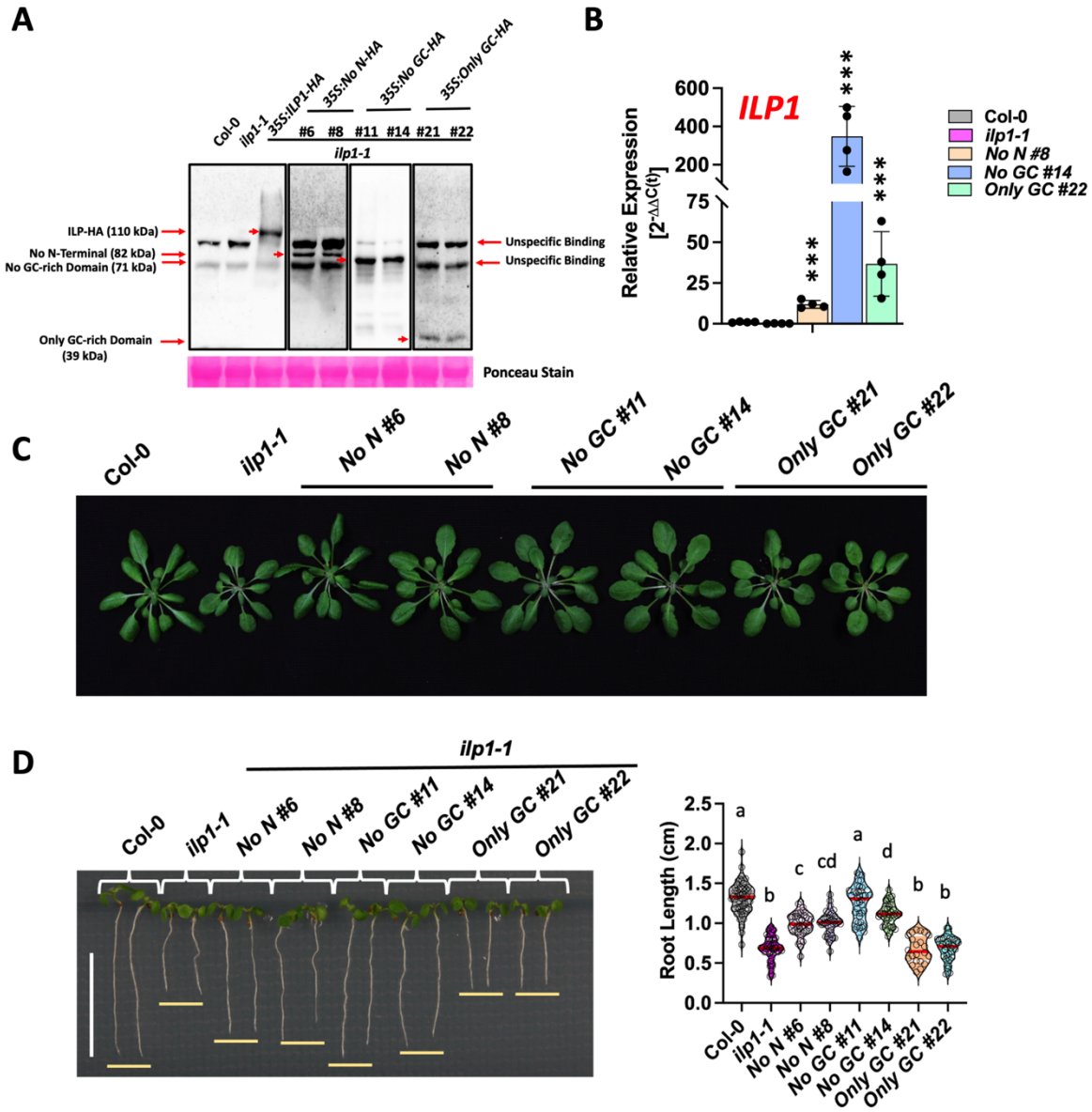

Figure S16. Generation and characterization of the truncated versions of ILP1. (A) Western blot of the different truncated constructs showing their specific sizes, (B) relative expression levels of the truncated versions, (C) rosette phenotypes of 4-week-old plants, and (D) root lengths of 7DAG seedlings. Data are mean ± SD. Asterisks indicate statistical significance compared to Col-0 by Student's t-test (***$P < 0.001$). The red lines inside the violins show the median of values and the white lines the quartiles. Different letters indicate significance groups at $P < 0.05$ by Šidák's and Tukey's multiple comparison tests, respectively, as determined by two-way ANOVA.

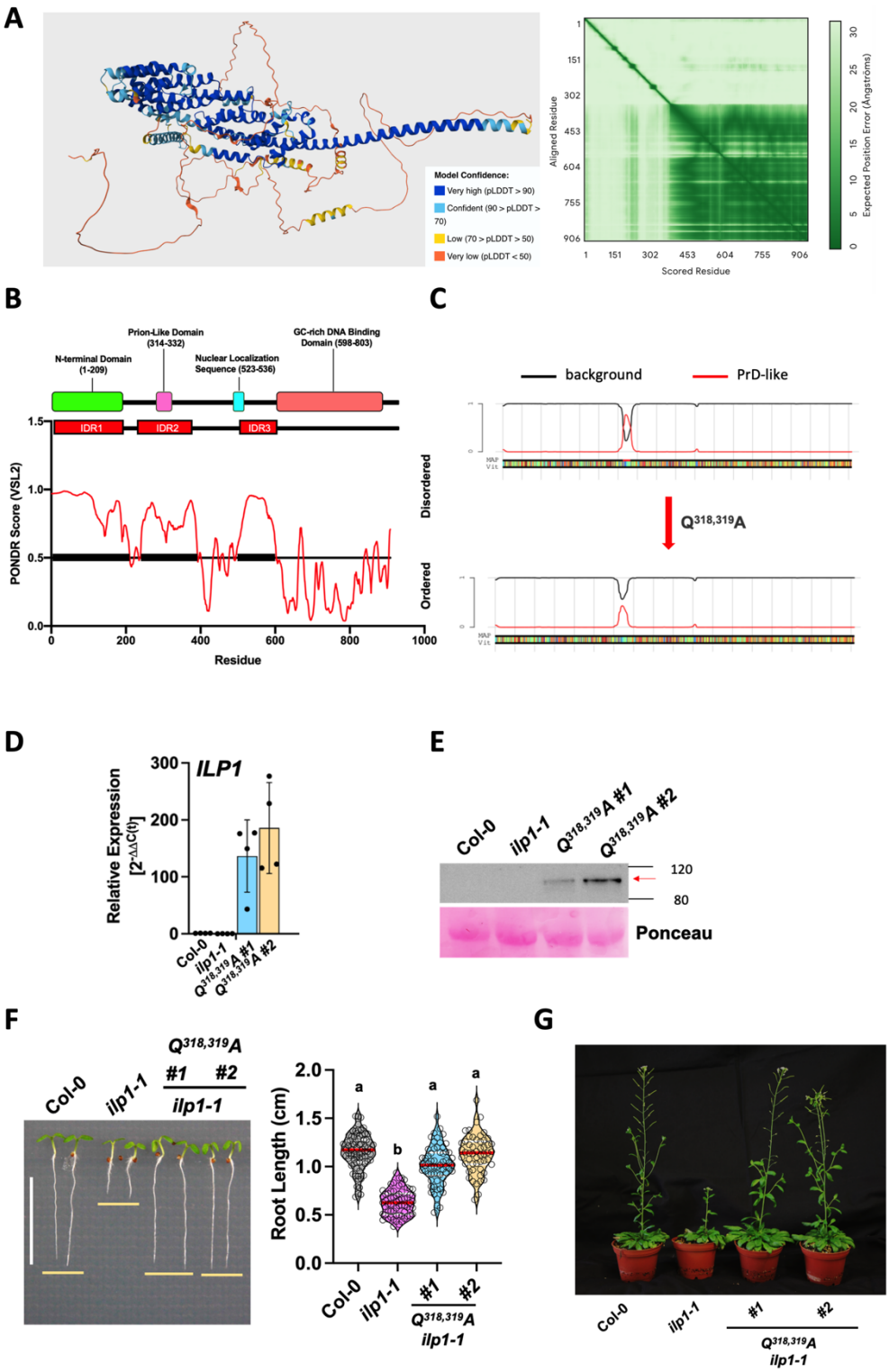

Figure S17. ILP1 is an intrinsically disorder protein. (A) Alphafold predicted structure of ILP1 in Arabidopsis (Jumper et al., 2021), (B) PONDR score showing the three disordered regions of ILP1, (C) double point mutation of the two adjacent glutamine (Q) disrupted the prion-like domain, (D) relative expressions and (E) western blot of the generated mutant lines in the *ilp1-1* background, and (F) root lengths of 7DAG seedlings and (G) their flowering times after 13 weeks under SD. Data are mean Data are mean ± SD. The red lines inside the violins show the median of values and the white lines the quartiles. Different letters indicate significance groups at $P < 0.05$ by Šidák's and Tukey's multiple comparison tests, respectively, as determined by two-way ANOVA.

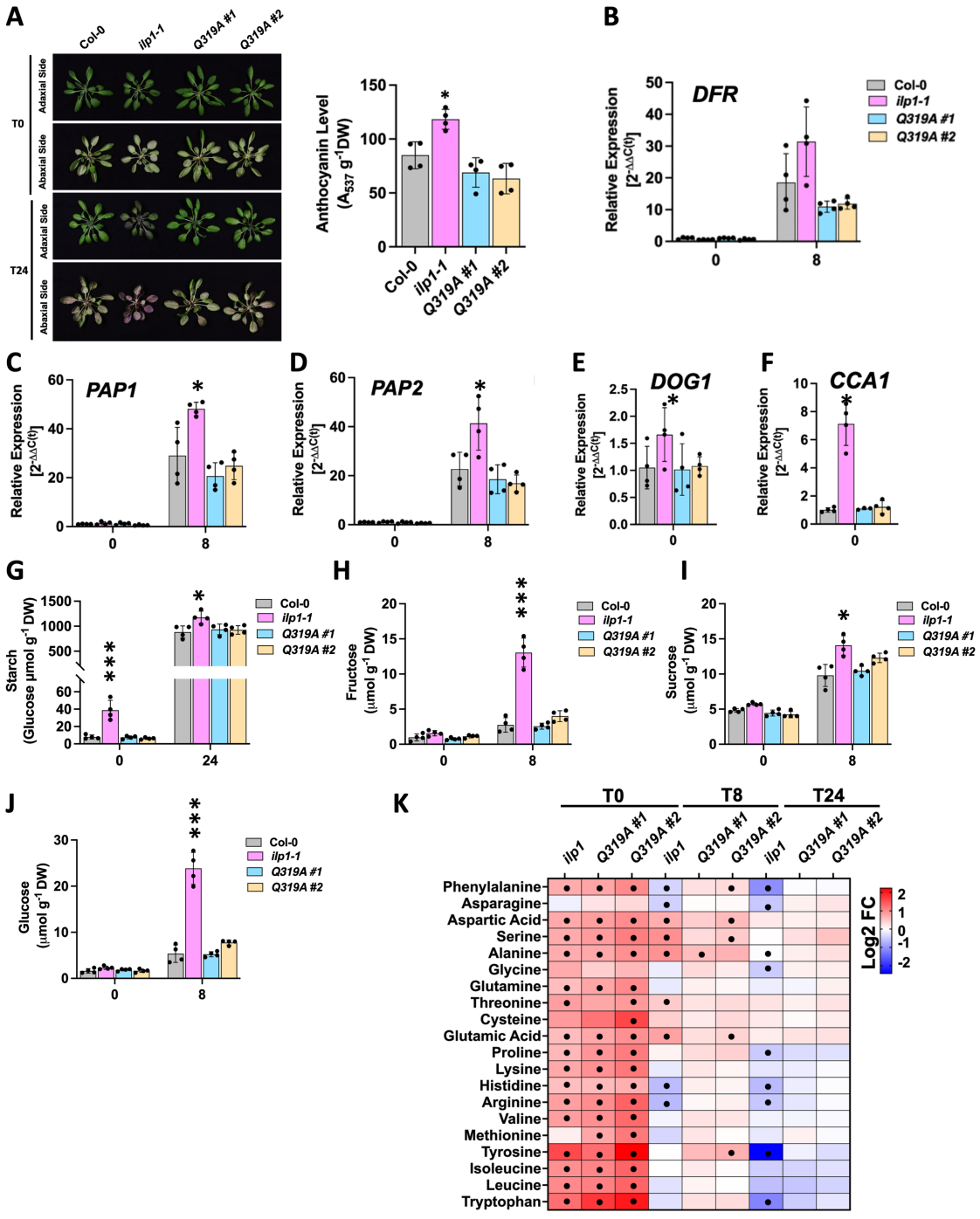

Figure S18. Acclimation response behavior of $Q^{518,519}A$ during high light exposure. (A) Anthocyanin contents, relative expressions of (B) DFR, (C) PAP1, (D) PAP2, (E) DOG1, (F) CCA1, (G) starch contents, (H) fructose, (I) sucrose, (J), and glucose levels, and (K) log2 FC of amino acids during HL. Data are mean ± SD. Asterisks indicate statistical significance compared to Col-0 by Student's t-test (*$P < 0.05$; **$P < 0.01$; ***$P < 0.001$). "•" in the heatmap indicates significance.

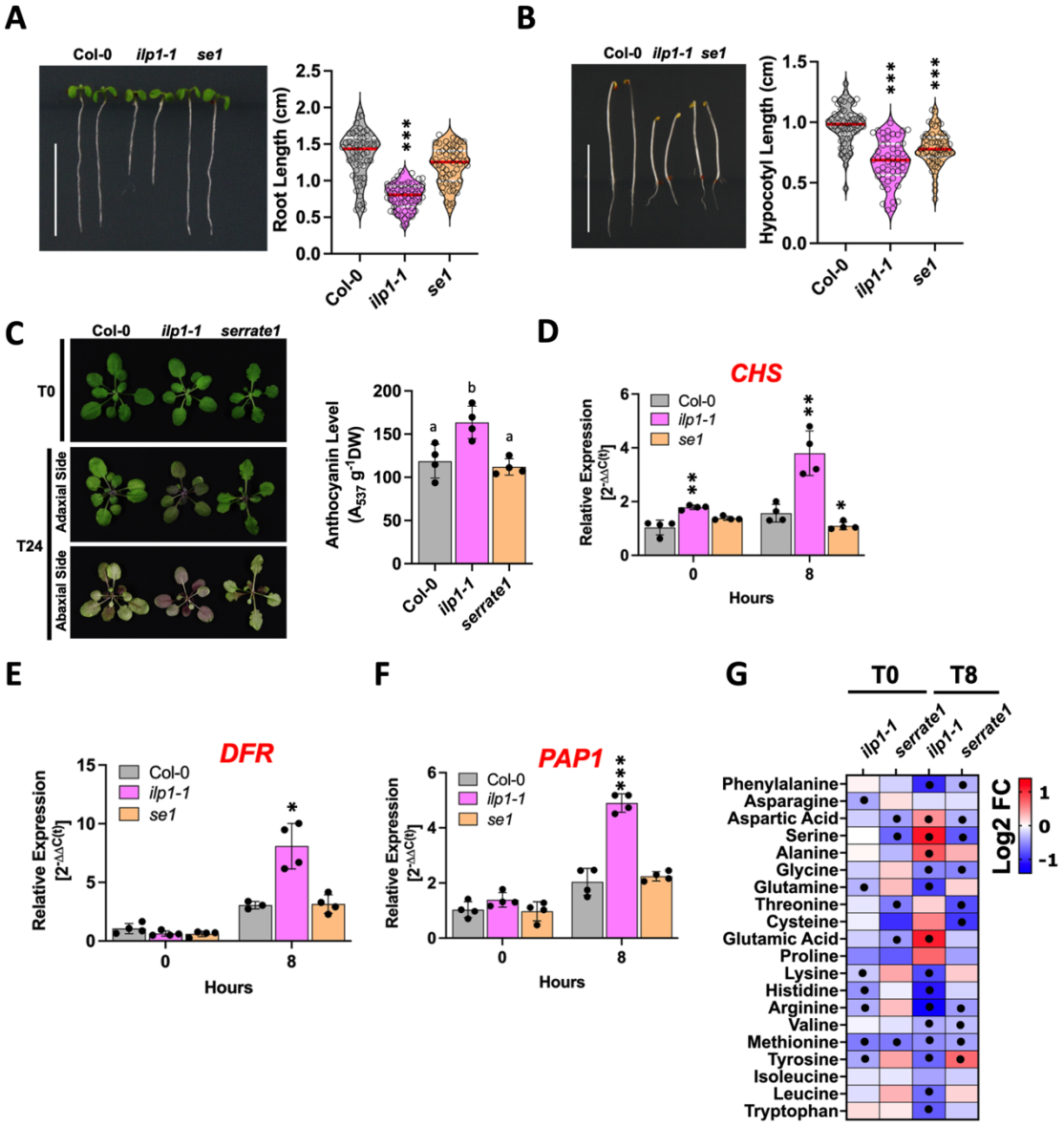

Figure S19. *se1,* a core mutant of miRNA biogenesis, shows a different response to acclimation. (A) Root lengths of 7 DAG seedlings, (B) hypocotyl lengths of 4DAG dark-grown seedlings, (C) anthocyanin accumulation after 24 hrs of HL, relative expressions of *CHS* (D), *DFR* (E), and *PAP1* (F) before and after 8 hrs of HL, and (G) log2 FC of amino acids during HL exposure. Data are mean ± SD. The red lines inside the violins show the median of values and the white lines the quartiles. Asterisks indicate statistical significance compared to Col-0 by Student's t-test (*$P < 0.05$; **$P < 0.01$; ***$P < 0.001$). "•" in the heatmap indicates significance.

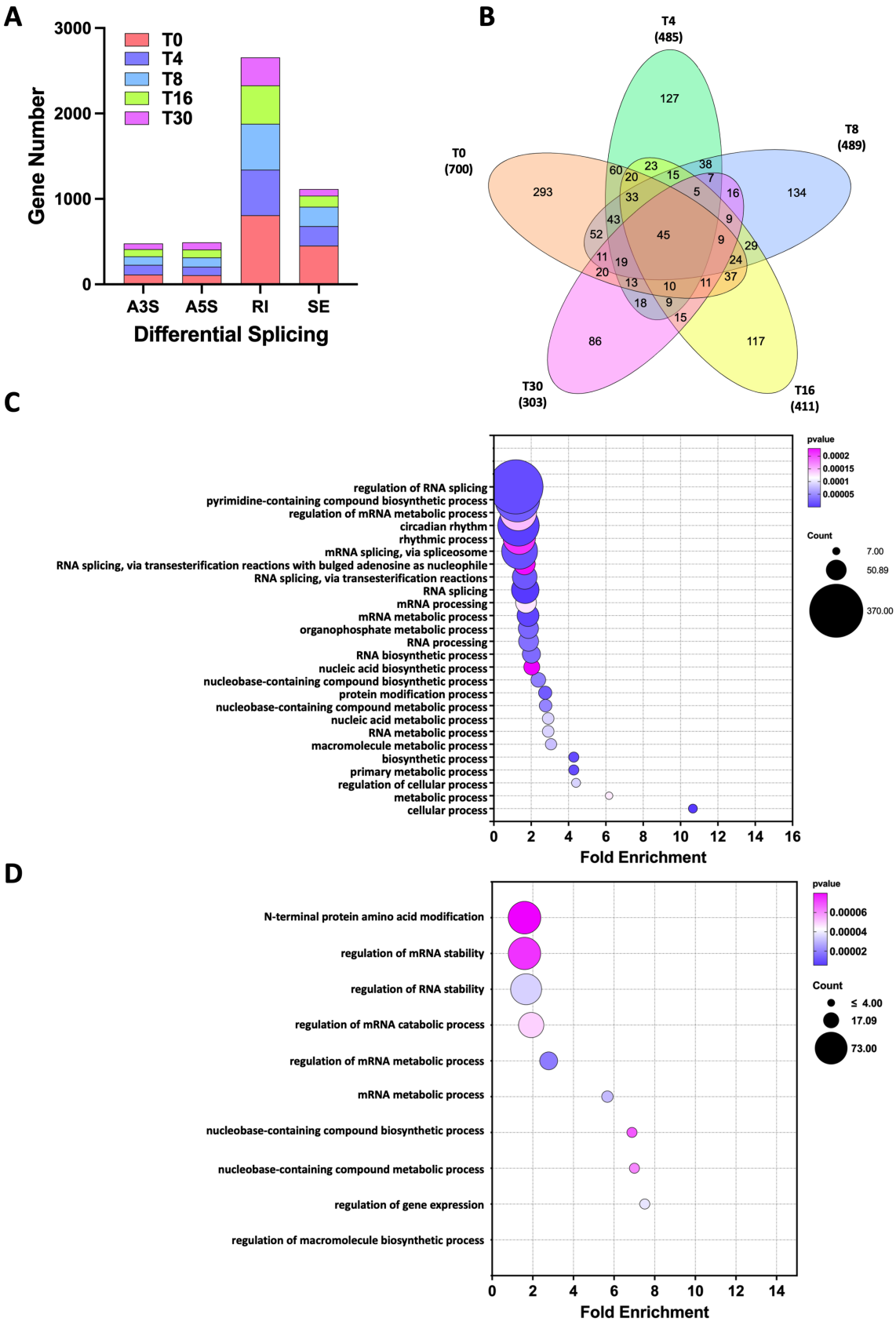

Figure S20. Differential splicing in *ilp1-1* during HL acclimation. (A) Gene count of differentially misspliced transcripts across various types of alternative splicing at different

time points, (B) venn diagram of genes with intron retention at different timepoints, and GO-term enrichment of differentially spliced transcripts with intron retention at (C) T0 and (D) T8. GO-term enrichment analysis was performed using https://geneontology.org/ and the venn diagram was constructed using https://www.interactivenn.net/ (Heberle et al., 2015).

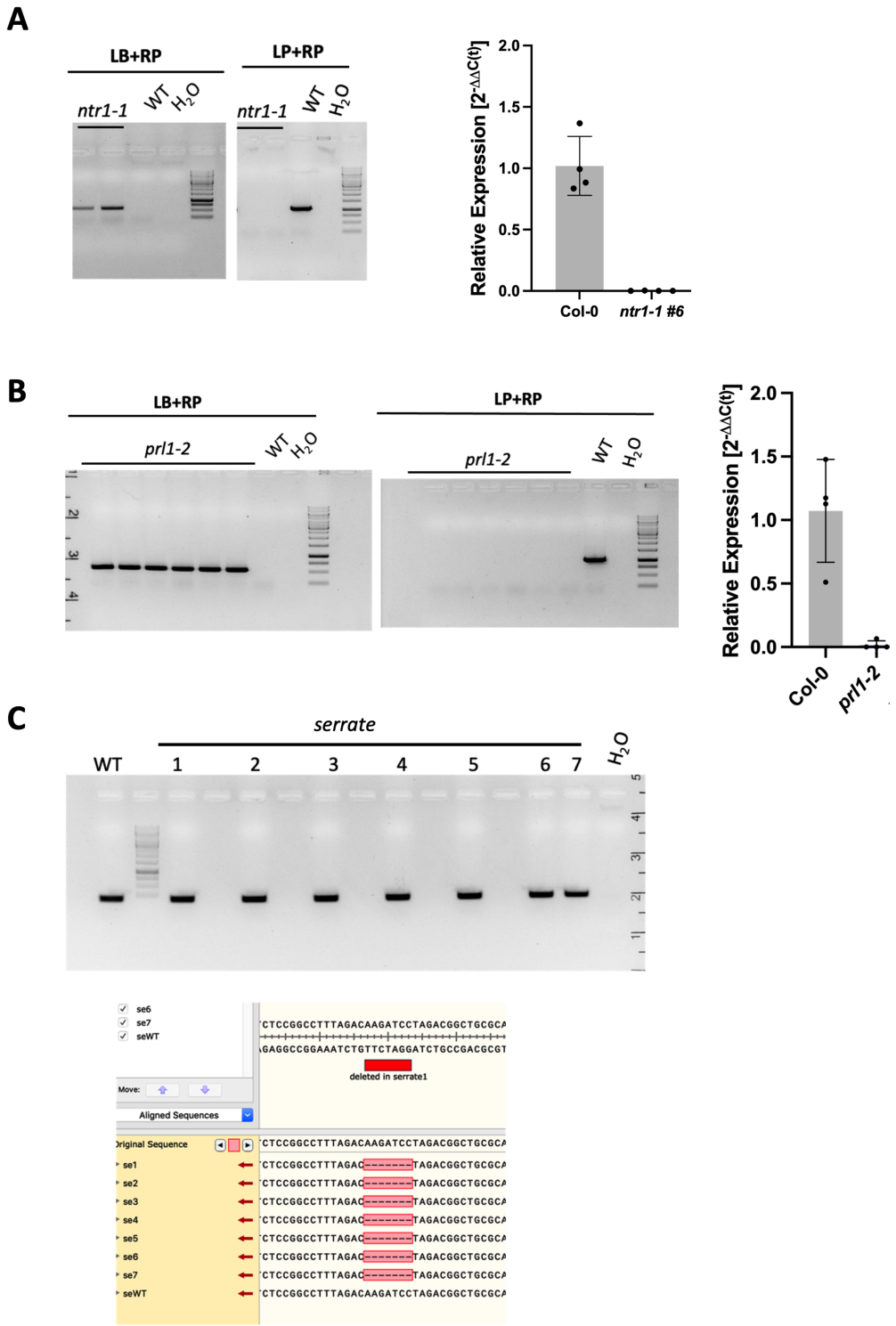

Figure S21. Genotyping of different mutants used in this study. (A) *ntr1-1*, (B) *prl1-2*, and (C) *serrate1*. Data are mean ± SD.

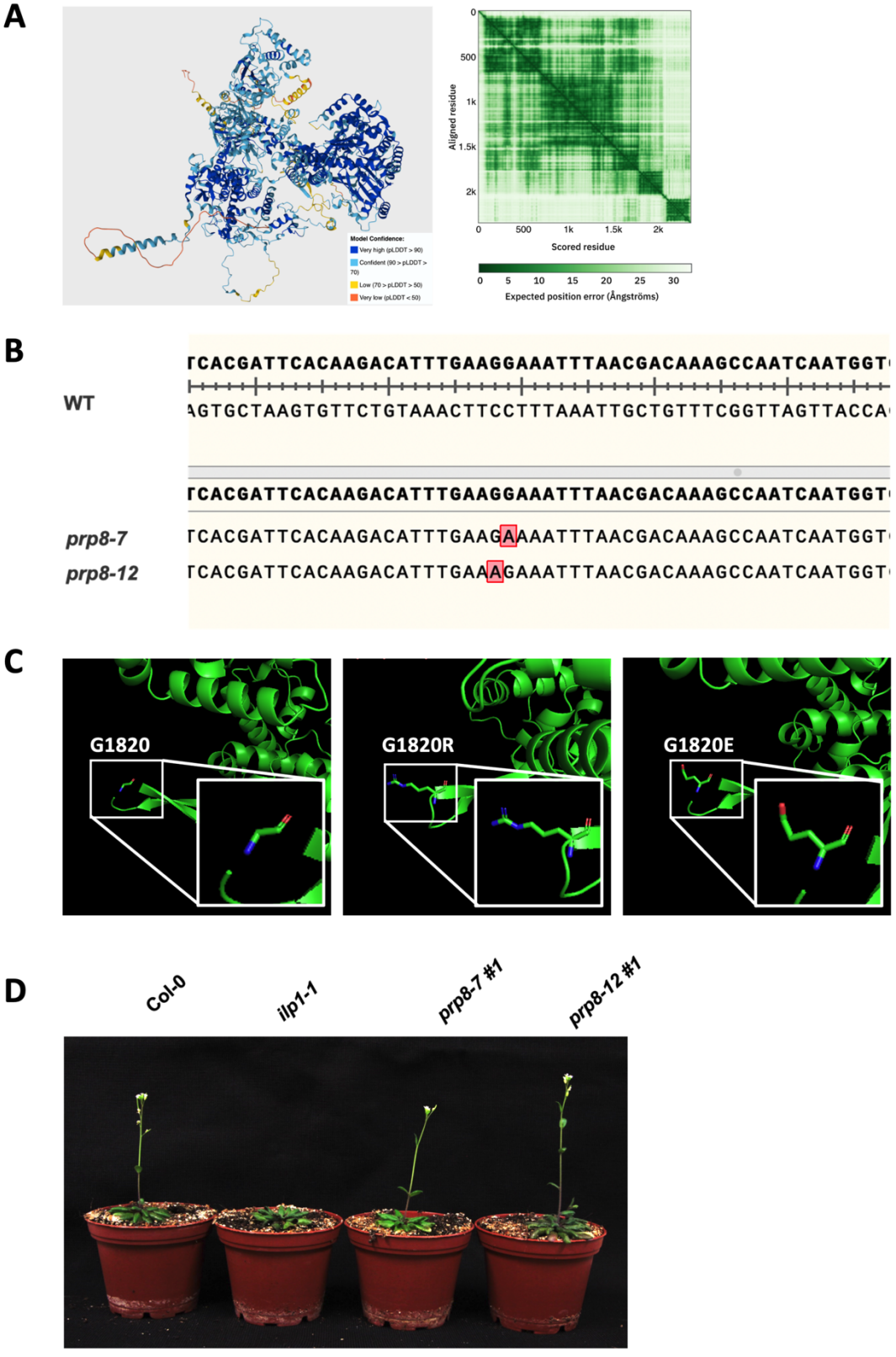

Figure S22. *PRP8* mutations. (A) Alphafold predicted structure of PRP8 in Arabidopsis (Jumper et al., 2021; Maradi et al., 2024), (B) positions of the point mutations in the 2 mutant alleles of *prp8*, (C) modeling of the amino acid changes in G1820 using PyMol (DeLano, 2002), and (D) flowering time of the *prp8* mutants.

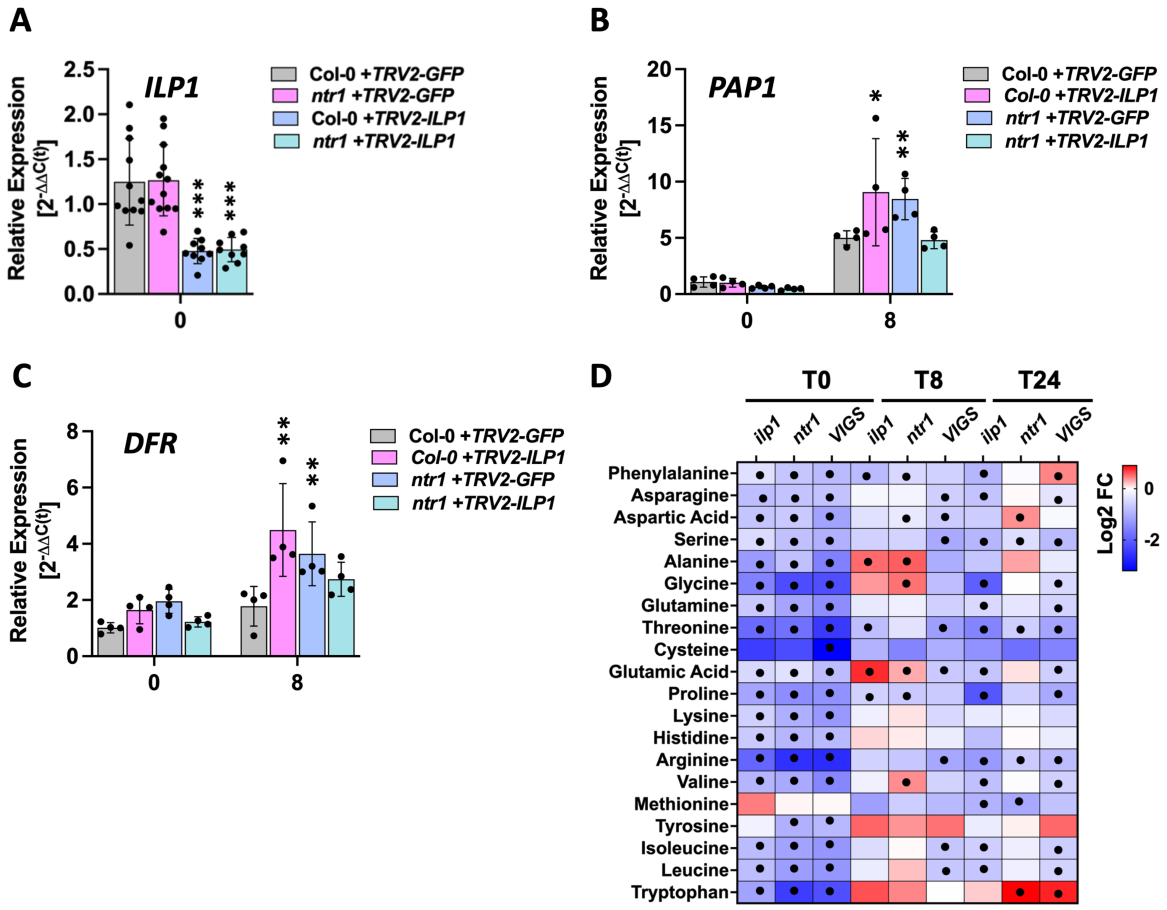

Figure S23. VIGS transcripts and metabolome. (A) mRNA transcripts of *ILP1* in the different VIGS constructs to confirm *ILP1* silencing, relative expressions of (B) *PAP1* and (C) *DFR* after 8 hrs of HL, and (D) log2 FC of quantified amino acids during HL exposure. Data are mean ± SD. Asterisks indicate statistical significance compared to Col-0 by Student's t-test (*$P < 0.05$, ** $P < 0.01$, ***$P < 0.001$). "•" in the heatmap indicates significance.

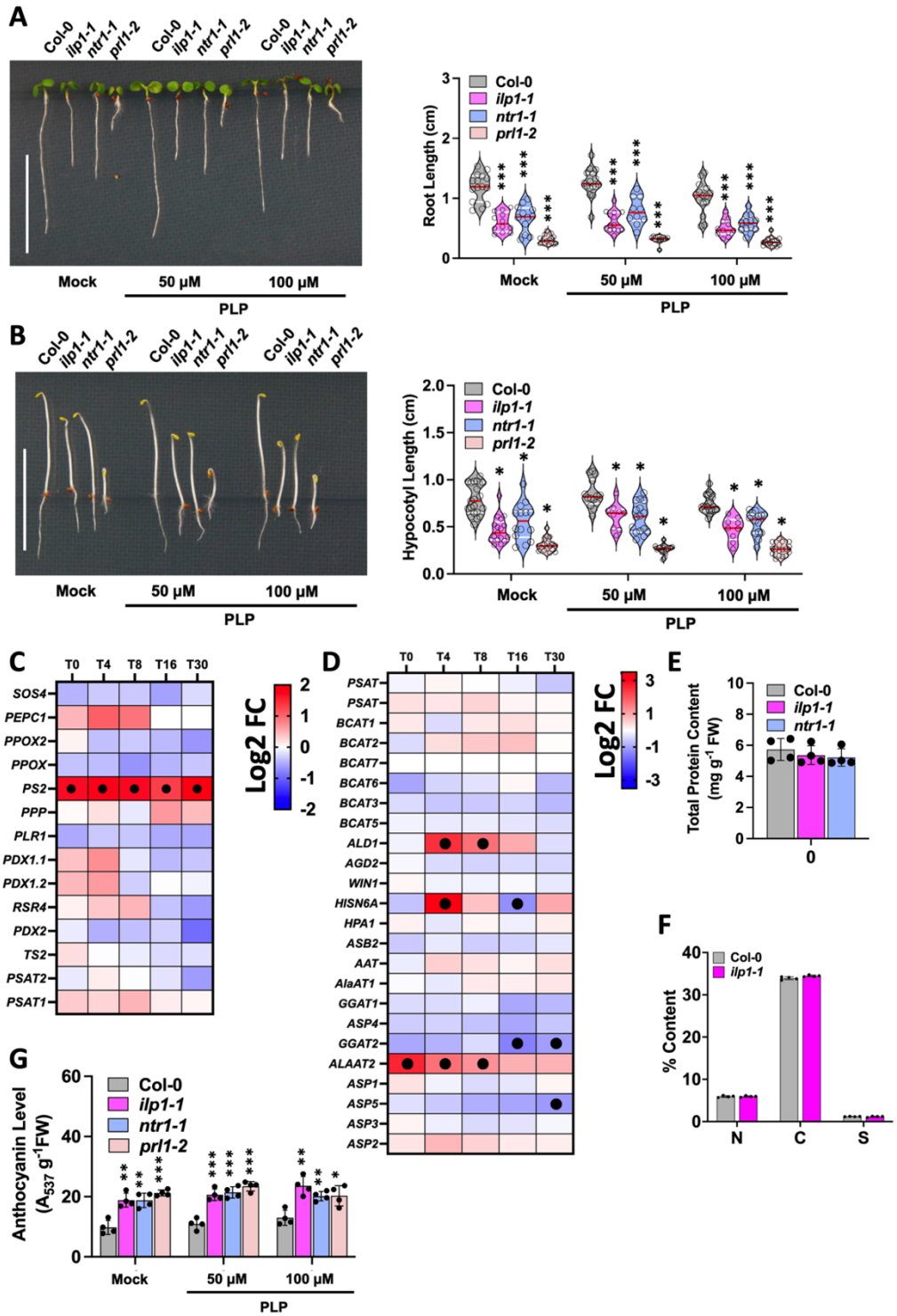

Figure S24. Effects of exogenous PLP on the spliceosomal mutants. (A) Root lengths of 7DAG seedlings with increasing concentration of PLP, (B) hypocotyl lengths of 4DAG dark-grown seedlings with increasing concentration of PLP, (C) enzymes involved in PLP biosynthesis and (D) aminotransferases and gene products involved in N-assimilation , (E) total protein content in Col-0, *ilp1-1*, and *ntr1-1*, (F) %content of nitrogen (N), carbon (C), and sulfur (S) in Col-0 and *ilp1-1*, and (G) effects of increasing concentration of PLP on anthocyanin levels in the spliceosomal mutants. Data are mean ± SD. Asterisks indicate statistical significance compared to Col-0 by Student's t-test (*$P < 0.05$, ** $P < 0.01$, ***$P < 0.001$). The red lines inside the violins show the median of values and the white lines the quartiles. "•" in the heatmap indicates significance.

Table S1. List of all oligonucleotides used in this study.

Code/Name	Sequence (5'->3')	Purpose
GA01	ATTTTGCCGATTTCGGAAC	LB; genotyping
GA13	TATTCTCCAGGTTCCGACATG	*ilp1-1* LP; genotyping
GA14	GATGAGCCTTTGCTGGTACAG	*ilp1-1* and *ilp1-2* RP; genotyping
GA15	ATGTTTCTGCTTCGAGTGAGG	*ilp1-2* LP; genotyping
GA16	TCGCGACAAGCTTTCATCGCTAG	*pILP1:ILP1* cloning
GA17	TCGCGACAACAGCTTCCTGACTTC	*pILP11:ILP1* cloning
GA18	TCGCGAATGGGAAGTAACCGTCC	*p35S:ILP1* cloning
GA90	TCGCGAAACTGCCTCCTTAAGATTG	*p35S1:ILP1* cloning
GA26	CATCTTCATGCTGCTCTTCTTCCCC	*ILP1* transgene genotyping
GA44	CCACTGACGTAAGGGATGACGC	*ILP1* transgene genotyping
GA38	GGGAATCTCATTCGTCTTAGACC	endogenous *ILP1* genotyping
GA344	GTCCGGTAGTGATGAAAATGCAAGGC	endogenous *ILP1* genotyping
GA47	GGACAGGACCAAGCGTCACAC	qPCR *ILP1* mRNA levels
GA48	GCGTGGTCATGTTCATGGAGC	qPCR *ILP1* mRNA levels
GA103	GGAAGTATTTGCGCAAGAGCAG	qPCR *NTR1* mRNA levels
GA104	CCAACCGCCATCTTTCTGAGC	qPCR *NTR1* mRNA levels
GA107	CATAAGGTTGGCCAAGAGTCC	*ntr1-1* LP, genotyping
GA108	ACTGCCTTCCTCACCTTCTTC	*ntr1-1* RP, genotyping
GA109	GAAGGTAGCGGGAGAGGTG	*SERRATE1* for sequencing
GA110	GGTCACTTCTTCCTCTGGAGC	*SERRATE1* for sequencing
GA113	GGGACTGGAAGAGTGGTCACA	qPCR *PRL1* mRNA levels
GA114	CGTCTTATCAGCCTCGCATGT	qPCR *PRL1* mRNA levels
GA117	GACCTTCAAATGCTCTTTCCC	*prl1-2* RP, genotyping
GA118	CTGCTTCTACAATCGCCAAAG	*prl1-2* LP, genotyping
GA149	GGACATGACAACACCGTTTGTTCTG	*raa7* and *raa14* SNP sequencing
GA168	GCATTCTAAACAGCAGACACTGCCAGCACAGCAACCGCAGATGTATGCTTATC	prion Q318A
GA245	CAGACACTGCCAGCAGCGCAACCGCAGATGTATG	Q319A_new_F prion Q318,319A
GA246	CATACATCTGCGGTTGCGCTGCTGGCAGTGTCTG	Q319A_new_R prion Q318,319A
GA308	TCGCGATACATATCACTAGATGGTGGTA	no start_no N-terminal Domain

GA309	TCGCGACTTTCAAAGGTGAAGGC	no start_only GC rich
GA310	TCGCGAGGAAGTAACCGTCCTAAG	no start_no GC rich
GA419	GTGTAATGATTGGGCTTGATCTGGCATAC	prp8-12_F
GA420	GGAGAGATCGCACAAGTGCAGC	prp8-12_R
GA421	CCAATCCGGCTCTATATGTGTTGAGAG	prp8-12 sequencing
GA422	CCATCTCCAACAGGTGTAATGATTGGG	prp8-7 F
GA423	CCATCTGCGGTTCTGTAGCCTTC	prp8-7 R
GA424	CCTGCATTCTGCCTTTGGTAATTGG	prp8-7 sequencing
SAND	AACTCTATGCAGCATTTGATCCACT	qPCR (F)
SAND	TGATTGCATATCTTTATCGCCATC	qPCR (R)
PAP1	GGCACCAAGTTCCTGTAAGAG	qPCR (F)
PAP1	CCTATGAAGGCGAAGAAGAAGA	qPCR (R)
DFR	CGCCAAGACGCTACTCACT	qPCR (F)
DFR	CGGCTTTATCACTTCGTTCTCA	qPCR (R)
CHS	GGTCTCACCTTCCATCTCCT	qPCR (F)
CHS	AGTATGAAGAGAACGCACGC	qPCR (R)
FLS1	AGTATATTCCCTCCGCCGT	qPCR (F)
FLS1	CTCTTTATCCACCGTCGTCC	qPCR (R)
APX1	TCGAGAAATACGCTGCTGATG	qPCR (F)
APX1	ACACAGAGCATACGTCACAG	qPCR (R)
DOG1_Exon2_F	CAAGGAGCGGATTTCTTGCTCGC	qPCR / targeted splicing analysis
DOG1_Intron2_R	CTACTTTCCTTCCTCTCCTCCGGC	qPCR / targeted splicing analysis
CCA1_Exon6_F	GCCGCAGTAGAATCAGCTCCAA	qPCR / targeted splicing analysis
CCA1_Intron6_R	GGAAGTTGATCTTTAGTCCAAGTAAG	qPCR / targeted splicing analysis

Appendix B: List of Abbreviations

2,4-D	2,4-Dichlorophenoxyacetic acid
µL	microLiter
µM	micromolar
4CL	4-Coumarate:CoA Ligase
A3S	Alternative 3' splice site
A5S	Alternative 5' splice site
A. tumefaciens	Agrobacterium tumefaciens
ABA	abscisic acid
At	Arabidopsis thaliana
ATP	adenosine triphosphate
BAP	6-Benzylaminopurine
bHLH	Basic Helix-Loop-Helix
bp	base pair
BR	Brassinosteroids
C4H	Cinnamic acid 4-Hydroxylase
CCA1	Circadian Clock Associated 1
cDNA	complementary DNA
CDS	Coding sequence
CHI	Chalcone Isomerase
CHS	Chalcone Synthase
CK	Cytokinin
Col-0	wild-type Arabidopsis ecotype Columbia-0
DAB	3,3'-diaminobenzidine
DCMU	3-(3,4-dichlorophenyl)-1,1-dimethylurea
DEG	Differentially Expressed Gene
DFR	Dihydroflavonol 4-Reductase
DMSO	Dimethyl sulfoxide
DOG1	Delay of Germination1
DTT	Dithiothreitol
E. coli	Escherichia coli
EBGs	Early Biosynthetic Genes
EDTA	Ethylenediaminetetraacetic Acid
EMS	Ethylmethanesulfonate
F3H	Flavanone 3-Hydroxylase
FC	Fold Change
FLS1	Flavonol Synthase1
GA	Gibberellic acid
GC/MS	Gas Chromatography/Mass Spectrometry
GFP	Green Fluorescent Protein
GL3	Glabra3
GO-term	Gene Ontology-term
GST26	Glutathione S-transferase26

GUN5	Genomes Uncoupled5
GPT2	Glucose-6-Phosphate/Phosphate Translocator2
HL	High Light
HCl	hydrochloric acid
hr/s	hour/hours
IAA	Indole-3-acetic acid
IDP	Intrinsically Disordered Protein
IDR	Intrinsically Disordered Region
ILP1	Increased Level of Polyploidy1
ILS	Intron Lariat Spliceosome
JA	Jasmonic Acid
kb	kilobase pair/s
LB	Luria Broth
LBGs	Late Biosynthetic Genes
LDOX	Leucoannthocyanidin Dioxygenase
LC/MS	Liquid Chromatography/Mass Spectrometry
MBW	MYB-bHLH-WD40
miRNA	microRNA
mRNA	messenger RNA
MYB	Myeloblastosis
MYBL2	MYB-Related Protein2
NBT	Nitroblue tetrazolium chloride
NLS	Nuclear Localization Sequence
nm	nanometer
nM	nanomolar
NTR1	NTC-related Protein1
PAL1	Phenylalanine Ammonia Lyase1
PAP1	Production of Anthocyanin Pigment1
PAP2	Production of Anthocyanin Pigment2
PRL1	Pleiotropic Regulatory Locus1
PRP8	pre-mRNA Processing8
PCR	Polymerase Chain Reaction
qPCR	quantitative real-time PCR
RAA	Restored Anthocyanin Accumulation
RI	Retained Intron/Intron Retention
ROS	reactive oxygen species
RT	Root Temperature
SA	Salicylic acid
SE	Skipping Exon
Se1	Serrate1
S.D.	standard deviation
SDM	Site Directed Mutagenesis
SDS	sodium dodecyl sulfate
SNP	Single Nucleotide Polymorphism
SnRK1	SNF1-related Kinase1
TCA	Tricarboxylic Acid
T6P	Trehalose-6-Phosphate
TPT	Triose Phosphate Translocator
TTG1	Transparent Testa Glabra1

UF3GT	UDP-glucose:flavonoid 3-o-glucosyltransferase
VIGS	Virus-Induced Gene Silencing
v/v	volume per volume
WT	Wild Type/Col-0
w/v	weight per volume
Vol	Volume
YEB	Yeast Extract Beef Broth

List of Figures

List of Tables

CURRICULUM VITAE

Place of Birth: Sorsogon City, Philippines
Email: gearaguirang@icloud.com
Google Scholar: http://tiny.cc/102073/2168
ORCID: 0000-0002-1600-4183
Personal Website: gearaguirang.com

EDUCATION

05/2021 – 07/2025	**PhD Candidate (Biology),** Universität Rostock, Germany
10/2020 - 04/2021	**PhD Candidate (Biology),** Humboldt Universität zu Berlin, Germany (the whole lab moved to Universität Rostock, Germany in May 2021)
10/2019 - 08/2020	**PhD Candidate (Biochemistry)** under the International Max Planck Research School (IMPRS-PMPG) PhD Program of the Max Planck Institute of Molecular Plant Physiology; IGZ Leibniz, Germany Degree-Granting University: University of Potsdam, Germany
2015 - 2018	**MSc Molecular Biology and Biotechnology**, University of the Philippines Los Baños (UPLB), Philippines (Grade: 1.53; "Very Good") Academic Adviser: Maribel L. Dionisio-Sese, D. Sc.
2017	**MSc Thesis Student**, Molecular Plant Physiology and Photobiology Laboratory, Philipps-Universität Marburg, Germany (Grade: 1.00; "Excellent") MSc Thesis Host Professor: Prof. Dr. Alfred Batschauer
2016	**Winter School on Quantitative Systems Biology** (highly competitive), International Center for Theoretical Physics (ICTP), Trieste, Italy
2009 - 2013	**BSc Biology** (major in Cell and Molecular Biology), UPLB, Philippines ***Cum laude* (With Distinction),**
2006-2009	**High School (with Honors)**, Top 1% of the graduating class, Sorsogon National High School, Sorsogon City, Philippines

RESEARCH EXPERIENCE

2024 – Present	**Project: Regulation of Clathrin-Mediated Endocytosis by Ubiquitination** Molecular Plant Physiology, RWTH Aachen University Supervisor: Prof. Marco Trujillo
2020 - 2024	**Project: Anthocyanin Biosynthesis and High Light Acclimation in Arabidopsis** Physiology of Plant Cell Organelles, Humboldt Universität zu Berlin, Germany and Physiology of Plant Metabolism, Universität Rostock, Germany Supervisor: Jun. Prof. Andreas S. Richter
2019 - 2020	**Project: Temperature Sensing and Energy Signaling in Arabidopsis** IGZ Leibniz, Großbeeren, Germany Supervisor: Prof. Philip Wigge
2018 - 2019	**Projects: (1) CEK Family in Phospholipid Metabolism and (2) Choline Transporter-Like (CTL) Proteins in Arabidopsis** Institute of Plant and Microbial Biology, Academia Sinica, Taipei, Taiwan Supervisor: Dr. Yuki Nakamura
2018	**TIGP Summer Intern** (10% success rate), Yuki Nakamura Laboratory, Taiwan International Graduate Program-International Internship Program (TIGP-IIP), Academia Sinica, Taipei, Taiwan
2018	**Teaching Assistant/Graduate Student Apprentice**, UP Graduate Mentoring Apprenticeship Program (GMAP) Faculty Mentor: Maribel L. Dionisio-Sese, D. Sc. Courses Taught/Assisted: Elementary Plant Physiology (Undergraduate) and Plant Photophysiology (Graduate)
2017	**MSc Thesis Student**, Molecular Plant Physiology and Photobiology Laboratory, Philipps-Universität Marburg, Germany MSc Thesis Host Professor: Prof. Dr. Alfred Batschauer MSc Thesis: *"In vitro and In vivo Characterization of Arabidopsis Cryptochrome 2 (cry2) I404F Photoreceptor and the Effects of Metabolite Binding on its Structure and Photobiochemical Properties"*

2014 **University Research Associate** (DOST-PCIEERD Project), Food and Feeds Laboratory, National Institute of Molecular Biology and Biotechnology, UPLB
Project: Development of a dipstick assay format for detection of Salmonellae in food and feeds

2013-2014 **University Research Associate** (RIHN-LakeHEAD Project), Under Professor Emeritus Macrina Tamayo-Zafaralla, Institute of Biological Sciences, College of Arts and Sciences, UPLB
Project: Water quality assessment and understanding the influences of rainfall in the offshore waters of five barangays along West Bay of Laguna de Bay, Philippines

PUBLICATIONS

8. **Araguirang GE**, Venn B, Kelber NM, Feil R, Lunn J, Kleine T, Leister D, Mühlhaus T, and Richter AS. (2023) "Spliceosomal complex components are critical for adjusting the C:N balance during high-light acclimation" *The Plant Journal* https://doi.org/10.1111/tpj.16751

7. **Araguirang GE**, Venn B, Kelber NM, Feil R, Lunn J, Kleine T, Leister D, Mühlhaus T, and Richter AS. (2023) "Spliceosomal complex components are critical for adjusting the C:N balance during high-light acclimation" BioRxiv https://doi.org/10.1101/2023.07.19.549727 [now in *The Plant Journal*, see Publication #8]

6. **Araguirang GE** and Richter AS. (2022) "Activation of anthocyanin biosynthesis in high light – what is the initial signal?" *New Phytologist 236: 2037-2043*. https://doi.org/10.1111/nph.18488

5. Zirngibl ME, **Araguirang GE**, Kitashova A, Jahnke K, Rolka T, Kühn C, Nägele T, and Richter AS. (2022) "Triosephosphate export from chloroplasts and cellular sugar content regulate anthocyanin biosynthesis during high light acclimation" *Plant Communications* https://doi.org/10.1016/j.xplc.2022.100423

4. Zirngibl ME, **Araguirang GE**, Kitashova A, Jahnke K, Rolka T, Kühn C, Nägele T, and Richter AS. (2022) "Triosephosphate export from chloroplasts regulates flavonoid biosynthesis and permits high light acclimation through the inactivation of SnRK1" BioRxiv https://doi.org/10.1101/2022.03.09.483619 [now in Plant Communications; see Publication #5]

3. Lin YC*, **Araguirang GE***, Ngo AH*, Lin KT, Angkawijaya AE, and Nakamura Y. (2020) "The Four Arabidopsis Choline/Ethanolamine Kinase Isozymes Play Distinct Roles in Metabolism and Development" *Plant*

Physiology 183: 152-166. https://doi.org/10.1104/pp.19.01399 (*equal contribution)

2. **Araguirang GE**, Niemann N, Kiontke S, Eckel M, Dionisio-Sese ML, and Batschauer A. (2020) "The Arabidopsis cryptochrome 2 I404F mutant is hypersensitive and shows flavin reduction even in the absence of light" *Planta 251:33*. https://doi.org/10.1007/s00425-019-03323-y

1. **Araguirang GE**, Arizala AJR, Asilo EBB, Batalon JLS, Bello EB, Madigal JPT, Monge JR, Sanchez NAL, and Elegado FB. (2020) "Pre-Treatment and Enzymatic Hydrolysis of Banana (Musa acuminata x balbisiana) Pseudostem for Ethanol Production" *Agro Bali: Agricultural Journal 3 (2): 98-107* https://doi.org/10.37637/ab.v3i2.608

FEATURED PROFILES

2. **Araguirang GE. (**2022**)** *New Phytologist 236: 2016-2018.* https://doi.org/10.1111/nph.18444

1. **Recognized in Plant Physiology: First Author Profiles** for the Research Article "The Four Arabidopsis Choline/Ethanolamine Kinase Isozymes Play Distinct Roles in Metabolism and Development" https://plantae.org/recognizing-plant-physiology-authors-galileo-estopare-araguirang/

HONORS AND AWARDS

2023	**Reinhold-von-Sengbusch Best Poster Award** (out of ~100 posters), Molecular Biology of Plants Conference (Plant Physiology and Molecular Biology Section of the DBG), February 6-9, 2023, Hennef, Germany
2022	**European Molecular Biology Laboratory (EMBL) Best Poster Award** (out of ~150 Participants), 24th EMBL PhD Symposium (The Spectra of Life: Dimensional Breadth in Biological Research), December 07-09, 2022, EMBL, Heidelberg, Germany
2022	**Botanik Tagung Best Poster Award** (Rank 1 from the Top 10 Best Posters out of 309 posters), Botanik Tagung 2022, Aug. 28 - Sept. 1, 2022, University of Bonn, Germany
2022	**New Phytologist Best Poster Award** (out of ~100 posters), New Phytologist's Next Generation Scientist 2022, July 19-22, 2022, University of Tartu, Estonia
2019-2020	**IMPRS-PMPG PhD Candidate**, MPI-MP and IGZ Leibniz, Germany

2014	**Selected Interviewee**, 3rd Asian Chemical Biology Initiatives (ACBI) Students Interview Session, Manila Hotel, Philippines, chosen as one of the top 46 all over the Philippines to be invited
2013	***Cum laude* (With Distinction)**, BS Biology Major in Cell and Molecular Biology, UPLB
2013	**Recipient of the University President's Medal of Merit for Academic Excellence**, UPLB
2013	**Recipient of the Medal of Merit for Academic Excellence** from the College of Arts and Sciences, UPLB
2013	**Recipient of the Medal of Merit for Academic Excellence** from the Institute of Biological Sciences, UPLB
2009-2013	**Consistent University Scholar and College Scholar,** UPLB

GRANTS AND FELLOWSHIPS (>29 000 €)

2023	**Full Scholarship Travel Grant (10% Success Rate),** Early Career Researcher Plant Networking Meeting and IPB Symposium, Leopoldina/Leibniz Institute of Plant Biochemistry, Halle (Saale), Germany, 08-11 May 2023
2023	**Deutsche Botanische Gesellschaft e.V. (DBG) Travel Scholarship** (250 €), Molecular Biology of Plants 2023, Sportschule Hennef, North Rhine-Westphalia, Germany, 06-09 February 2023
2022	**Deutsche Botanische Gesellschaft e.V. (DBG) Travel Scholarship** (400 €), Botanik-Tagung: International Conference of the German Society for Plant Sciences, University of Bonn, 28 August – 01 September 2022
2022	**Full Scholarship Travel Grant (highly competitive),** New Phytologist Next Generation Scientist 2022, Delta Centre, University of Tartu, Estonia, 19-22 July 2022
2018	**TIGP-IIP Summer Internship Grant** (~75 000 NTD or ~2 300 € for 2 months), Yuki Nakamura Laboratory, Taiwan International Graduate Program-International Internship Program (TIGP-IIP), Academia Sinica, Taipei, Taiwan, 01 May – 30 June 2018
2017	**Recipient of the UP COOPERATE Scholarship Grant** (~9 000 €) for MSc Thesis in Philipps-Universität Marburg, Germany

2016	**Recipient of the Winter School On Quantitative Systems Biology Travel Grant** (~1 500 €) in Trieste, Italy
2015-2017	**DOST-ASTHRDP-NSC Scholarship Award** for MSc Molecular Biology and Biotechnology (~15 000 € for 2 years)
2012-2013	**Commission on Higher Education (CHED) Scholarship Award** for BSc Biology (200 € for 1 semester)

MENTORING AND TEACHING EXPERIENCE

10/2024	Supervised Bachelor students (~160 students) for their practical course in Plant Physiology, RWTH Aachen, Germany
09/2022-01/2023	Supervised a Bachelor student (Nadja Kelber) for her BSc Thesis project, University of Rostock
04/2022-03/2023	Supervised a Master student (Lucas Erdmann) for his research practicum and MSc Thesis project, University of Rostock
2020-2021	GradMap Mentor: provides application and career assistance, and advice to Filipino STEM students who plan to pursue graduate studies overseas
2020	Assisted and supervised undergraduate students under Reimo Zoschke's and Rita Zrenner's laboratory class on 'Genetics and Microbiology' at the University of Potsdam (Summer Semester 2020-2021)
2019	Supervised a summer intern (Reina Esther Caro) under the TIGP-IIP internship program in Dr. Yuki Nakamura Lab, Academia Sinica
2018	Assisted in Undergraduate (Elementary Plant Physiology; Class size: 130 students) and Graduate (Plant Photophysiology; Class size: 15 students) Courses in UPLB as a Teaching Assistant/Graduate Student Apprentice of Dr. Maribel L. Dionisio-Sese (2nd semester 2017-2018)

INTERNATIONAL TRAININGS/ COMPETITIONS

2020	Selected Participant out of 550 applicants from 35 countries, Johns Hopkins CBID COVID-19 Design Challenge by The Johns Hopkins University Center for Bioengineering Innovation & Design
2019	Participant, 2019 Nobel Prize Dialogue, Berlin, Germany

TALKS PRESENTED

2023 **Araguirang GE**. "Spliceosomal components are vital for the adjustment of the C:N balance during high light acclimation" September 19-22, 2023, Adam Mickiewicz University, Poznań, Poland

2023 **Araguirang GE**. "When Plants Paint Their Leaves Purple: Regulation of Anthocyanin Biosynthesis in High Light" May 10, 2023, Leibniz Institute of Plant Biochemistry, Halle (Saale), Germany

2023 **Araguirang GE**. "When Plants Paint Their Leaves Purple: Regulation of Anthocyanin Biosynthesis in High Light", Graduate Workshop: 10th Anniversary Celebration of the Department of Life, Light & Matter (LL&M), January 27, 2023, University of Rostock, Germany (in-person)

2023 **Araguirang GE**. "When Plants Paint Their Leaves Purple: Regulation of Anthocyanin Biosynthesis in High Light" January 23, 2023, TRR175: The Green Hub Project C06 Yearly Meeting, Germany (Online Presentation)

2022 **Araguirang GE**. "When Plants Paint Their Leaves Purple: Analyses of New Factors Involved in the Regulation of Anthocyanin Biosynthesis" March 10, 2022, TRR175: The Green Hub Project C06 Yearly Meeting, Germany (Online Presentation)

2021 **Araguirang GE**. "Regulation of Flavonoid Biosynthesis by Plastid-Derived Signals" February 5, 2021, TRR175: The Green Hub Project C06 Yearly Meeting, Germany (Online Presentation)

POSTERS PRESENTED

2023 **Araguirang GE**, Kleine T, Lunn J, Venn B, Mühlhaus T, Leister D, and Richter AS. When Plants Paint Their Leaves Purple: Regulation of Anthocyanin Biosynthesis in High Light" February 6-9, 2023. Molecular Biology of Plants Conference (MBP2023), Hennef, Germany

2022 **Araguirang GE**, Kleine T, Leister D, and Richter A. "When Plants Paint Their Leaves Purple: Regulation of Anthocyanin Biosynthesis in High Light" Dec. 7 -9, 2022. 24th EMBL PhD Symposium (The Spectra of Life: Dimensional Breadth in Biological Research), EMBL, Heidelberg, Germany

2022 **Araguirang GE**, Kleine T, Leister D, and Richter A. "When Plants Paint Their Leaves Purple: Regulation of Anthocyanin Biosynthesis in High Light" Aug 28-Sept 1, 2022. Botanik-Tagung: International Conference of the German Society for Plant Sciences. University of Bonn, Germany

2022 **Araguirang GE**, Kleine T, Leister D, and Richter A. "When Plants Paint Their Leaves Purple: Regulation of Anthocyanin Biosynthesis in High Light" July 19-22, 2022. New Phytologist Next Generation Scientist 2022. University of Tartu, Estonia

2018 **Araguirang GE**, Angkawijaya AE, and Nakamura Y. "Choline/Ethanolamine Kinase 3 (CEK3) plays a significant role in root cellular architecture". 2018 IPMB 6th Annual Poster Competition. Hallway, 4F, Humanities and Social Science Building, Academia Sinica, Taipei, Taiwan

2018 **Araguirang GE**, Angkawijaya, AE, and Nakamura Y. "Elucidating the tissue and subcellular localization of Choline/Ethanolamine Kinase 3 (CEK3) and its mutational effects on the root phenotype of Arabidopsis thaliana". Taiwan International Graduate Program-International Internship Program, Academia Sinica, Taipei, Taiwan

2017 Madigal JP, **Araguirang GE,** Arizala A, Asilo EB, Batalon JL, Bello E, Monge J, Sanchez N, and Elegado F. 2017. "Optimization of banana (Musa acuminata x balbisiana) pseudostem enzymatic hydrolysis for biomass production and fermentation". The 39th Annual Scientific Meeting of National Academy of Science and Technology. The Manila Hotel, Philippines

2013 Zafaralla MT and **Araguirang GE**. 2013. "Some influences of rainfall in Laguna de Bay". RIHN-LakeHEAD Community Forum 2013. BP International Makiling, Los Banos-Laguna, Philippines

References

Agati, G., Guidi, L., Landi, M., and Tattini, M. (2021). Anthocyanins in photoprotection: knowing the actors in play to solve this complex ecophysiological issue. New Phytol 232, 2228-2235.

Agati, G., Brunetti, C., Fini, A., Gori, A., Guidi, L., Landi, M., Sebastiani, F., and Tattini, M. (2020). Are flavonoids effective antioxidants in plants? Twenty years of our investigation. Antioxidants 9, 1098.

Alcázar,R., Marco, F., Cuevas, J.C., Patron, M., Ferrando, A., Carrasco, P., Tiburcio, A.F., and Altabella, T. (2006). Involvement of polyamines in plant response to abiotic stress. Biotechnol Lett 28, 1867-1876,

Alpert, P. and Simms, E.L. (2002). The relative advantages of plasticity and fixity in different environments: when is it good for a plant to adjust? Evo Ecol 16, 285–297.

An, JP., Xu, R.R., Liu, X., Zhang, J.C., Wang, X.F., You, C.X., and Hao, Y.J. (2021a). Jasmonate induces biosynthesis of anthocyanin and proanthocyanidin in apple by mediating the JAZ1-TRB1-MYB9 complex. Plant J 106, 1414–1430.

An, J.P., Yao, J.F., Xu, R.R., You, C.X., Wang, X.F., and Hao, Y.J. (2018.) Apple bZIP transcription factor MdbZIP44 regulates abscisic acid-promoted anthocyanin accumulation. Plant Cell Environ 41, 2678–2692.

An, J.P., Zhang, X.W., Liu, Y.J., Wang, X.F., You, C.X., and Hao, Y.J. (2021b). ABI5 regulates ABA-induced anthocyanin biosynthesis by modulating the MYB1-bHLH3 complex in apple. J Exp Bot 72, 1460–1472.

Araguirang, G.E., and Richter, A.S. (2022). Activation of anthocyanin biosynthesis in high light – what is the initial signal? New Phytol. 236: 2037-2043.

Araguirang, G.E., Venn, B., Kelber, N.-M., Feil, R., Lunn, J., Kleine, T., Leister, D., Mühlhaus, T. and Richter, A.S. (2024). Spliceosomal complex components are critical for adjusting the C:N balance during high-light acclimation. Plant J, 119: 153-175.

Arenas, J.E., and Abelson, J.N. (1997). Prp43: An RNA helicase-like factor involved in spliceosome disassembly. Biochemistry, pp. 11798-11802.

Baena-González, E., Rolland, F., Thevelein, J.M., and Sheen, J. (2007) A central integrator of transcription networks in plant stress and energy signalling. Nature 448, 938–942.

Balcke, G.U., Vahabi, K., Giese, J., Finkemeier, I., and Tissier, A. (2023). Coordinated metabolic adaptation of Arabidopsis thaliana to high light. Plant J, 120: 387-405.

Banani, S.F., Lee, H.O., Hyman, A.A., and Rosen, M.K. (2017). Biomolecular condensates: organizers of cellular biochemistry. Nat Rev Mol Cell Bio 18, 285-298.

Black, D.L. (2003). Mechanisms of alternative pre-messenger RNA splicing. In Annual Review of Biochemistry, pp. 291-336.

Borevitz, J.O., Xia, Y., Blount, J., Dixon, R.A., and Lamb, C. (2000). Activation tagging identifies a conserved MYB regulator of phenylpropanoid biosynthesis. Plant Cell 12, 2383-2394.

Brett, D., Pospisil, H., Valcárcel, J., Reich, J., and Bork, P. (2002). Alternative splicing and genome complexity. Nature Genetics 30, 29-30.

Broucke, E., Vi Dang, T.T., Li, Y., Hulsmans, S., Van Leene, J., De Jaeger, G., Hwang, I., Van den Ende, W., and Rolland, F. (2023). SnRK1 inhibits anthocyanin biosynthesis through both transcriptional regulation and direct phosphorylation and dissociation of the MYB/bHLH/TTG MBW complex. Plant J, 115: 1193-1213.

Burch-Smith, T.M., Schiff, M., Liu, Y., and Dinesh-Kumar, S.P. (2006). Efficient virus-induced gene silencing in Arabidopsis, Plant Physiol 142, 21–27.

Cabezas-Fuster, A., Micol-Ponce, R., Fontcuberta-Cervera, S., and Ponce, M.R. (2022) Missplicing suppressor alleles of Arabidopsis PRE-MRNA PROCESSING FACTOR 8 increase splicing fidelity by reducing the use of novel splice sites, Nucleic Acids Res 50, 5513–5527.

Calixto, C.P.G., Guo, W., James, A.B., Tzioutziou, N.A., Entizne, J.C., Panter, P.E., Knight, H., Nimmo, H.G., Zhang, R., and Brown, J.W.S. (2018). Rapid and dynamic alternative splicing impacts the Arabidopsis cold response transcriptome. Plant Cell 30, 1424-1444.

Cao, O., Renna, L., Stefano, G., and Brandizzi, F. (2016). SYP73 Anchors the ER to the Actin Cytoskeleton for Maintenance of ER Integrity and Streaming in Arabidopsis. Current Bio 26, 3245-3254.

Cecchini, N.M., Torres, J.R., López, I.L., Cobo, S., Nota, F., and Alvarez, M.E. (2022). Alternative splicing of an exitron determines the subnuclear localization of the Arabidopsis DN glycosylase MBD4L under heat stress. Plant Journal 110, 377-388.

Chen, J., Wu, S., Dong, F., Li, J., Zeng, L., Tang, J., and Gu, D. (2021). Mechanism underlying the shading-induced chlorophyll accumulation in Tea leaves. Front. Plant Sci. 12:779819.

Chen, L., Shi, X., Nian, B., Duan, S., Jiang, B., Wang, X., Lv, C., Zhang, G., Ma, Y., and Zhao, M. (2020). Alternative splicing regulation of anthocyanin biosynthesis in camellia sinensis var. assamica unveiled by PacBio Iso-Seq. G3: Genes, Genomes, Genetics 10, 2713-2723.

Chotewutmontri, P. and Barkan, A. (2018). Multilevel effects of light on ribosome dynamics in chloroplasts program genome-wide and psbA-specific changes in translation. PLOS Genetics 14: e1007555

Craine, J.M. and Dybzinski, R. (2013). Mechanisms of plant competition for nutrients, water and light. Funct Ecol, 27: 833-840.

Das, P.K., Shin, D.H., Choi, S.B., Yoo, S.D., Choi, G., and Park Y.I. (2012). Cytokinins enhance sugar-induced anthocyanin biosynthesis in Arabidopsis. Mol. Cells 34, 93–101.

DeLano, W. L. (2002). Pymol: An open-source molecular graphics tool. CCP4 Newsl. Protein Crystallogr 40, 82-92.

Dolata, J., Guo, Y., Kołowerzo, A., Smoliński, D., Brzyżek, G., Jarmołowski, A., and Świeżewski, S. (2015). NTR 1 is required for transcription elongation checkpoints at alternative exons in Arabidopsis. The EMBO journal *34*, 544-558.

Dorone, Y., Boeynaems, S., Flores, E., Jin, B., Hateley, S., Bossi, F., Lazarus, E., Pennington, J.G., Michiels, E., De Decker, M., Vints, K., Baatsen, P., Bassel, G.W., Oteguie, M.S., Holehouse, A.S., Exposito-Alonso, M., Sukenik, S., Gitler, A.D., and Rhee, Y.S. (2021). A prion-like protein regulator of seed germination undergoes hydration-dependent phase separation. Cell 184, 4284–4298.e27a.

Dubos, C., Le Gourrierec, J., Baudry, A., Huep, G., Lanet, E., Debeaujon, I., Routaboul, J.-M., Alboresi, A., Weisshaar, B. and Lepiniec, L. (2008). MYBL2 is a new regulator of flavonoid biosynthesis in Arabidopsis thaliana. Plant J 55, 940-953.

Eliot, A.C. and Kirsch, J.F. (2004). Pyridoxal phosphate enzymes: Mechanistic, structural, and evolutionary considerations. Annu Rev Biochem *73*, 383-415.

Farinas, B. and Mas, P. (2011). Functional implication of the MYB transcription factor RVE8/LCL5 in the circadian control of histone acetylation. Plant J 66, 318-329.

Figueroa, C.M., Feil, R., Ishihara, H., Watanabe, M., Kolling, K., Krause, U., Hohne, M., Encke, B., Plaxton, W.C., Zeeman, S.C., Li, Z., Schulze, W.X., Hoefgen, R., Stitt, M., and Lunn, J.E (2016). Trehalose 6-phosphate coordinates organic and amino acid metabolism with carbon availability. Plant J 85, 410-423.

Freschet, G.T., Violle, C., Bourget, M. Y., Scherer-Lorenzen, M., and Fort, F. (2018). Allocation, morphology, physiology, architecture: the multiple facets of plant above- and below-ground responses to resource stress. New Phytol 219, 1338-1352.

Fu, X., Gregory, L.M., Weise, S.E., and Walker, B.J. (2023). Integrated flux and pool size analysis in plant central metabolism reveals unique roles of glycine and serine during photorespiration. Nat Plants 9, 169-178.

Garcia-Molina, A., Kleine, T., Schneider, K., Muhlhaus, T., Lehmann, M., and Leister, D. (2020). Translational components contribute to acclimation responses to high light, heat, and cold in Arabidopsis. iScience 23, 101331.

Gonzalez, A., Zhao, M., Leavitt, J.M., and Lloyd, A.M. (2008). Regulation of the anthocyanin biosynthetic pathway by the TTG1/bHLH/Myb transcriptional complex in Arabidopsis seedlings. Plant J 53, 814-827.

Goss, R. and Lepetit, B. (2015). Biodiversity of NPQ. J Plant Physiol, *172*, 13–32.

Gou, J.Y., Felippes, F.F., Liu, C.J., Weigel, D., and Wang, J.W. (2011). Negative regulation of anthocyanin biosynthesis in Arabidopsis by a miR156-targeted SPL transcription factor. Plant Cell 23, 1512-1522.

Gould, K.S., Jay-Allemand, C., Logan, B.A., Baissac, Y., and Bidel, L.P.R. (2018). When are foliar anthocyanins useful to plants? Re-evaluation of the photoprotection hypothesis using Arabidopsis thaliana mutants that differ in anthocyanin accumulation. Environmental and Experimental Botany 154, 11-22.

Grainger, R.J. and Beggs, J.D. (2005). Prp8 protein: at the heart of the spliceosome. RNA 5, 533-557.

Graska, J., Fidler, J., Gietler, M., Prabucka, B., Nykiel, M., and Labudda, M. (2023). Nitric oxide in plant functioning: Metabolism, signaling, and responses to infestation with ecdysozoa parasites. Biology (Basel) 12, 927.

Greenberg, B.M., Gaba, V., Mattoo, A.K., and Edelman, M. (1987). Identification of a primary in vivo degradation product of the rapidly-turning-over 32 kd protein of photosystem II. EMBO J 6: 2865–2869.

Groppa, M. and Benavides, M. (2008) Polyamines and abiotic stress: recent advances. Amino Acids 34, 35-45,

Hackbusch, J., Richter, K., Müller, J., Salamini, F., and Uhrig, J.F. (2005). A central role of Arabidopsis thaliana ovate family proteins in networking and subcellular localization of 3-aa loop extension homeodomain proteins. Proc. Natl. Acad. Sci. 102, 4908-4912.

He, L., Tang, R., Shi, X., Wang, W., Cao, Q., Liu, X., Wang, T., Sun, Y., Zhang, H., Li, R., and Jia, X. (2019). Uncovering anthocyanin biosynthesis related microRNAs and their target genes by small RNA and degradome sequencing in tuberous roots of sweetpotato. BMC Plant Biol. 19,:232.

He, L., Wu, Q., Jin, Y., Fan, Y., Shi, H., Wang, Y., and Yang, W. (2023). NTR1 is involved in heat stress tolerance through mediating expression regulation and alternative splicing of heat stress genes in Arabidopsis. Frontiers in plant science 13:1082511.

Heberle, H., Meirelles, G.V., da Silva, F.R., Telles, G.P., and Minghim, R. (2015). InteractiVenn: a web-based tool for the analysis of sets through Venn diagrams. BMC Bioinformatics 16, 169.

Huang, S., Taylor, N.L., Ströher, E., Fenske, R., and Millar, A.H. (2013). Succinate dehydrogenase assembly factor 2 is needed for assembly and activity of mitochondrial complex II and for normal root elongation in Arabidopsis. Plant J, 73: 429-441.

John, S., Olas, J.J., and Mueller-Roeber, B. (2021). Regulation of alternative splicing in response to temperature variation in plants. Journal of Experimental Botany 72, 6150-6163.

Jones, M.A., Williams, B.A., McNicol, J., Simpson, C.G., Brown, J.W.S., and Harmer, S.L. (2012). Mutation of Arabidopsis *SPLICEOSOMAL TIMEKEEPER LOCUS1* causes circadian clock defects. Plant Cell 24, 4066-4082.

Jumper, J., Evans, R., Pritzel, A., Green, T., Figurnov, M., Ronneberger, O., Tunyasuvunakool, K., Bates, R., Žídek, A., Potapenko, A., Bridgland, A., Meyer, C., Kohl, SAA., Ballard, A.J., Cowie, A., Romera-Paredes, B., Nikolov, S., Jain, R., Adler, J., Back, T., Petersen, S., Reiman, D., Clancy, E., Zielinski, M., Steinegger, M., Pacholska, M., Berghammer, T., Bodenstein, S., Silver, D., Vinyals, O., Senior, A.W., Kavukcuoglu, K., Kohli, P., and Hassabis, D. (2021). Highly accurate protein structure prediction with AlphaFold. Nature 596, 583-589.

Jung, J.-H., Barbosa, A.D., Hutin, S., Kumita, J.R., Gao, M., Derwort, D., Silva, C.S., Lai, X., Pierre, E., Geng, F., Kim, S.-B., Baek, S., Zubieta, C., Jaeger, K.E., and Wigge, P.A. (2020). A prion-like domain in ELF3 functions as a thermosensor in Arabidopsis. Nature 585, 256–260.

Kan, Z., Rouchka, E.C., Gish, W.R. and States, D.J. (2001). Gene structure prediction and alternative splicing analysis using genomically aligned ESTs. Genome Res 11, 889–900.

Kato, Y., Sun, X., Zhang, L., and Sakamoto, W. (2012). Cooperative D1 Degradation in the Photosystem II Repair Mediated by Chloroplastic Proteases in Arabidopsis. Plant Physiol 159, 1428–1439.

Kleine, T., Nagele, T., Neuhaus, H.E., Schmitz-Linneweber, C., Fernie, A.R., Geigenberger, P., Grimm, B., Kaufmann, K., Klipp, E., Meurer, J., Mohlmann, T., Muhlhaus, T., Naranjo, B., Nickelsen, J., Richter, A., Ruwe, H., Schroda, M., Schwenkert, S., Trentmann, O., Willmund, F., Zoschke, R., and Leister, D. (2021). Acclimation in plants - the Green Hub consortium. Plant J 106, 23-40.

Kim, V.N., Han, J., and Siomi, M.C. (2009). Biogenesis of small RNAs in animals. Nat. Rev. Mol. Cell Biol. 10, 126–139.

Kuhn, A.N., Reichl, E.M., and Brow, D.A. (2002). Distinct domains of splicing factor Prp8 mediate different aspects of spliceosome activation, Proc. Natl. Acad. Sci. 99, 9145-9149.

Kurihara, Y. and Watanabe, Y. (2004) Arabidopsis micro-RNA biogenesis through Dicer-like 1 protein functions. Proc. Natl. Acad. Sci. U.S.A. 101, 12753-12758.

Lancaster, A.K., Nutter-Upham, A., Lindquist, S., and King, O.D. (2014). PLAAC: a web and command-line application to identify proteins with Prion-Like Amino Acid Composition Bioinformatics 30, 2501–2502.

Laubinger, S., Sachsenberg, T., Zeller, G., Busch, W., Lohmann, J.U., Ratsch, G., and Weigel, D. (2008). Dual roles of the nuclear cap-binding complex and SERRATE in pre-mRNA splicing and microRNA processing in Arabidopsis thaliana. Proc Natl Acad Sci U S A 105, 8795-8800.

Lea, U. S., Slimestad, R., Smedvig, P., and Lillo, C. (2007). Nitrogen deficiency enhances expression of specific MYB and bHLH transcription factors and accumulation of end products in the favonoid pathway. Planta 225, 1245–1253.

Lee, R.C., and Ambros, V. (2001). An extensive class of small RNAs in Caenorhabditis elegans. Science 294, 862-864.

Lee, Y. and Rio, D.C. (2015). Mechanisms and regulation of alternative pre-mRNA splicing. Annu Rev Biochem 84, 291-323.

Legen, J., Lenzen, B., Kachariya, N., Feltgen, S., Gao, Y., Mergenthal, S., Weber, W., Klotzsch, E., Zoschke, R., Sattler, M., and Schmitz-Linneweber C. (2024). A prion-like domain is required for phase separation and chloroplast RNA processing during cold acclimation in Arabidopsis. Plant Cell 36, 2851-2872.

Leigh, A., Sevanto, S., Close, J. D., and Nicotra, A. B. (2017). The influence of leaf size and shape on leaf thermal dynamics: does theory hold up under natural conditions? Plant Cell Environ. 40, 237–248.

Li, C., Shi, L., Wang, Y., Li, W., Chen, B., Zhu, L., and Fu, Y. (2020). Arabidopsis ECAP is a new adaptor protein that connects JAZ repressors with the TPR2 co-repressor to suppress jasmonate-responsive anthocyanin accumulation. Mol Plant 13: 246–265.

Li, Y., Cui, W., Wang, R., Lin, M., Zhong, Y., Sun, L., Qi, X., and Fang, J. (2019). MicroRNA858-mediated regulation of anthocyanin biosynthesis in kiwifruit (*Actinidia arguta*) based on small RNA sequencing. PLoS One 14, e0217480.

Liang, J. and He, J. (2018). Protective role of anthocyanins in plants under low nitrogen stress. Biochem Biophys Res Commun 498, 946-953.

Liao, H.-S., Yang, C.-C., Hsieh, M.-H. (2022). Nitrogen deficiency- and sucrose-induced anthocyanin biosynthesis is modulated by HISTONE DEACETYLASE15 in Arabidopsis. J Exp Bot, 73, 3726–3742.

Liu, C., Xin, Y., Xu, L., Cai, Z., Xue, Y., Liu, Y., Xie, D., Liu, Y., and Qi, Y. (2018). Arabidopsis ARGONAUTE 1 Binds Chromatin to Promote Gene Transcription in Response to Hormones and Stresses. Dev Cell. 44, :348-361.e7.

Liu, Y., Schiff, M. and Dinesh-Kumar, S.P. (2002), Virus-induced gene silencing in tomato. Plant J, 31: 777-786.

Liu, Z., Shi, M.Z., and Xie, D.Y. (2014). Regulation of anthocyanin biosynthesis in Arabidopsis thaliana red pap1-D cells metabolically programmed by auxins. Planta 239, 765–781.

Llinas, R.J., Xiong, J.Q., Clark, N.M., Burkhart, S.E., and Bartel, B. (2022) An Arabidopsis pre-RNA processing8a (prp8a) missense allele restores splicing of a subset of mis-spliced mRNAs. Plant Phys 189, 2175–2192.

Lloyd, A., Brockman, A., Aguirre, L., Campbell, A., Bean, A., Cantero, A., and Gonzalez, A. (2017). Advances in the MYB-bHLH-WD Repeat (MBW) Pigment Regulatory Model: Addition of a WRKY Factor and Co-option of an Anthocyanin MYB for Betalain Regulation. Plant Cell Physiol 58, 1431-1441.

Lobbes, D., Rallapalli, G., Schmidt, D.D., Martin, C., and Clarke, J. (2006). SERRATE: a new player on the plant microRNA scene. EMBO Rep 7, 1052-1058.

Loreti, E., Povero, G., Novi, G., Solfanelli, C., Alpi, A., and Perata, P. (2008). Gibberellins, jasmonate and abscisic acid modulate the sucrose-induced expression of anthocyanin biosynthetic genes in Arabidopsis. New Phytol 179, 1004–1016.

Luciński, R., Misztal,R., Samardakiewicz, S., and Jackowski, G. (2011). The thylakoid protease Deg2 is involved in stress-related degradation of the photosystem II light-harvesting protein Lhcb6 in Arabidopsis thaliana. New Phyt 192, 74-86.

Mur, L.A.J., Mandon, J., Persijn, S., Cristescu, S.M., Moshkov, I.E., Novikova, G.V., Hall, M.A., Harren, F., Hebelstrup, K., and Gupta, K. (2013). Nitric oxide in plants: an assessment of the current state of knowledge. AoB PLANTS 5, pls052.

Lunn, J.E., Feil, R., Hendriks, J.H., Gibon, Y., Morcuende, R., Osuna, D., Scheible, W.R., Carillo, P., Hajirezaei, M.R., and Stitt, M. (2006). Sugar-induced increases in trehalose 6-phosphate are correlated with redox activation of ADPglucose pyrophosphorylase and higher rates of starch synthesis in Arabidopsis thaliana. Biochem J 397, 139-148.

Martín, G., Márquez, Y., Mantica, F., Duque, P., and Irimia, M. (2021). Alternative splicing landscapes in Arabidopsis thaliana across tissues and stress conditions highlight major functional differences with animals. Genome Biology 22, 35.

Matsui, K., Umemura, Y. and Ohme-Takagi, M. (2008). AtMYBL2, a protein with a single MYB domain, acts as a negative regulator of anthocyanin biosynthesis in Arabidopsis. Plant J 55, 954-967.

Mittler, R., Zandalinas, S.I., Fichman, Y., and Van Breusegem, F. (2022). Reactive oxygen species signalling in plant stress responses. Nat Rev Mol Cell Biol 23, 663–679.

Nicol, L., Nawrocki, W.J., and Croce, R. (2019). Disentangling the sites of non-photochemical quenching in vascular plants. Nat Plants, 5, 1177–1183.

Nunes-Nesi, A., Fernie, A.R., and Stitt, M. (2010). Metabolic and Signaling Aspects Underpinning the Regulation of Plant Carbon Nitrogen Interactions. Mol Plant 3, 973-996.

Ori, N., Eshed, Y., Chuck, G., Bowman, J.L. and Hake, S. (2000). Mechanisms that control knox gene expression in the Arabidopsis shoot. Development, 127, 5523–5532.

Prigge, M.J. and Wagner, D.R. (2001). The Arabidopsis SERRATE gene encodes a zinc-finger protein required for normal shoot development. The Plant Cell, 13, 1263–1279.

Qi, T., Song, S., Ren, Q., Wu, D., Huang, H., Chen, Y., Fan, M., Peng, W., Ren, C., and Xie, D. (2011). The jasmonate-ZIM-domain proteins interact with the WD-Repeat/bHLH/MYB complexes to regulate jasmonate-mediated anthocyanin accumulation and trichome initiation in Arabidopsis thaliana. Plant Cell 23, 1795–1814.

Reitzer, L. (2003). Nitrogen assimilation and global regulation in *Escherichia coli*. Annu Rev Micro 57, 155-176.

Richter, A.S., Tohge, T., Fernie, A.R., and Grimm, B. (2020). The genomes uncoupled-dependent signalling pathway coordinates plastid biogenesis with the synthesis of anthocyanins. Philos Trans R Soc Lond B Biol Sci 375, 20190403.

Rolland, F., Moore, B., and Sheen, J. 2002. Sugar sensing and signaling in plants. Plant Cell 14: 185–205.

Rozendaal, D.M.A,, Hurtado, V.H., and Poorter, L. (2006). Plasticity in leaf traits of 38 tropical tree species in response to light; relationships with light demand and adult stature. Funct Ecol 20, 207–216.

Ruban, A.V. (2016). Nonphotochemical Chlorophyll Fluorescence Quenching: Mechanism and Effectiveness in Protecting Plants from Photodamage. Plant Physiol 170, 1903–1916.

Russell, A.W., Critchlet, C., Robinson, S.A., Franklin, L.A., Seaton, G.R., Chow, W.S., Anderson, J.M., and Osmond, C.B. (1995). Photosystem II regulation and dynamics of the chloroplast D1 protein in Arabidopsis leaves during photosynthesis and photoinhibition. Plant Physiol. 107, 943-952.

Ruvkun, G. (2001). Molecular biology: Glimpses of a tiny RNA world. In Science, pp. 797-799.

Salter, A.H., Virgin, I., Hagman, A., and Andersson, B. (1992). On the molecular mechanism of light-induced D1 protein degradation in photosystem II core particles. Biochemistry 31, 3990–3998

Schuster, M., Gao, Y., Schöttler, M.A., Bock, R., and Zoschke, R. (2020). Limited responsiveness of chloroplast gene expression during acclimation to high light in tobacco. Plant Physiol 182, 424–435.

Sharma, N., Nagar, S., Thakur, M., Suriyyakumar, P., Kataria, S., Shanker, A.K., Landi, M., and Anand, A. (2023). Photosystems under high light stress: throwing light on mechanism and adaptation. Photosynthetica 61, 250-263.

Shen., X., Zhao, K., Liu, L., Zhang, K., Yuan, H., Liao, X., Wang, Q., Guo, X., Li, F., Li, T. (2014). A role for PacMYBA in ABA-regulated anthocyanin biosynthesis in red-colored sweet cherry cv Hong Deng (Prunus avium L.). Plant & Cell Physiol 55, 862–880.

Shi, H.T., Liu, G.Y., Wei, Y.X., and Chan, Z.L. (2018). The zinc-finger transcription factor ZAT6 is essential for hydrogen peroxide induction of anthocyanin synthesis in Arabidopsis. Plant Mol Bio 97: 165–176.

Stracke, R., Ishihara, H., Huep, G., Barsch, A., Mehrtens, F., Niehaus, K., and Weisshaar, B. (2007). Differential regulation of closely related R2R3-MYB transcription factors controls flavonol accumulation in different parts of the Arabidopsis thaliana seedling. Plant J 50, 660-677.

Syed, N.H., Kalyna, M., Marquez, Y., Barta, A., and Brown, J.W.S. (2012). Alternative splicing in plants - coming of age. Trends Plant Sci 17, 616-623.

Tirumalai, V., Swetha, C., Nair, A., Pandit, A., and Shivaprasad, P.V. (2019). miR828 and miR858 regulate VvMYB114 to promote anthocyanin and flavonol accumulation in grapes. J Exp Bot 70, 4775–4792.

Varadi, M., Bertoni, D,. Magana, P., Paramval, U., Pidruchna, I., Radhakrishnan, M., Tsenkov, M., Nair, S., Mirdita, M., Yeo, J., Kovalevskiy, O., Tunyasuvunakool, K., Laydon, A., Žídek, A., Tomlinson, H., Hariharan, D., Abrahamson, J., Green, T., Jumper, J., Birney, E., Steinegger, M., Hassabis, D,. and Velankar, S. (2024). AlphaFold Protein Structure Database in 2024: providing structure coverage for over 214 million protein sequences. Nucleic Acids Res. 52, D368-D375.

Wahl, M.C., Will, C.L., and Lührmann, R. (2009). The Spliceosome: Design Principles of a Dynamic RNP Machine. Cell 136, 701-718.

Wan, R., Yan, C., Bai, R., Lei, J., and Shi, Y. (2017). Structure of an Intron Lariat Spliceosome from Saccharomyces cerevisiae. Cell 171, 120-132.

Wang, C., Wang, X., Yang, Z., and Gao, X. (2024a). Pleiotropic regulatory locus 1 maintains actin cytoskeleton integrity and cellular homeostasis to enable Arabidopsis root growth. iScience 27, 110414.

Wang, J., Chen, S., Jiang, N., Li, N., Wang, X., Li, Z., Li, X., Liu, H., Li, L., Yang, Y., Ni, T., Yu, C., Ma, J., Zheng, B., and Ren, G. (2019). Spliceosome disassembly factors ILP1 and NTR1 promote miRNA biogenesis in Arabidopsis thaliana. Nucleic Acids Res 47, 7886-7900.

Wang, J., Yao, R., Sun, Z., Wang, M., Jiang, C., Zhao, X., Liu, X., Zhong, C., Zhang, H., Zhao, S., Wang, X., and Yu, H. (2024b). Effects of shading on morphology, photosynthesis characteristics, and yield of different shade-tolerant peanut varieties at the flowering stage. Front. Plant Sci. 15:1429800.

Wang, Y., Liu, W., Wang, X., Yang, R., Wu, Z., Wang, H., Wang, L., Hu, Z., Guo, S., Zhang, H., Lin, J., and Fu, C. (2020). MiR156 regulates anthocyanin biosynthesis through SPL targets and other microRNAs in poplar. Hortic Res 7, 118.

Wei, X., Ke, H., Wen, A., Gao, B., Shi, J., and Feng, Y. (2021) Structural basis of microRNA processing by Dicer-like 1. Nat. Plants 7, 1389–1396.

Wientjes, E., van Stokkum, I.H.M., van Amerongen§, H., and Croce, R. (2011). The role of the individual LHCAs in Photosystem I excitation energy trapping. Biophys. J. 101, 745-754.

Wu, J., Chen, W., Ge, S., Liu, X.,Shann, J., Zhang, M., Su, Y., and Liu, Y. (2024). ILP1 and NTR1 affect the stability of U6 snRNA during spliceosome complex disassembly in Arabidopsis. Plant Sci 347, 112199.

Wu, X., Ma, Y., Wu, J., Wang, P., Zhang, Z,. Xie, R., Liu, J., Fan, B., Wei, W., Nie, L.Z., and Liu, X. (2022). Identification of microRNAs and their target genes related to the accumulation of anthocyanin in purple potato tubers (Solanum tuberosum). Plant Direct 6, e418.

Xie, Y., Tan, H., Ma, Z., and Huang, J. (2016). DELLA proteins promote anthocyanin biosynthesis via sequestering MYBL2 and JAZ suppressors of the MYB/bHLH/WD40 complex in Arabidopsis thaliana. Mol Plant 9: 711–721.

Xu, Z., Mahmood, K., and Rothstein, S.J. (2017). ROS induces anthocyanin productionvia late biosynthetic genes and anthocyanin deficiency confers the hypersensitivity to ROS-generating stresses in Arabidopsis. Plant Cell Physio 58, 1364–1377.

Xue, B., Dunbrack, R.L., Williams, R.W., Dunker, A.K., and Uversky, V.N. (2010). PONDR® FIT: A meta-predictor of intrinsically disordered amino acids. BBA Proteins and Proteomics 1804, 996–1010.

Yonekura-Sakakibara, K., Higashi, Y., and Nakabayashi, R. (2019) The Origin and Evolution of Plant Flavonoid Metabolism. Front. Plant Sci. 10:943.

Yoshizumi, T., Tsumoto, Y., Takiguchi, T., Nagata, N., Yamamoto, Y.Y., Kawashima, M., Ichikawa, T., Nakazawa, M., Yamamoto, N., and Matsui, M. (2006). Increased level of polyploidy1, a conserved repressor of CYCLINA2 transcription, controls endoreduplication in Arabidopsis. Plant Cell 18, 2452-2468.

Zang, J., Klemm, S., Pain, C., Duckney P., Bao, Z., Stamm, G., Kriechbaumer, V., Bürsteinbinder, K., Husset, P.J., and Wang, P. (2021). A novel plant actin-microtubule bridging complex regulates cytoskeletal and ER structure at ER-PM contact sites. Current Bio 31, 1251-1260.

Zhang, H., Zhao, Y., and Zhu, J.K. (2020). Thriving under Stress: How Plants Balance Growth and the Stress Response. Dev Cell 55, 529-543.

Zhang, S., Liu, Y., and Yu, B. (2014a). PRL1, an RNA-binding protein, positively regulates the accumulation of miRNAs and siRNAs in Arabidopsis. PLoS Genetics 10: e1004841.

Zhang, X., Niu, D., Carbonell, A., Wang, A., Lee, A., Tun, V., Wang, Z., Carrington, J.C., Chang, C.E., and Jin H,. (2014b). ARGONAUTE PIWI domain and microRNA duplex structure regulate small RNA sorting in Arabidopsis. Nat Commun. 5, 5468.

Zhang, Z. Y., Gong, W. Z., Yang, W. Y., and Ma, L. (2007). Correlation between agronomic characters and yield in relay-planting soybeans. Soybean Sci. 5, 680–686.

Zirngibl, M.E., Araguirang, G.E., Kitashova, A., Jahnke, K., Rolka, T., Kuhn, C., Nagele, T., and Richter, A.S. (2023). Triose phosphate export from chloroplasts and cellular sugar content regulate anthocyanin biosynthesis during high light acclimation. Plant Commun 4, 100423.